Investigation of wing installation effects on the sound field of a model jet engine

Master Thesis

at Deutsches Zentrum für Luft- und Raumfahrt
Abteilung Triebwerksakustik

Prof. Dr. Lars Enghardt
Institut für Strömungsmechanik und Technische Akustik
Fachgebiet für Turbomaschinen- und Thermoakustik
Technische Universität Berlin

by
cand. M.Sc. **Jonas König** **Matr.-Nr. 320 900**

supervised by
Prof. Dr. Lars Enghardt
Dr. Henri Siller

Berlin, 9th October 2015

Hiermit erkläre ich, dass ich die vorliegende Arbeit selbstständig und eigenhändig sowie ohne unerlaubte fremde Hilfe und ausschließlich unter Verwendung der aufgeführten Quellen und Hilfsmittel angefertigt habe.

Signature

Berlin, 9th October 2015

Abstract

Civil air traffic has been constantly growing over the past decades. Therefore, the noise emitted by aircraft became increasingly important to public perception, as noise pollution has numerously evidenced adverse effects on human health. Jet noise - one of different noise sources of an aircraft - has been successfully alleviated by new technological advances, such as serrated nozzle geometries. This thesis aims to enhance the knowledge of jet noise generation by assessing the experimental data of an aeroacoustic investigation of jet noise generated by a common turbofan engine. The effects of aerofoil and pylon presence as well as different nozzle and cowling configurations are elaborated at flow conditions resembling the ICAO noise reference measurement points by examining the sound field of the jet via source directivity analysis. The findings agree well with theory: Wing installation increases the sound pressure level slightly for all test cases due to reflection events, while the flight stream lowers the sound emission noticeably by encasing the hot core jet flows.

Zusammenfassung

Die letzten Dekaden zeichneten sich durch einen konstanten Zuwachs des ziviles Luftverkehrs aus. In Anbetracht dieser Tatsache wuchs in der öffentlichen Wahrnehmung das Interesse an durch Flugzeugen verursachtem Lärm, da dieser bewiesenermaßen eine Vielzahl von negativen Auswirkungen auf die menschliche Gesundheit hat. Die Lärmemission des Freistrahls - eine der Lärmquellen eines Flugzeugs - konnte durch Einsatz moderner Technologien wie Chevrondüsen verringert werden. Diese Arbeit erweitert das Wissen um Triebwerksschall, indem die aeroakustischen Daten aus einem experimentellen Versuch zur Untersuchung der Lärmentstehung im Freistrahl eines Triebwerks untersucht werden. Dabei werden die Auswirkungen von Tragflügelinstallation sowie verschiedenen Düsen- und Gehäusekonfigurationen anhand von Strömungszuständen, welche die ICAO-Referenzpunkten zur Lärmmessung widerspiegeln, durch Analyse der Richtcharakteristik des Triebwerksschallfelds erörtert. Die Ergebnisse stimmen mit der Theorie überein: Die Flügelinstallation erhöht den Schalldruckpegel geringfügig, während der Flugstrahl die Schallabstrahlung durch Einschließen der heißen Kernmassenströme merklich reduziert.

Contents

List of Figures III

List of Tables V

List of Symbols VI

1 Introduction 1

1.1 Motivation . . . 2
1.2 Objective . . . 3
1.3 Approach . . . 3

2 Theory 4

2.1 Jet Engines . . . 4
2.2 Fluid Mechanics . . . 8
2.2.1 Similitude . . . 8
2.2.2 Free Jet Fluid Mechanics . . . 10
2.3 Acoustics . . . 12
2.3.1 Basics . . . 12
2.3.2 ICAO Noise Certification . . . 13
2.3.3 Free Jet Acoustics . . . 14
2.3.4 SODIX . . . 20

3 Implementation 26

3.1 Experimental Setup and Execution . . . 26
3.1.1 Coordinate System . . . 26
3.1.2 Testing Conditions . . . 27
3.1.3 Noise Test Facility . . . 28
3.1.4 Engine Setup . . . 29
3.1.5 Linear Microphone Array . . . 32

3.2 Data Sets 33
3.2.1 Raw Data 34
3.2.2 SODIX Setup 37

4 Data Analysis **43**
4.1 Aliasing 43
4.2 Flight Stream Effect 46
4.3 ICAO Reference Measurement Points 49
4.3.1 Reference Measurement Points without Flight Stream 49
4.3.2 Reference Measurement Points with Flight Stream 56
4.4 Broadband Fan Noise Simulation 63
4.5 Nozzle Configurations 66
4.5.1 Serrated Nozzle 66
4.5.2 Scarfed Nozzle 69
4.6 Long Cowl Engine 71
4.7 Remarks 74

5 Conclusion and Outlook **76**

Bibliography **78**

Appendix **81**

List of Figures

2.1 Brayton cycle 6
2.2 Turbofan engine cross-section 6
2.3 Short-cowl configuration 11
2.4 Long-cowl configuration 11
2.5 Jet mixing process 15
2.6 Jet sound directivity 16
2.7 Bypass noise reduction 17
2.8 Two-stream jet mixing regions 18
2.9 Jet sound spectrum with and without installation effects 19
2.10 SODIX source directivity calculation 22
2.11 SODIX source projection 23
2.12 SODIX example plot 24
2.13 SODIX example comparison plot 25

3.1 Coordinate System 27
3.2 QinetiQ Noise Test Facility 28
3.3 Different cowling configurations 29
3.4 Different nozzle configurations 30
3.5 Engine speaker arrangement 31
3.6 Wing model 32
3.7 Linear microphone array 33
3.8 Auto spectrum of DLR 317 (logarithmic) 35
3.9 Auto spectrum of DLR 317 (linear) 36
3.10 Comb filter effect in source directivities of DLR 317 36
3.11 DLR 317 TOB 10000 Hz for shortened source position grid 39
3.12 Source position grid 40
3.13 SODIX: Iteration count tests 40
3.14 Slack variable configuration 42

4.1 SODIX: DLR 317 aliasing effect 44

4.2 Trace wave length 45
4.3 SODIX: Aliasing effect in constructed CSM 45
4.4 SODIX: DLR 248 46
4.5 Spectra of DLR 248, DLR 317 and DLR 325 47
4.6 Auto Spectra of DLR 248 47
4.7 SODIX: DLR 248, elongated source position grid 48
4.8 SODIX: DLR 317 51
4.9 SODIX: Comparison DLR 435 - DLR 317 53
4.10 SODIX: Comparison DLR 411 - DLR 279 and DLR 395 - DLR 287 . . 55
4.11 SODIX: DLR 287 and 395 56
4.12 SODIX: DLR 325 57
4.13 SODIX: DLR 325 flight stream 58
4.14 SODIX: Comparison DLR 325 - DLR 317 59
4.15 SODIX: Comparison DLR 443 - DLR 325 60
4.16 SODIX: Comparison DLR 403 - DLR 297 and DLR 423 - DLR 257 . . 62
4.17 SODIX: DLR 257 and 423 63
4.18 SODIX: DLR 306 and 383 64
4.19 SODIX: DLR 306 and 383 full DR 64
4.20 SODIX: DLR 350 and 444 65
4.21 SODIX: DLR 350 and 444 full DR 66
4.22 SODIX: DLR 735 and 817 67
4.23 SODIX: Comparison DLR 735 - DLR 325 68
4.24 SODIX: DLR 527 and 599 70
4.25 SODIX: Comparison DLR 527 - DLR 325 71
4.26 SODIX: DLR 900 72
4.27 SODIX: Comparison DLR 900 - DLR 317 72
4.28 SODIX: DLR 914 73
4.29 SODIX: Comparison DLR 914 - DLR 325 74

A.1 Source position grid: Reference 85
A.2 Source position grid: Linear 85
A.3 Source position grid: Weighted linear 86
A.4 Source position grid: Corrected weighted linear 86

List of Tables

2.1 Maximum noise levels 14

3.1 Broadband band-pass scenarios. 31
3.2 Microphone array dimensions 33

4.1 ICAO reference measurement test points. 50
4.2 Broadband test points. 63
4.3 Nozzle geometry test points 67
4.4 Long cowl test points 71

A.1 Microphone positions 81
A.2 Third octave bands 84
A.3 Analysed test points 87

List of Symbols

Symbol	Unit	Denotation
Latin Symbols		
a	$\mathrm{m/s}$	Velocity of sound
A	$\mathrm{m^2}$	Surface area
c	$\mathrm{m/s}$	Axial air velocity
C	–	Cross-spectral matrix
d	m	Diameter
f	$\mathrm{1/s}$	Frequency
g	–	Steering vector
F	$\mathrm{kg{\cdot}m/s^2}$	Thrust
H_c	$\mathrm{kJ/kg}$	Heat of combustion
I	$\mathrm{kg{\cdot}m/s}$	Momentum
I	$\mathrm{W/m^2}$	Sound intensity
J	–	Number of sources
l	m	Length
L_p	dB	Sound pressure level
m	kg	Mass
$\dot{m}$	$\mathrm{kg/s}$	Mass flow
M	–	Number of microphones
Ma	–	Mach number
$\vec{n}$	–	Perpendicular, norm
p	$\mathrm{kg/ms^2}$	Pressure
r	m	Distance or radius
R	$\mathrm{J/kgK}$	Individual gas constant of air
Re	–	Reynolds number
St	–	Strouhal number
t	s	Time
T	K	Temperature

W	$\mathrm{kg \cdot m^2/s^2}$	Work
x	m	Cartesian coordinate in direction of flow
y	m	Horizontal cartesian coordinate perpendicular to x
z	m	Vertical cartesian coordinate perpendicular to x

Greek Symbols

β	–	Fuel-to-air-ratio (FAR)
γ	–	Adiabatic index for diatomic gases
Δx_m	m	Axial microphone offset
Δx_s	m	Axial source position offset
θ	deg	Emission angle
θ^*	deg	Corrected emission angle
λ	$\mathrm{1/s}$	Wavelength
λ_s	$\mathrm{1/s}$	Trace wave length
μ	–	Bypass ratio
ν	$\mathrm{m^2/s}$	Kinematic viscosity
ξ	–	Cartesian position vector
ρ	$\mathrm{kg/m^3}$	Density
σ_1	–	SODIX slack variable for source directivity
σ_2	–	SODIX slack variable for source distribution

Indizes

B	Bleed air
F	Fuel
i	In
j	Source
l	Lower
m	Microphone
o	Out
p	Propulsive
s	Isentropic
t	Total or Stagnation property
th	Thermal
u	Upper

0	Datum point: Atmospheric condition
2	Datum point: Compressor entry
3	Datum point: Combustion chamber entry
4	Datum point: Turbine entry
5	Datum point: Turbine exit area
9	Datum point: Nozzle exit area
19	Datum point: Bypass Nozzle exit area
I	Engine core duct
II	Engine bypass duct

Abbreviations

APP	Approach ICAO reference measurement point
BPR	Bypass ratio
CB	Cutback ICAO reference measurement point
CSM	Cross-spectral density matrix
DLR	Deutsches Zentrum für Luft- und Raumfahrt
DR	Dynamic range
FAR	Fue-to-air-ratio
FS	Flight Stream
ICAO	International Civil Aviation Organization
LC	Long cowl
NTF	Noise Test Facility
OAPR	Overall pressure ratio
QQ	QinetiQ
RRD	Rolls-Royce Deutschland
RRUK	Rolls-Royce United Kingdom
SARP	Standards and Recommended Practices
SC	Short cowl
SFC	Specific fuel consumption
SL	Sideline ICAO reference measurement point
SN	Snecma
SODIX	Source Directivity modelling in CSM
SPL	Sound pressure level
TOB	Third-octave band
TP	Test point

1 Introduction

The successful introduction of jet engines in civil aviation at the beginning of the 1960s brought the noise emissions of aeroplanes to the center of public attention. The newly introduced aeroengines were considerably louder compared to the formerly used propeller engines due to the noise emanated from the hot jet. In conjunction with an ever increasing air traffic rate - the trend coninuing to this date [3] - public perception was altered: Aircraft noise was no longer just conceived as a side-effect of technological progression, but as a nuisance to be dealt with [14, 33].

The introduction of local regulations at airports was a first counter measure in order to reduce the noise emissions of aircrafts and subsequently ensure the well-being of airport residents. Based on this principle, binding national noise regulations were enacted in many countries during the 1970s [33]. The International Civil Aviation Organisation (ICAO) recognized this fact in 1971 by passing *Annex 16 - Environmental Protection* as an extension of the Chicago Convention. Annex 16 is separated into two volumes which detail the Standards and Recommended Practices (SARPs) set by the ICAO. The first volume deals with technical requirements and procedures for the noise certification of aircraft [16], whereas the second volume contains specifications for aircraft emissions, including noise and pollutants [17].

Contrary to the national regulations, the ICAO annexes are not legally binding. All signees of the ICAO Convention, among which is Germany, however, pledge themselves to transfer the ICAO standards to national law in accordance with Article 37 of the Chicago Convention. Recommended Practices, on the other hand, are merely recommendations that do not have to be implemented. Filing for a SARP discrepancy in the form of a supplement conformable to Article 38 of the Chicago Convention is possible under special circumstances. In any case, the SARPs of Annex 16 act as a certification foundation in international civil aviation, despite lacking international legal obligation [15].

As mentioned before, these noise regulations serve to ensure the physical and psychological health of affected individuals. Therefore, health is the primary concern when analyzing acoustic immision. A continuous noise exposure can have different persistent effects on human organisms. These include syndromes like insomnia, disrupted communicational and attentional abilities and hearing loss. Moreover, affected individuals have shown a higher relative rate of allergies, cardiovascular diseases and depressions. In addition, the short-term exposure to a very loud noise source ($> 85\,\mathrm{dB}$) can cause lasting hearing losses, though this is not a common problem in aviation acoustics [12, 26].

Jet engine acoustics is a field of study which combines methods from acoustics and fluid mechanics to investigate acoustical phenomena of transient flows of jet engines and gas turbines. The research objective is the minimization of the detrimental effects on human health. The Department of Engine Acoustics at the Institute of Propulsion Technology at DLR is dedicated to the research of aeroacoustic phenomena and the development noise reduction technology for modern turbo engines [6].

1.1 Motivation

In order to evaluate the influence of scarfed and serrated nozzle configurations on the propagation of jet noise, a series of stationary experiments were conducted at the QinetiQ Noise Test Facility (NTF) in Farnborough, UK in summer 2012 as part of the OPENAIR European Research Project. The experiments were carried out using different flow conditions, which reference the ICAO noise certification requirements for new aircraft. In addition, tests using a wing model scaled to the reference engine were conducted to study the influence of wing presence on the free jet. The research took place as a joint venture between Airbus, Rolls-Royce UK (RRUK) and Germany (RRD) as well as Snecma (SN), the DLR and QinetiQ (QQ).

1.2 Objective

The scope of this work is to evaluate the acoustic data that resulted from the test. Special emphasis is put on the installation effect of the wing model on the sound field. Furthermore, the resulting flow and sound matrices for different simulated flight conditions and nozzle configurations are analyzed and evaluated regarding their noise effect. This work encompasses only a selection from the test data, considering the vast amount of different configurations that were tested.

1.3 Approach

The following describes the procedure used in this thesis. Chapter 2 explains the theoretical premises required to comprehend this work. It contains a brief introduction to the working principle of modern jet engines, an overview of free jet fluid mechanics as well as an extensive description of aeromachinery acoustics, focussing on the sound radiation of a free jet. Chapter 3 discusses the experimental setup and the various engine configurations used during the tests. In addition, the raw data provided in the scope of this thesis is analysed prior to the sound field assessment in order to evaluate its validity. After all theoretical prerequisites have been introduced and discussed, the analysis results are presented and elaborated in Chapter 4. In addition, observations and recommendations are made regarding future experiments. Finally, Chapter 5 contains a summary of the thesis as well as an outlook on how to proceed with the obtained data.

2 Theory

This chapter deals with the theoretical basics needed for an adequate understanding of this thesis. Section 2.1 gives a brief introduction into the functionality of airbreathing jet engines with a more in-depth view on the working principle of turbofan engines that are commonly used in civil aviation. Jet engines, as their name implies, create a jet of hot and fast gas. The mixing procedure of this jet with the free stream, a phenomenon of fluid mechanics, is described in Sect. 2.2. The central part of this thesis is the noise emanated by the mixing of hot and cold jets. Section 2.3 provides an introduction into acoustics and discusses the various fundamentals and methods associated with it needed for this work. This Section also deals with SODIX, the noise source analysis method developed at DLR.

2.1 Jet Engines

Airbreathing jet engines serve as a means to generate thrust in order to exert a sufficiently large, forward directed force to overcome air resistance, thus enabling flight. In accordance to Newton's third axiom *actio = reactio*, the thrust is created by increasing the momentum $\vec{I}$ of the air passing through the engine, see Eq. 2.1, where m is the mass and $\vec{c}$ the speed of the air. The mass difference between inlet and outlet can be considered neglectable, as the fuel massflow is comparably small to the air flow. Therefore, the momentum can only be raised by increasing the speed of the in-coming gas. The outlet momentum has to be of greater magnitude than the inlet momentum at all times to generate a forward directed force [4].

$$\vec{I} = m \cdot \vec{c} \tag{2.1}$$

The thrust force $\vec{F}$ is the time derivative of the momentum, Eq. 2.2. This relation is also called the principle of linear momentum in fluid mechanics [4].

$$\vec{F} = \frac{d\vec{I}}{dt} = \int_A \rho \cdot \vec{c}(\vec{c} \cdot \vec{n}) dA \tag{2.2}$$

For an enclosed control volume, Eq. 2.2 can be rewritten as follows [4]:

$$F = c_9 \cdot (\dot{m}_0 + \dot{m}_F - \dot{m}_B) - c_0 \cdot \dot{m}_0 + A_9 \cdot (p_9 - p_0) \tag{2.3}$$

Here $\dot{m}_0$ is the main mass flow, $\dot{m}_F$ the fuel mass inflow, $\dot{m}_B$ the bleed air offtake, A_9 the nozzle surface area and p the pressure at in- and outlet respectively. Equation 2.3 can be simplified further by neglecting the fuel and bleed mass flows, as they are comparably small to the main mass flow as well as assuming an adapted nozzle, so that the static pressure at the nozzle outlet is equal to atmospheric pressure, i.e. $p_9 = p_0$. This results in the simplified thrust equation 2.4 [4].

$$F = \dot{m}_0 \cdot (c_9 - c_0) \tag{2.4}$$

From Eq. 2.4 it can easily be deduced that thrust can be raised by either increasing the mass flow $\dot{m}_0$ or the airspeed difference between inlet and outlet. This relates back to the definition of momentum in Eq. 2.1.

The air passing through the jet engine is accelerated through a thermodynamic process chain by converting thermal energy into kinetic energy (jet) and mechanical work (fan). A jet engine is thus a heat engine. The thermodynamic cycle consists of compression, combustion and expansion stages and is known as the Brayton or Joule cycle. The ideal cycle is comprised of an isentropic compression in the compressor stages, an isobaric combustion in the combustion chamber and an isentropic expansion in the turbine stages of the engine. Work can be extracted from this cycle, because the isobars are diverging for increasing entropy. This means that the enthalpy difference of two pressures is bigger for larger entropies, i.e. in the turbine stages after combustion, where work is extracted from the cycle.

Figure 2.1 depicts the ideal and real Brayton cycle. The ideal process is marked by isentropic datum points indexed P_s. The real cycle, marked in red, follows the same general thermodynamic procedure as the ideal one and is indicated by unindexed datum points P. The real processes are no longer isentropic or isobaric, however, resulting in pressure losses and entropy growth which in turn increase the enthalpy needed for compression and reduce the enthalpy that can be extracted from the cycle in the turbine stages. This is directly reflected in a decrease of thermal efficiency.

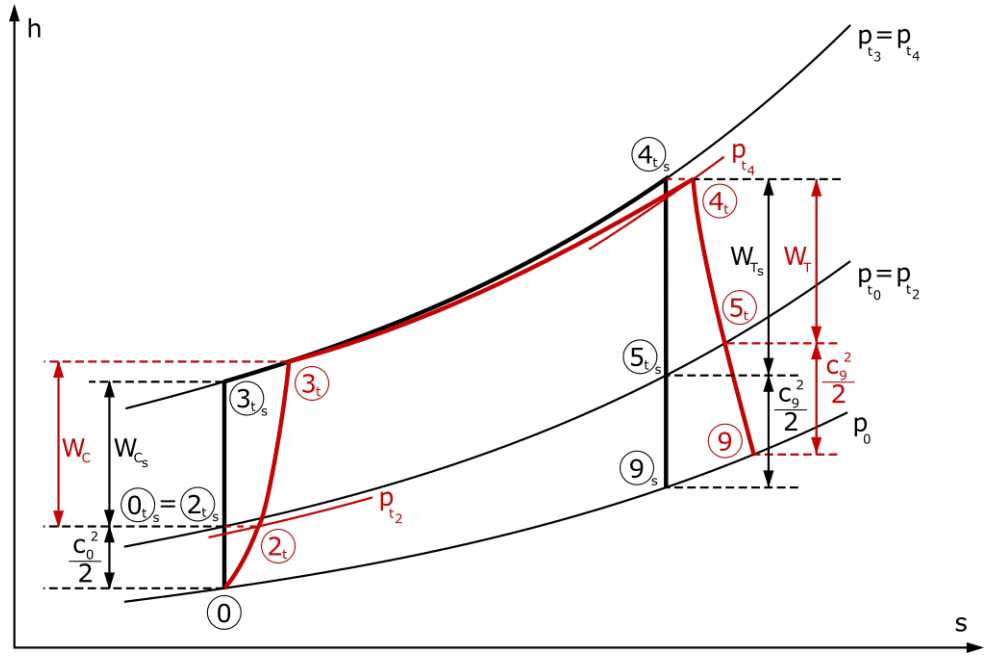

Figure 2.1: *Ideal and real Brayton or Joule cycle.*

Figure 2.2 shows the cross-section of a three shaft turbofan engine, a specialty of Rolls-Royce [4], pointing out the different turbo-components of an aeroengine.

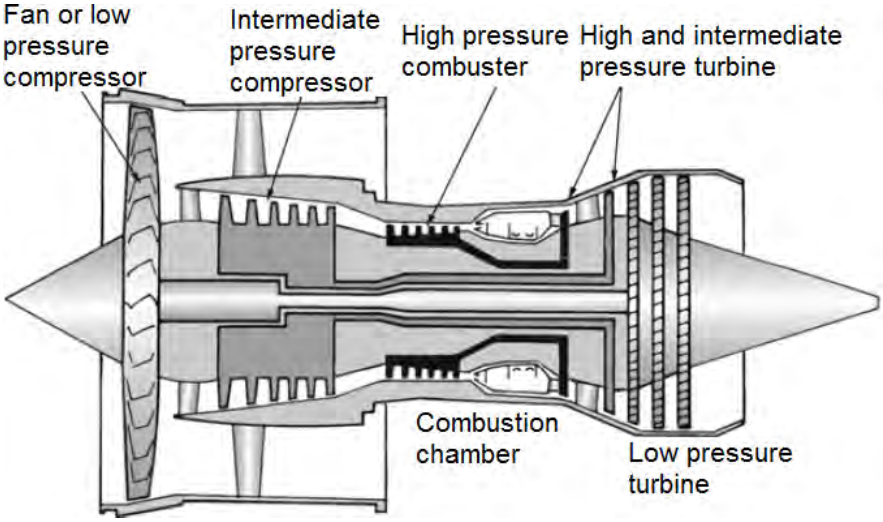

Figure 2.2: *Cross-section of a typical turbofan engine, showing the thermodynamic components. (Translated from [4])*

There are two main efficiencies defined for turbomachinery to rate the performance of an engine. The thermal efficiency (or cycle efficiency) quantifies, how much of the thermal energy fed into the thermodynamic cycle $\dot{Q}_i$ can be converted into effective work W_U, thus describing the quality of the thermodynamic

cycle (Eq. 2.5). Here, β is the fuel-to-air-ratio (FAR) and H_c the heat of combustion. The thermodynamic efficiency of an engine can be increased by either increasing the nozzle exit velocity c_9 of the air or decreasing the FAR, assuming that $F, c_0, H_c = const$. Decreasing the FAR also lowers the specific fuel consumption (SFC) [4].

$$\eta_{th} \equiv \frac{W_U}{\dot{Q}_i} = \frac{c_9^2 - c_0^2}{2 \cdot \beta \cdot H_c} \tag{2.5}$$

The second performance indicator is the propulsive efficiency (Eq. 2.6). It describes how much of the thermodynamic work W_U produced is converted into usable thrust W_F. The propulsive efficiency is greatest for $c_9 \approxeq c_0$. This directly conflicts with the optimisation of the thermal efficiency as described above, meaning that an increase in propulsive efficiency always goes in hand with a decrease in thermal efficiency.

$$\eta_p \equiv \frac{W_F}{W_U} = \frac{2}{1 + \frac{c_9}{c_0}} \tag{2.6}$$

Both efficiencies can be combined into the overall efficiency η of an engine, Eq. 2.7.

$$\eta = \eta_{th} \cdot \eta_p \tag{2.7}$$

Since the propulsive efficiency can only be enhanced by modifying c_9, this value is no longer available for improving thermal efficiency. Therefore, the latter may only be increased by lowering the FAR β, assuming $c_0, H_c = const$. This is possible by either increasing the mass flow $\dot{m}_0$ or by increasing the overall pressure ratio (OAPR) of the compressor, thus raising the temperature at the compressor outlet and reducing the amount of heat needed for combustion.

In modern civil aviation, turbofan engines are the most commonly used engine type. These double-shafted machines consist of a core engine that is encased by a bypass duct and make use of high bypass ratios (BPR) μ. This allows increasing $\dot{m}_0$, while reducing the average exit velocity c_9 and c_{19}, thus providing an optimal propulsive efficiency while maintaining a high level of thrust. Moreover, the higher throughput reduces the FAR, therefore lowering the SFC and improving thermal efficiency. Turboprop engines, having a propeller instead of a fan and lacking an outer nacelle, are another engine type that is used for smaller and lighter regional aircraft, as their maximum airspeed cannot match that of turbofan engines.

The turbine of the core engines powers the core compressor, the fan and all secondary equipment, e.g. the integrated drive generator for board power generation. The remaining work available is converted into accelerated air, which results in the core thrust. The bypass produces thrust via large mass flows $\dot{m}_{II}$ and small velocity differences, as the inlet surface area is comparably large to that of the core engine, while the OAPR of the fan is almost neglectable compared to that of the core compressor stages. Since the introduction of turbofan engines, the trend has moved to everincreasing bypass ratios, as this promotes the aforementioned advantages of making use of a large bypass mass flow. This comes with some repercussions, however. As the bypass ratio grow larger, so does the nacelle front surface area, hence increasing aerodynamic resistance and weight of the engine. This in turn entails a reduced ground clearance and larger supporting structures to carry the heavier nacelle. Both advantages and detriments have to be thoroughly considered while designing an engine to reach an optimally satisfying end product.

2.2 Fluid Mechanics

Many processes in fluid mechanics are very turbulent and thus highly stochastic in nature. Though computational fluid dynamics (CFD) has improved a great deal over the last decades, it still is advisable to approach some phenomena with experimental analysis, especially when a large amount of test cases is involved, as the cost of CFD has the potential to scale considerably steeper with increasing computation time. Experimental work, on the other hand, has a larger forward fixed cost, but is comparably more affordable as tests are carried out. In addition, experimental work tends to produce more reliable results, as CFD analysis always incorporates assumptions, e.g. turbulence modellation [34].

2.2.1 Similitude

Due to physical constraints, it is oftentimes not feasible to mount a full scale analysis of turbomachinery. The scaled models, that are subsequently used, possess different flow characteristics. Therefore, it is an inherent requirement of each test, that the data collected during model testing is comparable to the full scale model in its physical properties. There exist several dimensionless quantities that

address this matter. Only if those quanitities agree for both model and full-scale experiment, can the two can be considered having equal flow properties. This means, that the values of specific geometrical and physical quantities have to be equal for each flow point [31].

The relevant dimensionless quantities for this work are the Mach number Ma, the Reynolds number Re and the Strouhal number St. These quantities are derived from dimension analysis, either by applying the Buckingham π theorem or using the matrix method [27, 31]. The Mach number is the dimensionless relation between the local air velocity c and the speed of sound a, see Eq. 2.8.

$$Ma = \frac{c}{a} \text{ where } a = \sqrt{\gamma RT} \tag{2.8}$$

For an ideal gas, the speed of sound is dependent on the local static temperature T, the individual gas constant of air R and the adiabatic index for diatomic gases γ [27]. Since it holds that the latter two values are constants, hence the speed of sound is proportional to the temperature $a \sim \sqrt{T}$. Because the speed of sound is much higher in the hot jet of a turbofan engine, the outlet flow does not reach supersonic speed.

The dimensionless Reynolds number Re can be interpreted as the ratio of momentum forces to viscous forces of a specific flow condition, Eq. 2.9.

$$Re = \frac{c \cdot l}{\nu} \tag{2.9}$$

The momentum forces equate to the speed of the fluid c and a characteristic length l, which is typically lower for the experiment model. The viscous forces are represented by the kinematic viscosity ν. The Reynolds number is the paramount dimensionless quantity in fluid mechanics, as the flow condition of two geometrically similar bodies of different scale are considered comparable, provided that Re is equal for both cases. This can be achieved by varying the flow speed c or by using a fluid with different kinematic viscosity ν [31].

The Strouhal number St, also called dimensionless frequency, is the ratio of the path l that a particle travels with speed c to the frequency f of a transient process, e.g. the frequency of vortex shedding due to air flow around an object, Eq. 2.10 [31].

$$St = \frac{l \cdot f}{c} \tag{2.10}$$

Besides the Reynolds number, the Strouhal number is of importance for jet geometry scaling. It allows frequency comparisons between jets of different scale and flow velocity.

2.2.2 Free Jet Fluid Mechanics

As air exits the engine nozzle, it enters into a stationary or comparably slow and parallel moving environment, resulting in a highly turbulent free jet. A shear layer is formed between the fluids of different velocities. This shear layer facilitates particle exchange through turbulent friction, thus aligning the velocity of both the jet and free stream. At the center of the nozzle is a conically shaped area, in which the velocity of the jet equates to that of the jet at the outlet plane. As such, this area is also known as the potential core of the free jet. The core's diameter decreases with increasing distance to the nozzle, its dissipation marking the end of the continous area and the begin of the dissipation area. Contrarily, the toroidally shaped mixing layer's volume increases; as the jet becomes slower, it grows steadily broader, until it fully dissipates into the surrounding after a distance of approximately $x/d \approx 10 - 100$. The dissipation length depends on the speed difference of jet and free stream [30, 31].

The jet of modern bypass turbofan engines develops following the same principle as described above. However, due to turbofan engines having two separate nozzles - for core and bypass flow - two mixing processes take place: The very hot and fast core air flow is mixed with the slower and colder bypass flow, which in turn is mixed with the even colder and slower free air stream. As such, there are several interfaces between hot and cold flows of differing velocity, which give rise to a number of turbulent mixing regions. In addition, the cowl configuration influences the mixing process. There exist two notable cowl designs in modern turbofans. For the short-cowl configuration (SC), also known as separate nozzles, the core duct extends beyond the bypass duct, as depicted in Fig. 2.3. Therefore, the bypass flow mixes with the free jet first (1). The core flow is then encased by this slow and cold pre-mixed flow (2), which lowers overall acoustic emission (see Sect. 2.3). The mixed flow of boths jets (3) will dissipate into the atmosphere in a large-scale, low-velocities process (4) [4, 26, 33].

The second configuration is called long-cowl (LC), common or integrated nozzle. Here, the bypass duct extends beyond the core duct, allowing a pre-mixing of the

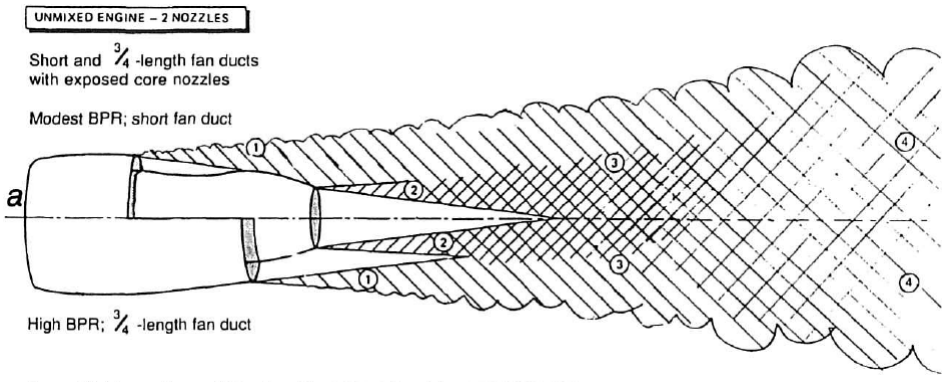

Figure 2.3: *Short-cowl nozzle configuration. The core duct extends beyond the bypass duct [26].*

two jets (2), which decreases the average speed and homogenizes the temperature distribution. As such, the exiting common jet is colder and slower as for the SC nozzle (1), thus emitting less noise. The mixing process can be accelerated by utilizing dedicated subsidiary structures, e.g. chevron nozzles or forced mixers. Again, the mixing is completed, when the jet has mixed with the atmosphere (4). The advantage in noise emission for this configuration is achieved by elongating the bypass duct, which means a heavier and more expensive engine, which in turn raises the SFC [4, 33].

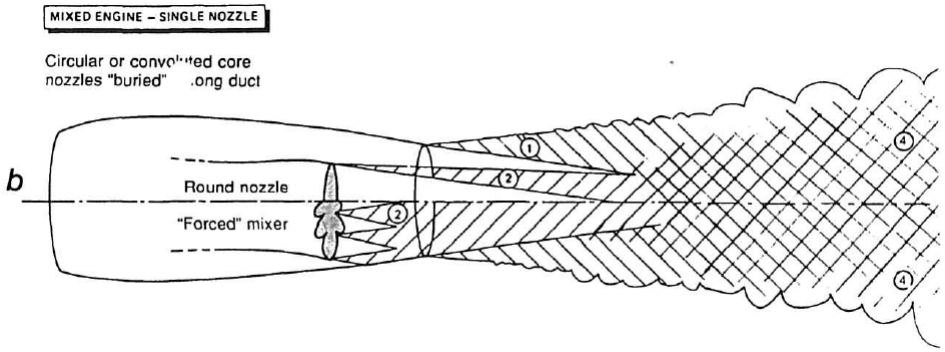

Figure 2.4: *Long-cowl nozzle configuration. The bypass duct extends beyond the core duct [26]*

.

In modern conventional aircraft configurations, engines are typically mounted under the wing. As such, the jet exiting the engine is influenced by the presence of the wing, especially so during take-off and landing, when flaps are deployed. The effects on jet flow and noise radiation are summarized under the term 'installation effects' [20]. When the jet mixing turbulent structures are broken and refracted by the wing and flaps, additional swirl vortices are created that travel

downstream [24]. The flap trailing edges create an additional set of rotating vortices similar to those present at the wing tip [24, 36]. Furthermore, a boundary layer forms on the under side of the wing. Due to the presence of the highly turbulent jet, counter-rotating eddies are formed inside this boundary layer, that travel downstream and burst, when their circulation becomes too low [30].

As a sidenote, some aircraft configurations use the propulsive system's exhaust to increase the lift force of flap systems. This is achieved by letting the high flow velocity and turbulence levels of the exhaust flow pass along the aerofoil and high lift surfaces, thus increasing the maximum lift coefficient. This reduces the required take-off and landing speeds of the aircraft, allowing operation on shorter runways at the cost of an increased noise radiation [8].

2.3 Acoustics

This chapter deals with basic acoustic assumptions in Sect. 2.3.1 and applies them to the specific case of jet exhaust noise in Sect. 2.3.3. It further introduces the noise regulation concepts devised by the ICAO in Sect. 2.3.2 and highlights the reference measurement points and their importance during civil aeroengine design. Finally, the working method as well as in- and output of the SODIX routine for source directivity analysis are explained in Sect. 2.3.4.

2.3.1 Basics

Sound, as humans perceive it, is a sinusoidal pressure fluctuation of the air between an emitter and a receiver, propagating as sound waves. Compared to the atmospheric static air pressure, these fluctuation are of rather small magnitude and thus result in only minor air movements. The human ear, acting as a sound receiver, is able to tolerate amplitudes that differ more than a million times between the threshold of hearing and the onset of physical pain, and perceives frequencies between approximately 20 Hz to 20 kHz, also called the hearing range. Generally, if sound can be considered subjectively unpleasant, it is referred to as noise. According to the Webner-Fechner law, human sound perception is proportional to the logarithm of the stimulus, similar to e.g. the haptic sense. For this reason, the quantity used to describe the sound pressure level (SPL) L_p is defined as the logarithm of the root mean square sound pressure p scaled with the

threshold of hearing p_0, Eq. 2.11 [14, 25, 33].

$$L_p = 10 \log_{10} \frac{p^2}{p_0^2} = 20 \log_{10} \frac{p}{p_0} \tag{2.11}$$

In order to represent the logarithmic sound perception, the unit of measurement for the SPL is the decibel dB. It uses a logarithmic ratio of the actual SPL to an arbitrary reference value, the threshold of hearing set at 20 μPa [33]. For easier management, acoustic energy is integrated over certain frequency bands. An octave corresponds to the doubling of the frequency and can be further divided into one-third octave bands (TOB). The TOBs used for this work are in accordance to EN ISO Norm 266 [18] and are listed in Table A.2. In international standardisation, approximately 11 kHz have been established as the upper limit of effective noise [33], taking hearing deterioration with age into account.

The sinusoidal pressure fluctuation is characterized by its frequency and amplitude. The wavelength λ of a sound event is equal to the quotient of the speed of sound a and frequency f, $\lambda = a/f$. The sound intensity then is defined as the product of mean square sound pressure p and particle velocity v, $I = pv$. When sound propagates in the atmosphere, its intensity decreases due to two effects. Firstly, as sound is emitted from a source, its intensity, i.e. its sound power per unit area, diminishes as it spreads out over a larger surface, the sound intensity quartered for each doubling of the distance to the source. Secondly, sound propagation is subject to atmospheric attenuation. Due to internal friction in the fluid, the sound wave amplitude is reduced. The amount by which the intensity of sound diminishes is mainly dependent on the frequency of the sound, being of greater magnitude for high frequencies as well as temperature, pressure and humidity, thus making air effectively a low pass filter over long ranges [29, 38].

2.3.2 ICAO Noise Certification

As explained in Chapter 1, there is no international legislature in aviation. The annexes published by the ICAO, however, are binding for signees of the ICAO convention, who comprise of almost all states conducting aviation. The ICAO is a special UN-agency, committed to the development of standardisation processes. The developed procedures (SARPs) are laid down as annexes to the *Chicago Convention* [15, 29]. As such, *Annex 16 - Environmental Protection* is the internationally agreed basis for noise related certification criteria during research, development

and product life cycle. Chapter 4 of the first volume of said annex deals with the aircraft noise of subsonic jet aeroplanes whose certification has been submitted after January 2006 and is therefore the most contemporary design limiter [16, 38]. The annex lists three reference measurement points at which noise criteria have to be met. These points are:

- **Lateral full-power reference noise measurement point**, also labelled side-line point (SL), at a line parallel and 450 m to the runway center line, where the noise level is maximum during takeoff;
- **Flyover reference noise measurement point**, also labelled cutback point (CB), at the extended runway center line after 6.5 km from the start of roll;
- **Approach reference noise measurement point**, approach point (APP) at the extended runway center line, 2 km from the threshold.

The maximum noise levels allowed depend on the reference point and the maximum take-off weight (MTOM) of the aircraft and the engine configuration. They are listed in Table 2.1.

Table 2.1: *Maximum noise levels for aircrafts whose certification has been submitted after January 2006, based on reference point and MTOM [16].*

M = Maximum take-off mass in 1 000 kg		0	20.2	28.6	35	48.1	280	385	400
Lateral full-power noise level (EPNdB) All aeroplanes		94			80.87 + 8.51 log M				103
Approach noise level (EPNdB) All aeroplanes		98			86.03 + 7.75 log M			105	
Flyover noise levels (EPNdB)	2 engines or less	89			66.65 + 13.29 log M				101
	3 engines	89			69.65 + 13.29 log M				104
	4 engines or more	89			71.65 + 13.29 log M				106

In addition, the annex gives details on possible amendments if noise limits are exceeded, the flight procedures and the testing conditions such as atmospheric conditions and aircraft speed [16].

2.3.3 Free Jet Acoustics

Section 2.2 already touched on the subject of noise generation due to turbulent flows. This section expands on this knowledge and deals with the manifold sound sources of an isolated aeroengine jet and under the effects of a wing. When assessing the sound field of a jet, it has to be considered that the noise generated

by other sources like the turbine and combustion process can be of greater magnitude than the jet noise, essentially drowning it out. As mentioned before, this happens especially during low thrust flight, as then the exhaust velocity is low and the subsequent mixing process is comparably slow and quiet. This deviating influence has to be segregated to enhance measurement quality. For the tests this work is based on, this factor can be neglected, as there are no turbomachinery components in the experiment setup.

Single stream jet noise

The term "jet noise" refers to sound sources in the mixing exhaust jet and shock induced noise from an inefficiently expanding supersonic flow [33]. The latter is neglectable in the scope of this work, as it only deals with jet exhaust velocities lower than the local speed of sound. Jet mixing noise is caused by pressure fluctuations due to mixing turbulence, which are created during the mixing process and propagate as sound waves through the surrounding atmosphere [29, 36]. Similar to other turbulence induced sound, jet noise has a distinctive broadband noise spectrum, as the eddies created during the process increase in size while travelling downstream, see Fig. 2.5 [33]. Figure 2.9 on page 19 shows the frequency spectrum of a common jet.

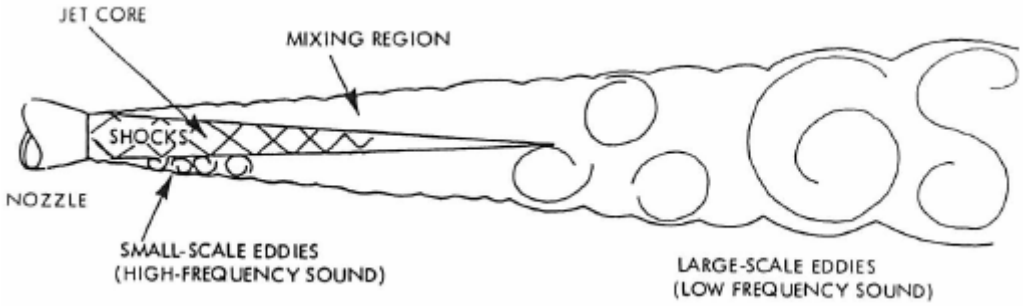

Figure 2.5: *Jet mixing process, showing shock induced noise and eddy dissipation [33].*

According to Lighthills *Theory of Sound* [19], the fluctuating shear stress is responsible for the generation of broadband noise, its intensity being related to the eighth power of the jet velocity, $I \sim c^8$. Experimental studies showed, that this assumption holds true for all but very low and high frequencies. For low frequencies, this deviation most likely occurs due to other sound sources drowning out the jet noise, resulting in $I \sim c^5$. For high frequencies, however, the speed of the convected eddies is greater than the local speed of sound with which the

sound waves propagate into the acoustic farfield. This velocity difference results in a different ratio of approximately $I \sim c^3$ [26, 33].

The directivity of jet noise is similar over all TOB. There is a peak in the center of the aft quadrant, from whence there is a gently decline towards the forward quadrant. Downstream, the noise rapidly diminishes, before terminating in a zone of almost no sound between 15° and 10°, called the *cone of silence*. The cone results from refraction effects between high-speed jet and atmosphere. Studies referenced by Smith [33] showed, that jet noise increases for increasing temperature, whereas the opposite holds true for decreasing temperature. Smith attibutes this phenomenon to the variation in the local speed of sound, coupled with the hot-cold fluid boundary. However, this effect can be considered second-order, because the differences in temperature profiles for aeroengines do not differ considerably between operating points. Figure 2.6 shows the general directivity of a low and high bypass engine, respectively.

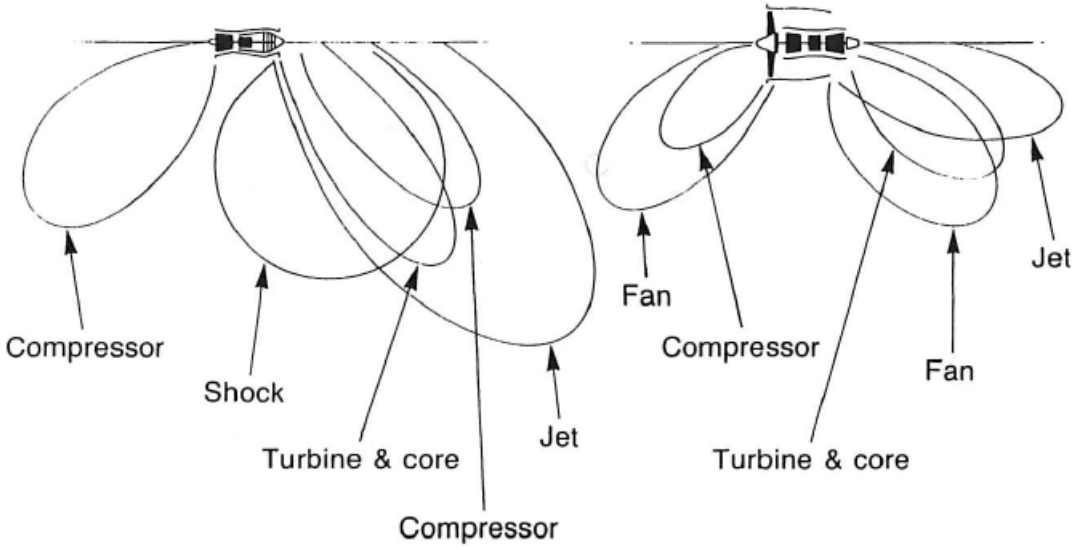

Figure 2.6: *Sound directivity of a low (left) and high (right) bypass engine [33].*

Two stream jet noise

As explained in Sect. 2.1, turbofan engines with a high BPR are most commonly used in modern civil aviation. The accompanying reduction of flow velocity results in a significant sound level reduction, since jet noise is generally assumed to be proportional to the eighth power of the speed of sound. During the last 35 years, noise levels of turbofan engines have been reduced by up to 24 dB [29, 33]. Despite this decrease, turbofan jet noise alleviation still faces manifold challenges.

As the jet is exhausted through two separate, usually axially staggered nozzles with different speed and temperature, a multitude of fluid interfaces and subsequently potential noise sources is generated. Since turbulence in the mixing process is responsible for jet noise generation, the sound level can only be reduced by decreasing the turbulence. However, the turbulence occurs far downstream of the nozzle, rendering structural provisions inside the jet itself unfeasible. Instead, the turbulence generation can be moved upstream by utilizing special mixing devices at the nozzle plane. Furthermore, turbulence reduction is possible by decreasing the velocity of the jet, which, assuming constant thrust, can only be accomplished by increasing the mass flow $\dot{m}_0$ and thus the BPR. Figure 2.7 shows the achievable noise reduction by encasing the core flow in a slower bypass flow. Note, how the SPL reduction of the high-frequent upstream source becomes more prominent for decreasing bypass flow velocity. An additional challenge is the low frequency portion of the emitted broadband noise, which is generated with great intensity, but is only affected by atmospheric attenuation to a minor degree.

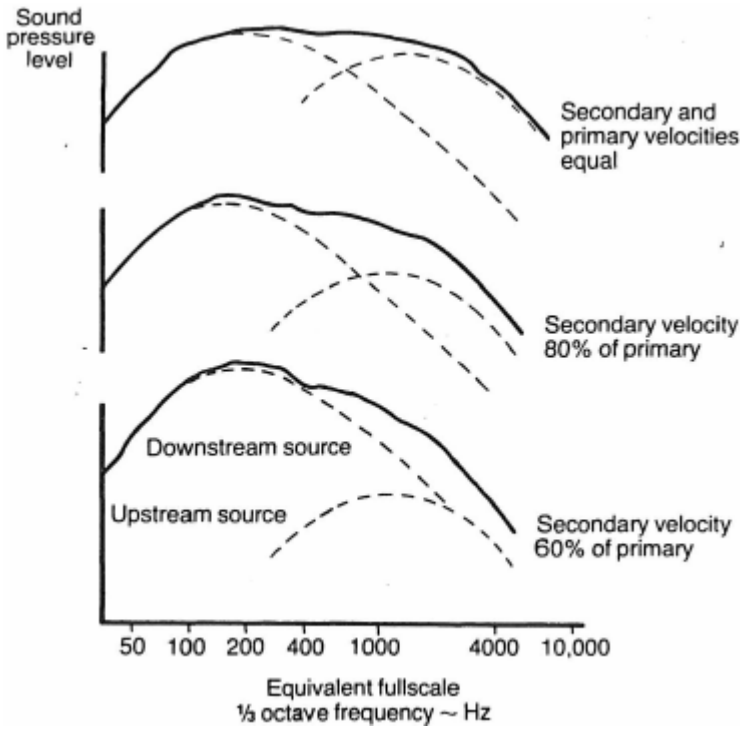

Figure 2.7: *Reduction in noise radiation by using a mantling bypass flow of different velocities [33].*

Experimental investigation of a LC aeroengine showed two mixing regions downstream of the nozzle that are primarily responsible for jet noise, Fig. 2.8. The first peak in the SPL occurs in close proximity to the nozzle, likely due to the fan flow

mixing with the environment, the second at approximately ten nozzle diameters downstream the exhaust plane, caused by the mixing of the fully developed jet with the atmosphere. Further investigation by variation of the ratio of core and bypass flow velocity yielded, that the first source emits mainly high-frequency noise, whereas the second one radiates mostly low-frequency noise. This is attributed to the size of the eddies caused by the mixing shear layers. At the first position, the jet velocity is much greater than the surrounding velocity, thus promoting only minor mixing and subsequently small eddies. At the second position, the mixing is of greater magnitude, the turbulence coarser, which facilitates the generation of larger eddies. Further credence is given by source localisation studies that identify two dominant mixing regions among a number of insignificant sources [26, 28, 29, 33].

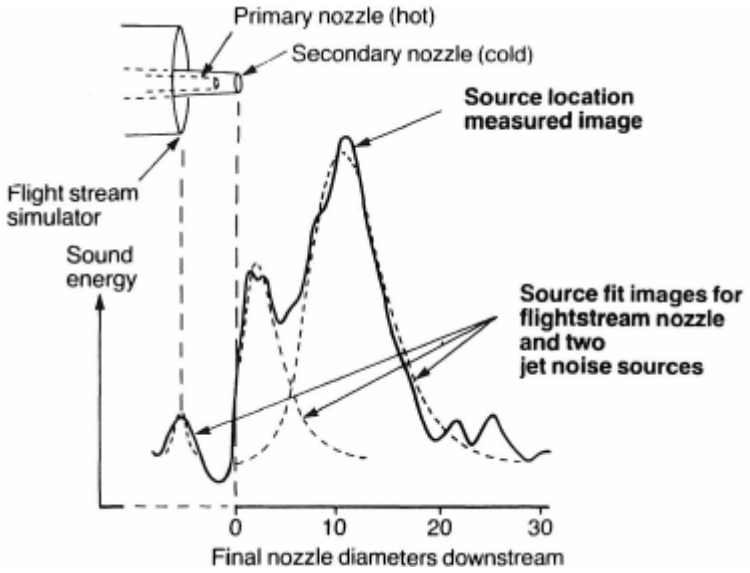

Figure 2.8: *Mixing regions of a two-stream exhaust engine, produced during an experiment at the Noise Test Facility in England, 1976 [28, 33].*

Interaction noise

Interactions caused by engine installation are called Propulsion Airframe Aeroacoustic (PAA) interactions [21]. Nelson [26] identifies two major noise sources due to jet/wing interference. Firstly, the interaction of the jet with the wing surface leads to large-scale turbulence which results in an up to 10 dB SPL increase. However, due to the formation of comparably big eddies, the increase happens at very low frequencies that can well be beyond the audible range. The second effect is caused by interaction of the jet with wing flaps and is thus primarily of concern during take-off and landing operations, when flaps are deployed. Depending on the engine position relative to the wing, it might also occur during

flight. This effect has a magnitude of the same order as the first one, however within the audible range. It can be alleviated or even completely obviated by considering engine placement during design. Unoptimised installation may act as if an additional engine was mounted [26].

Figure 2.9 shows a typical farfield SPL spectrum of an isolated jet in addition to a jet affected by PAA interactions, taken from Nelson [26], where the aforementioned effects can be observed. Similar observations regarding the spectrum have been made by other authors ([1, 5, 9]), the SPL maximum ranging between $f = 100 \ldots 2000\,\mathrm{Hz}$, depending on jet speed, temperature, immission angle and experiment setup.

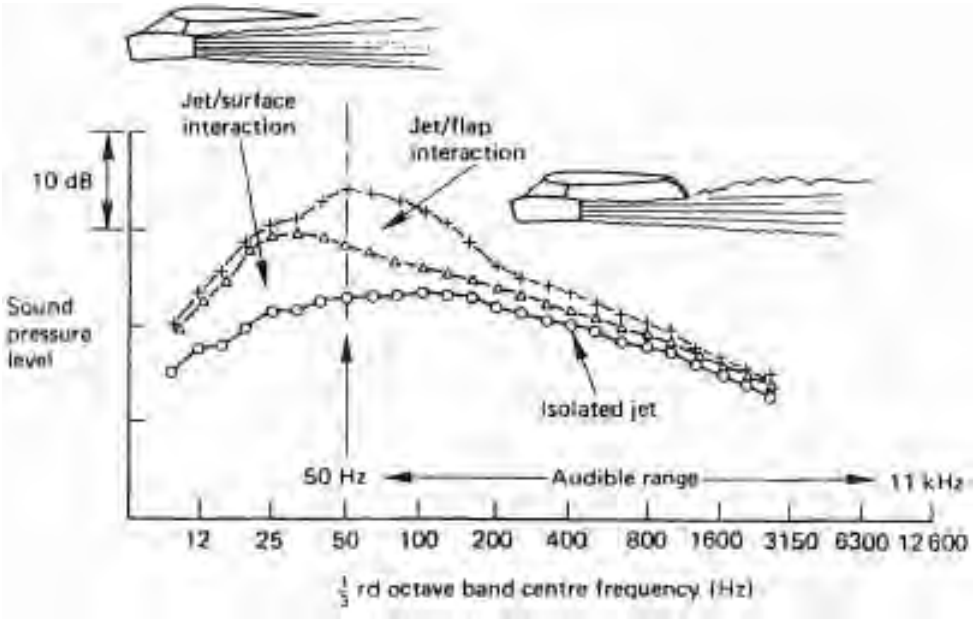

Figure 2.9: *Farfield frequency spectrum of an isolated jet and with installation effects [26].*

Additionally, sound waves are subject to reflection, refraction and diffraction effects. Reflection may cause the sound source to appear louder and change directivity [13] or create the pretence of a second sound source [24]. Incidence and exit angle correspond, while part of the impinging sound is absorbed by the reflection surface [25]. The wing acts as a natural sound reflection surface and as such can be expected to alter the SPL of the installed jet. When a sound wave travels through two different, permeable fluid media, it is refracted [24], altering the incidence angle of the sound wave. As the core, bypass and free flows are all of a different velocity and temperature, refraction effects can be expected in jet acoustics. Lastly, sound waves are able to bend around solid objects, an effect

called diffraction [25]. Diffraction occurs at the nozzle circumference and causes sound to be emitted into the forward quadrant as well as at the wing and pylon, where sound is diffracted laterally and skyward, and is thus of no consequence for ICAO noise measurements.

During interaction noise tests using a full installation, i.e. wing, fuselage and empennage, Bashforth [1] observed an increase in SPL ranging from 1 to 4 dB for very low frequencies ($f \approx 100\,\text{Hz}$) and high frequencies ($f \approx 6.3\,\text{kHz}$) respectively. The latter effect is attributed to jet noise reflection by the wing, as the sources close to the nozzle tend to be of high frequency.

2.3.4 SODIX

The SODIX algorithm (named for SOurce DIrectivity modelling in cross-spectral matriX) has been developed at DLR. SODIX is used to determine the sound directivities of broadband sound sources of an aeroengine. Other contemporary methods are the polar correlation technique and beamforming, both of which can only be applied assuming uniform sound directivity [22]. This section gives an overview of the working principles of the routine and details the in- and output of the algorithm. For further information regarding the derivation of the algorithm and comparisons with other deconvolution methods, refer to the papers published by DLR [10, 11, 22].

Method

The algorithm is based on modelling the cross-spectral matrix (CSM) of the microphone signals using a set of linear point sources with unknown directivities along the engine center axis. The CSM is a three-dimensional matrix, wherein each frequency band is represented by a matrix C_{mn} of M by M complex values, where M is the number of microphones in the microphone array [22]. The matrix is Hermitian, or self-adjoint, meaning that the element of the m-th row and the n-th column is equal to the complex conjugate of the n-th row and the m-th column: $c_{mn} = \overline{c_{nm}}$. This entails that the elements along the matrix' diagonal, that represent the microphone auto spectra, must be real, as they are their own complex conjugate. The CSM is a representation of the phase and amplitude ratio of all microphones among each other.

Contrary to deconvolution methods, SODIX does not assume a uniform source strength, but instead models the CSM C_{mn}^{mod} using the steering vectors g_{jm} and the point source strength D_{jm} of the sound pressures of each source j towards each microphone m, Eq. 2.12.

$$C_{mn}^{\text{mod}} = \sum_{j=1}^{J} g_{jm} g_{jn}^{*} D_{jm} D_{jn} \tag{2.12}$$

The complex steering vectors are defined as in Eq. 2.13, with $r_{jm} = \left|\vec{\xi}_j - \vec{\xi}_m\right|$ being the distance between microphone and source position and $k = 2\pi f c^{-1}$ the angular wavenumber [11].

$$g_{jm} = \frac{1}{r_{jm}} e^{ikr_{jm}} \tag{2.13}$$

The goal is to reconstruct the measured CSM C_{mn} such that the mean square error $F(D)$ between the measured and modelled matrix is minimized, Eq. 2.14 [11, 22].

$$F(D) = \sum_{m,n=1}^{M} \left| C_{mn} - C_{mn}^{\text{mod}} \right|^2 \tag{2.14}$$

This problem is not mathematically well-posed, as there can potentially be more unknown source strengths D_{jm} than there are microphones M and point sources J, for solving for Eq. 2.14 results in a set of JM non-linear equations [10]. For this reason, smoothing functions G_1 and G_2 were introduced, assuming an even distribution of source directivity (G_1) and source distribution (G_2) [22]. Further iterations on the SODIX methods introduced a cost function F to restrain the solver from negative solutions for D, as it now solves for $d_{jm} = \sqrt{D_{jm}}$ [11]. The cost function then is

$$F(d) = \sum_{m,n=1}^{M} \left| C_{mn} - \sum_{j=1}^{J} g_{jm} g_{jn}^{*} d_{jm}^2 d_{jn}^2 \right|^2 . \tag{2.15}$$

Using the smoothing functions, the equation that has to be minimized instead of Eq. 2.15 is defined as

$$G(d) = F(d) + \sigma_1 G_1(d) + \sigma_2 G_2(d). \tag{2.16}$$

The slack variables σ_1 and σ_2 in Eq. 2.16 are used to control the intensity of the smoothing. σ_1 controls the source directivity smoothing; with increasing values greater than zero, the directivity of each source becomes smoother. Values $\sigma_1 = 0.0001 \ldots 1$ are typically used. σ_2 controls the source distribution smoothing;

with increasing values greater than zero, the distribution of the sources becomes smoother. Suprisingly enough, the solution also converges when disregarding the smoothing functions ($\sigma_1 = \sigma_2 = 0$) [11]. Figure 2.10 illustrates the SODIX source model, calculating the source strength D_{jm} towards the individual microphones.

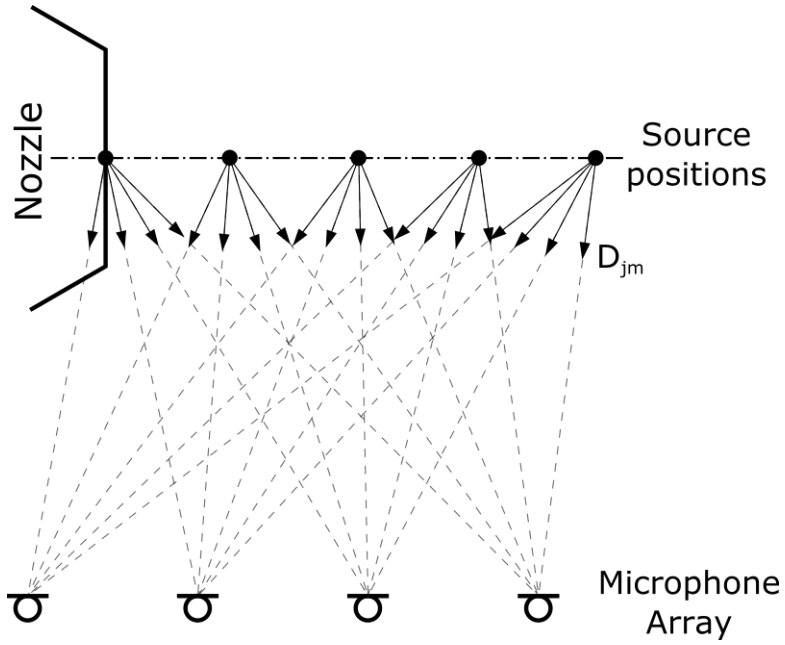

Figure 2.10: *Illustration of the sound source directivity calculation as done by SODIX.*

Input

The SODIX algorithm requires several input parameters. To calculate the modelled CSM, it requires the measured CSM for all narrow bands that are to be simulated as well as the cartesian coordinates of the microphones used in the experiment. In addition, the cartesian coordinates of the source positions have to be provided. The source positions are allocated on a straight line and have to be specified for each TOB, but the position of individual points can be chosen arbitrarily. Studies showed, that the outcome of the SODIX calculation is rather independent on the selected grid [11], as long as some requirements are fulfilled: The spacing between the sources is suggested to be $\Delta x_s = 0.25\lambda \ldots 0.4\lambda$ with corrections for very low and high frequencies as to not dilute results and enhance calculation time respectively [22]. In addition, the source position grid needs to be of sufficient length to cover all sound events prevalent in the raw data. Otherwise, the algorithm assumes sources at the far end of the source grid in order to

account for sources outside the domain, resulting in source clustering that adulterates the directivity plots.

Due to the discrete one-dimensional nature of the source grid, actual sources outside of the assumed straight grid line are projected onto the individual source positions. The projection is a function of the relative emission angle between source and microphone, as SODIX projects the true source onto the two source points closest to the line directly connecting both. This means that the actual position of the sound event may deviate from the one given by the SODIX calculation. The source projection has to be considered during SODIX plot interpretation. Figure 2.11 illustrates this circumstance. As grids become denser for higher frequencies, this effect is less pronounced at higher TOB, as the distance between individual source points is reduced and as such the likeliness of noticeable projection decreases. This is why plots appear to be more blurred at low frequencies while having clearer sound events at higher ones.

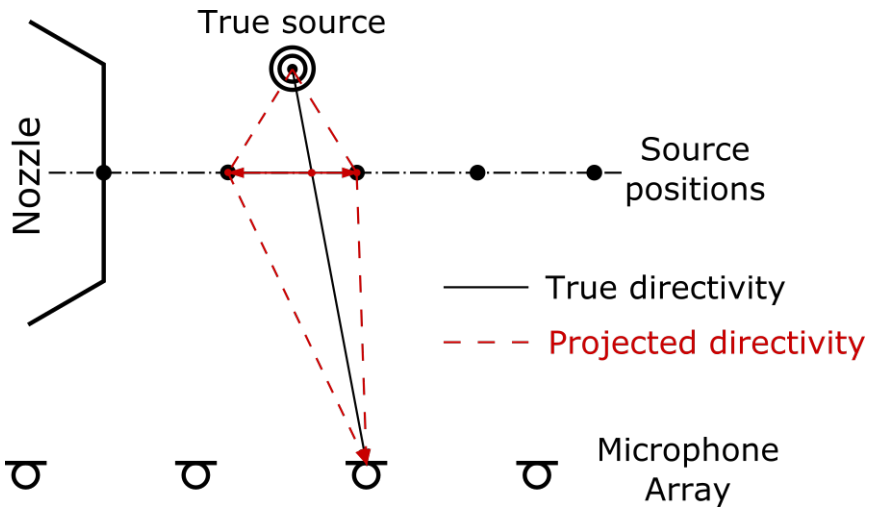

Figure 2.11: *Sound source projection in SODIX due to one-dimensional source position grids.*

The SODIX simulation is implemented as a MATLAB script that requires an *sdx*-file as control file. This file contains configuration parameters, such as the simulation start and end frequencies, the slack variables σ_1 and σ_2, the speed of sound a, a range of microphone numbers as well as defective or faulty microphones and the number of iterations. Previous SODIX calculations show that the most dominant sound sources are already modelled correctly after 20 iterations. The algorithm is able to improve the solution up to a tested 200 iterations [11].

Output

There are only two output parameters of the SODIX algorithm: The frequency range selected in the *sdx*-file in narrow band steps and the modelled CSM for the selected microphones for each narrow band. Both are saved to a *mat*-file and need to be processed before further information can be extracted. An object-oriented python plot routine for SODIX output was developed in the scope of this work, based on a MATLAB plot routine previously implemented by DLR.

The python routine is able to plot the SPL for selected SODIX result files. Each file contains an object that corresponds to all TOBs, which the data encompasses. Plots are carried out on the TOB level, i.e. each TOB is plotted individually and cannot be split into smaller spans. It is possible to plot a range of narrow bands if they are within a TOB and the input data does not contain more information. Figure 2.12 shows an example SODIX plot. The abscissa is length scaled with nozzle diameter and marks the position of the individual source points, the ordinate is the emission angle of each of those source points. This means, that the directivity of a source point can be read from a vertical line. The SPL of the directions is given by the color scale on the right side of the plot, which, unless specified otherwise, has a dynamic range of 20 dB. The nozzle exit plane is marked by a vertical dashed line, whereas the wing trailing edge and the flap tip are marked by dotted lines respectively.

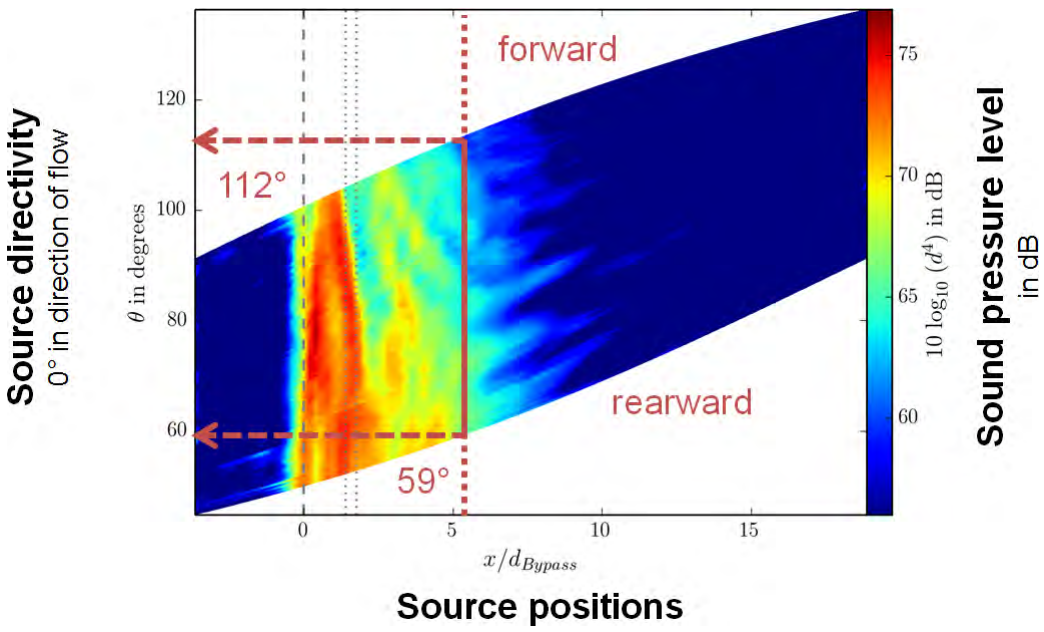

Figure 2.12: *Plot of an example SODIX calculation with explanatory markings.*

In addition, the routine is able to compare two different TOB objects, given that the microphone and source positions are identical. This restriction is required, as the routine bases the abscissa and ordinate on those positions. The differential plot routine works for individual TOB, but SODIX output files can be input as well; their TOB objects will then be used if applicable. Figure 2.13 depicts an example comparison plot with explanations for future reference. The color scale of the comparison plots uses a heat scale, with white being identical SPL between compared objects. The dynamic range is based on the greater of absolute maximum and minimum. The second TOB object is always subtracted from the first one, i.e. that if the plot shows mainly red colors, the first TOB radiates noise at a higher SPL. It has to be noted, that the comparison routine always displays the relative difference between two plot points, independent of their actual SPL. This entails that sometimes areas with a SPL that is comparably low to the main event get highlighted, because the relative difference is large at those points. This does not necessarily mean that those areas are relevant within the sound field.

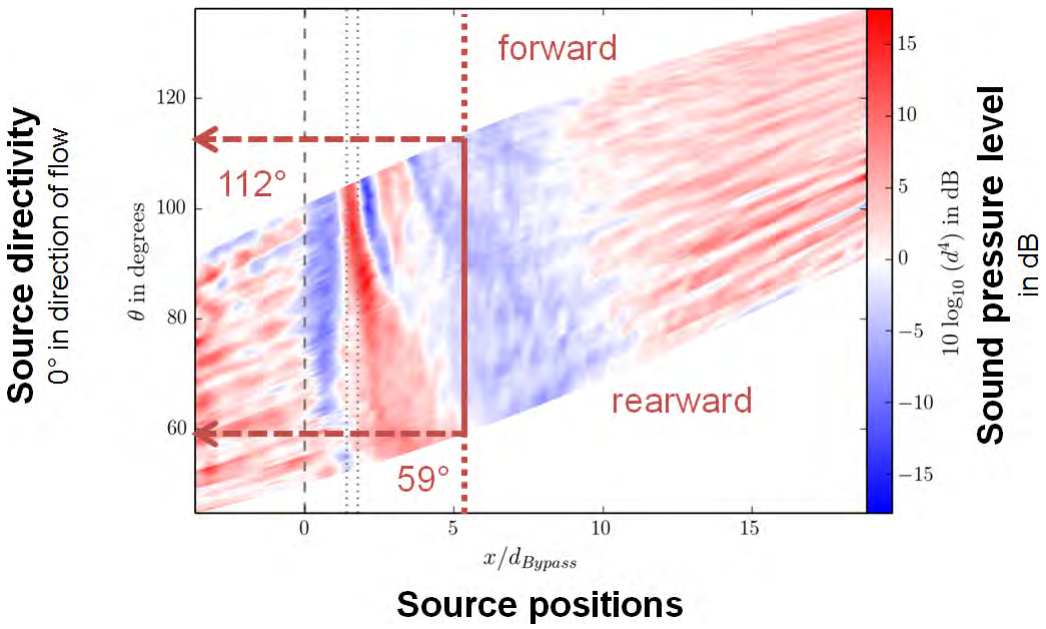

Figure 2.13: *Plot of an example SODIX comparison of two TOB with explanatory markings.*

3 Implementation

The experiment presented in this thesis was carried out between 20th June to 17th August 2012 at the noise test facility (NTF) of QinetiQ in Farnborough, UK as part of the OPENAIR European Research Project [32]. It was designed as a joint venture of multiple European companies that are leading in the field of aeroacoustical research. The research team was composed of scientists from DLR, RRUK, RRD, SN, Airbus and QQ [2]. The primary aim of the studies was to evaluate the influence of scarfed and serrated nozzle geometries regarding the rearward noise production of the aeroengine. Furthermore, the effect of a scaled wing model on the acoustics and fluid dynamics of the jet were being researched [2, 32]. The following chapter deals with the test preparation and setup (Sect. 3.1) and the experiments and their respective data sets (Sect. 3.2).

3.1 Experimental Setup and Execution

This section presents the test facility layout, the engine setup and the microphone arrangements used for the tests. It provides a brief description of those features in order to facilitate an easier understanding of the data evaluation in Chap. 4. Please refer to the individual test reports for further information on test conduction (see RR [2], DLR [32] and QQ [37]).

3.1.1 Coordinate System

The coordinate system used was cartesian, with the x-coordinate at a datum point centered on the engine axis halfway between the core and the bypass nozzle oriented in the direction of the mean flow. The y and z coordinates use the righthand system and point 270° and 180° from the top dead reference center, respectively. This coordinate system is used for all configurations. Figure 3.1 illustrates the coordinate system used. During the longcowl tests, the engine was moved so that

the coordinate center still falls on the datum point to avoid extensive repositioning of the microphones [32].

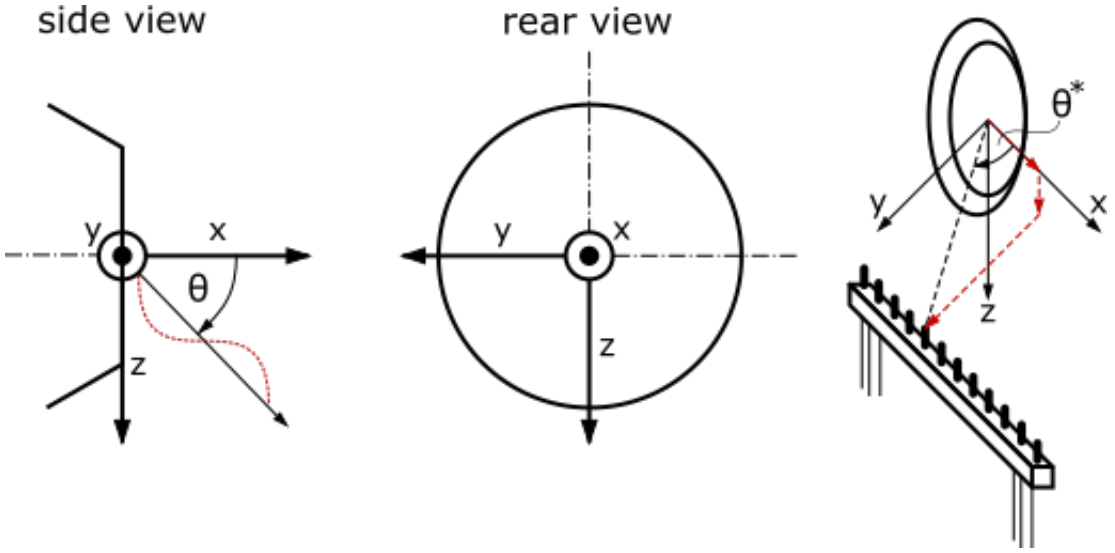

Figure 3.1: *Graphic illustration of the coordinate system used in the Openair experiment and this work.*

The emission angle θ^* illustrated in Fig. 3.1 is based on the emission angle θ from the source point to the respective microphone, corrected for the three-dimensional arrangement of the microphone array (see Sect. 3.1.5).

3.1.2 Testing Conditions

The tests were carried out under day ambient conditions, which inside the NTF could differ from the outside conditions. The ISA-referenced flow conditions were corrected according to the acoustic Mach number. Meticulous records for each individual test point can be found in the QQ test report. In order to evaluate the performance of the different nozzles and cowl configurations according to the ICAO noise certification standards, tests were carried out using different flow conditions emulating the behaviour of the engine during approach, cutback and sideline operations. In addition, a flight stream was simulated, in order to provide a realistic simulation of flow conditions during flight. The flight stream reached up to $70\,\mathrm{ms}^{-1}$ for approach and $90\,\mathrm{ms}^{-1}$ for sideline and cutback flight conditions. This test setup differs significantly from the usual setup for noise tests by aeroengine manufacturers, where flight stream simulation and wing interaction effects are not included [37].

3.1.3 Noise Test Facility

The QinetiQ NTF is an almost cubic, highly anechoic chamber, specifically designed for jet noise research (Fig. 3.2). The walls are 26x27 m long and 15 m high. The chamber is ventilated in order to prevent hot gas recirculation and to provide a steady air flow. The NTF can be used to test 1/10th scaled nozzles, which are mounted at a height of 8,73 m. The core and bypass air flows are provided by a centrifugal compressor at a maximum combined mass flow of $\dot{m}_{core,BP} = 15\,\mathrm{kg/s}$ at $p = 3\,\mathrm{bar}$. The NTF also allows the simulation of a flight stream up to $Ma = 0.33$. The flight stream is supplied by a very large blower and reaches a mass flow of up to $\dot{m}_{FS} = 350\,\mathrm{kg/s}$. The whole testing chamber is lined with 22,000 acoustic wedge liners, ensuring a most anechoic testing environment. In addition, an extensive silencing arrangement clads the air flow entry passages, thus warranting, that the noise produced by the flight stream is jet mixing noise only [37].

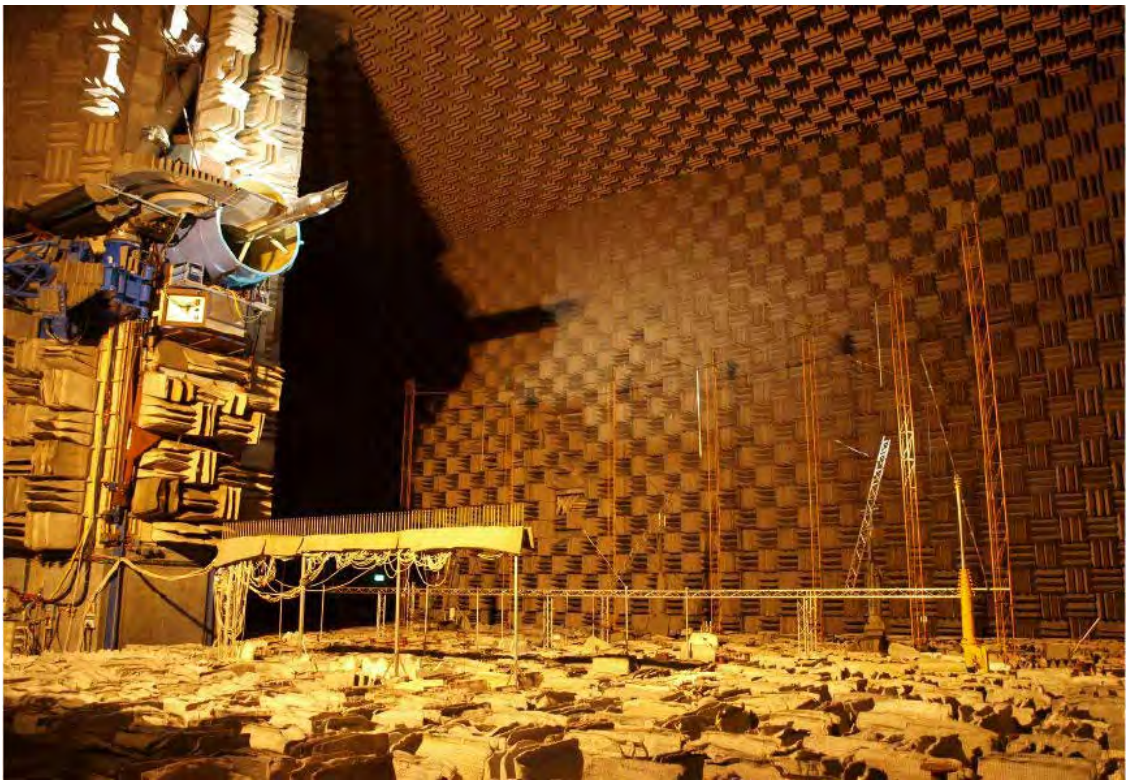

Figure 3.2: *An inside view of the QQ NTF in Farnborough, UK, showing the rig assembly, the linear microphone array and farfield arrays of joint researching teams [37].*

3.1.4 Engine Setup

This section deals with the configuration of the testing rig, comprising the model aeroengine with its different wing, cowling and nozzle configurations as well as the linear microphone array for sound directivity analysis. In addition, the excitation of broadband and tonal noise via external speakers is discussed. Though tonal noise generation was part of the tests, it is not subject of this thesis.

Nozzle and cowling

The nozzles were designed by RRD and SN. The short cowl (SC) configuration is based on a general outlet system with BPR 9. It was designed aerodynamically by RRUK and mechanically by SN. It was originally produced for the European SILENCE(R) project, the predecessor of the OPENAIR project (2001-2006) and was reused to minimize testing costs and provide the opportunity for data comparison with previous tests. The nozzle was designed for maximum noise reduction at approach, cutback and sideline conditions as well as for minimal aerodynamic losses during cruise. The long cowl (LC) configuration is based on an outlet system with BPR 5, originally designed by RRD and produced within the scope of an earlier project. A CAD draft of both configurations is shown in Fig. 3.3 [32, 37].

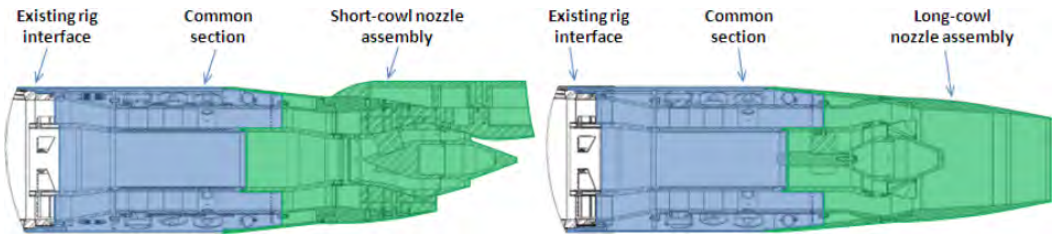

Figure 3.3: *Short cowl (left) and long cowl (right) engine configurations used during testing [37].*

The SC configuration was tested with three different nozzle geometries. The baseline configuration represents the standard design of the test aeroengine, whereas the scarfed and serrated nozzles were developed by Airbus France specifically for this test. The sinusoidal serrations were carved upstream into the nozzle such as to not move the bypass exit plane [37]. The LC engine was tested with baseline and scarfed nozzles only. Figure 3.4 shows the baseline and scarfed nozzle used throughout the test mounted on the LC configuration.

Figure 3.4: *Baseline and scarfed nozzle configurations used during testing on the long-cowl engine configuration. The forced mixer is visible inside the duct [37].*

Loudspeaker

The aeroengine used for the tests is a non-functional model that does not perform a thermodynamic cycle: The turbomachinery components compressor, combustion chamber and turbine are missing. The broadband and tonal rearward fan noise is instead simulated by a set of loudspeakers mounted inside the bypass duct. During the preceding TURNEX project, the speakers were mounted on top of tubes spanning the inner radial chord of the outer duct wall. However, since the OPENAIR test is carried out with added simulated core and bypass flow, this pratice had been no longer feasible, because the speaker tubes perturbed the flow. Hence multiple speaker arrangements were simulated by DLR in order to find a suitable setup. In compliance with the design goal, the final arrangement provides the smallest influence on broadband characteristics and coherence. The chosen configuration used 30 loudspeakers, arranged equidistantly over the engine's circumference on three axially staggered rings in groups of ten. The rings were staggered azimutally by one third of a speaker diameter. Figure 3.5 shows the speaker configuration [32].

The speakers were not able to radiate sound with a sufficient signal-to-noise ratio over the full frequency range at sideline and cutback conditions due to the high sound intensity of the jet. Therefore, five separate broadband scenarios were defined. The loudspeakers were operated with uncorrelated band-pass filtered white noise. The scenarios, labelled BB-A to BB-D, are listed in Table 3.1. For no-flow and approach conditions, broadband noise could be excited over the full frequency range of interest (BB).

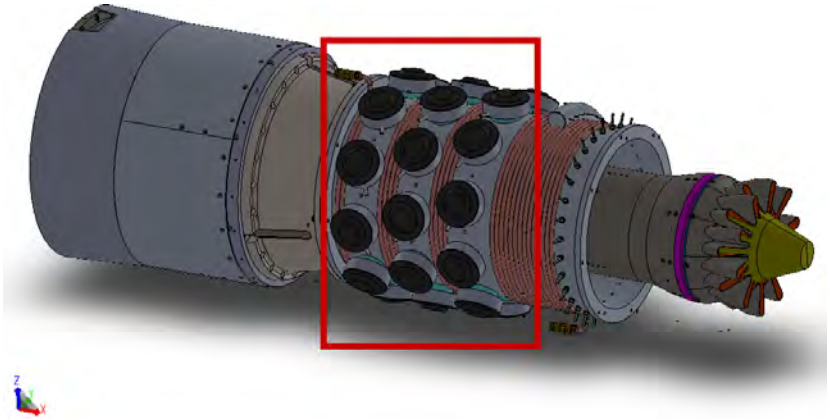

Figure 3.5: *Arrangement of the broadband/tonal loudspeakers on the engine model, marked by a red box. The model depicted is the core of the long cowl nozzle, showing the forced mixer [37].*

Table 3.1: *Broadband noise excited by operating the loudspeakers with uncorrelated band-pass filtered white noise.*

	f_{start} [Hz]	f_{end} [Hz]
BB	1200	20000
BB-A	1200	2500
BB-B	2500	5000
BB-C	5000	10000
BB-D	10000	20000

Wing

The wing model consists of a fully profiled starboard wing, a representative fuselage model and an aerodynamically faired wing stub to mount the model in the NTF. It had been designed and manufactured for the SYMPHONY program. During installed testing, the wing was mounted at 0° incidence relative to the direction of flow. The nozzle axis was aligned to the wing crack, see Fig. 3.6. The test report [37] states that flaps were always positioned at 16° during all tests, whereas the CAD draft of the test setup shows two flap positions, one at 16° and the other at approximately 32° relative to the flow axis. Standard Airbus 320 flap positions are 10° to 20° during take-off and 15° to 20° during approach. Full flap position is reached at 35° and is used during landing only [7].

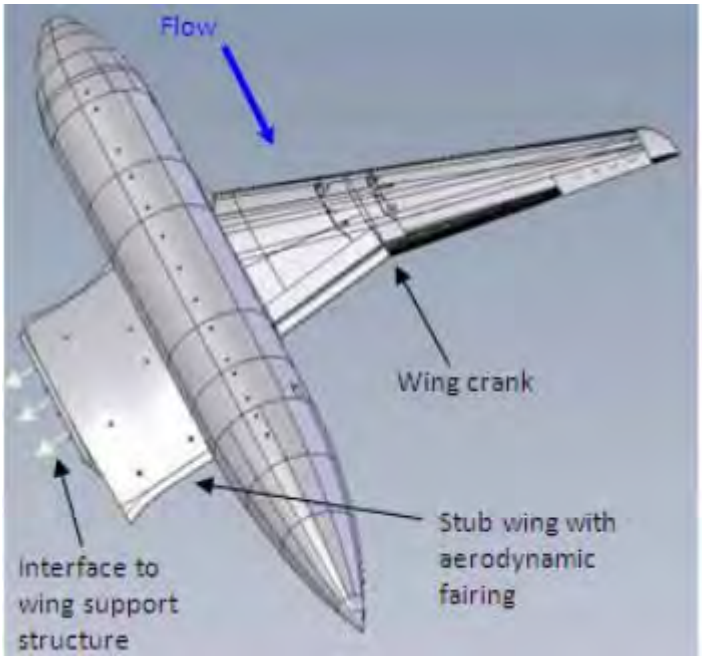

Figure 3.6: *The wing model, consisting of a profiled wing, fuselage and a stub mounting wing used during installed testing [37].*

3.1.5 Linear Microphone Array

The linear microphone array was part of the microphone arrangement of the test setup and was operated by DLR. It is placed in the nearfield of the engine and is specifically designed for 1D source location measurements. It consists of 100 microphones which are equidistantly spaced and mounted on top of a frame in parallel alignment to the jet axis. The frame is placed on top of stilts to minimize reflections caused by the acoustic wedges along the test chamber floor. Each microphone is mounted in a small brass tube to reduce the acoustic impact of the supporting structure. In addition, the frame is covered in acoustic foam absorbers. The linear array is shown in Fig. 3.7 and 3.2 [37].

The emission range θ of the microphones was corrected for the placement of the microphone array relative to the engine axis, see Fig. 3.1. In the subsequent SODIX plots, the corrected emission angle is displayed. Table 3.2 lists the geometric properties of the microphone frame. Table A.1 contains a detailed list of the cartesian coordinates and the emission angle of each microphone.

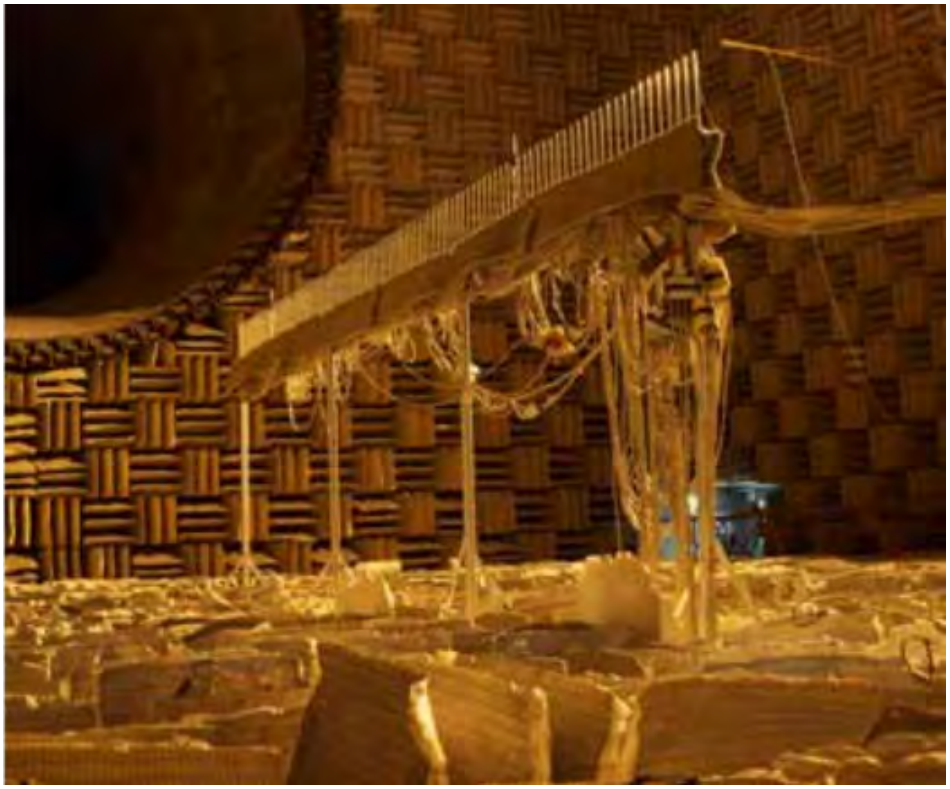

Figure 3.7: *Linear microphone array used by the DLR for source localization [37].*

Table 3.2: *Dimensions of the microphone array.*

Number of microphones	M	100
Microphone spacing	Δx_s	0.06 m
Array height	h_{Array}	5.71 m
Array offset	d_{Array}	1.01 m
Array length	l_{Array}	5.94 m
Emission range	θ	$109° - 33°$
Corr. emission range	θ^*	$101° - 50°$

3.2 Data Sets

This section deals with the data sets acquired during the tests. Testing environmental conditions are named and the data is analysed regarding its validity and practicability. In addition, an overview of the preliminary SODIX settings is given, paying special attention to the development of an optimised source position grid.

3.2.1 Raw Data

The raw data of the linear microphone array has been recorded by the DLR during the various tests. Each flow condition was sampled for 30 s at a rate of 44 kHz, using a 30 Hz highpass filter for each channel [37]. The linear array raw data consists of *hdf5*-files for each test point. The files need to be converted to *mat* format before source directivity calculation, because SODIX is coded in matlab. Each file contains the cross-spectral matrix (CSM) of its respective test point as well as the frequency spectrum in narrow band steps [22].

The test point (TP) naming convention is the following: Each test point is assigned a three letter code and number by QQ in alphanumerical order. In addition, each point is designated a different number by DLR. In the scope of this work the DLR denotation is used. In order to avoid confusion, DLR TP names are preceded by a "DLR" prefix (e.g. *DLR 317*). An exhaustive list of all TPs used in this thesis and their respective flow and working conditions can be found in Table A.3. Tests conducted with an installed wing will be referred to as "installed" cases below, whereas tests without wing installation will be referred to as "isolated" test cases. Furthermore, test cases with and without flight stream simulation are labelled with "FS" and "no FS" respectively.

Data verification

The results calculated by SODIX are depend on the quality of the raw data. Hence, it is advisable to perform a raw data check before the SODIX calculation. Figure 3.8 shows the logarithmic auto frequency spectrum of TP *DLR 317* for all microphones in the array as a function of their x position relating to the bypass nozzle diameter d_{Bypass}. The TP has been chosen representatively.

The microphone frequency spectra behave as expected, being of greater sound intensity with increasing distance from bypass nozzle. It is clearly noticeable that some microphones are miscalibrated and have lower a SPL than the neighbouring microphones, because their SPL shows a constant offset over all narrow bands. The x/d_{Bypass} position of these microphones is marked by black triangles in Fig. 3.8. This miscalibration may result from human error on the one hand, the calibration files containing the calibration constants show no anomalies for the deviating microphones, however. On the other hand, the microphones were exposed to demanding flow conditions and were thus of robust construction. Due

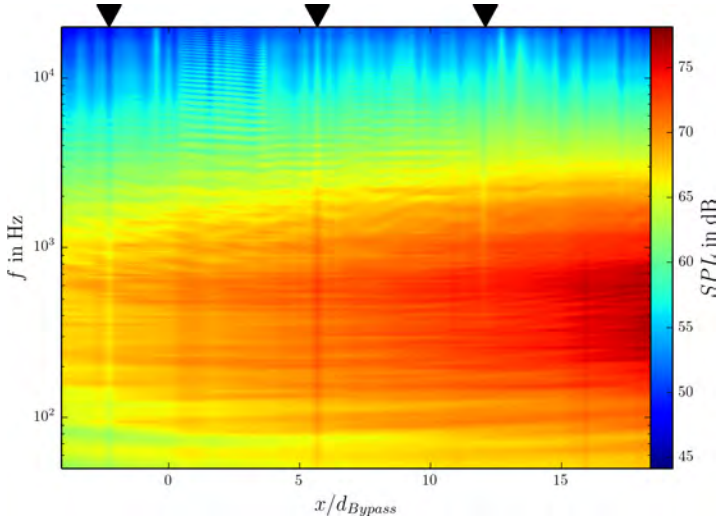

Figure 3.8: *Logarithmic auto spectrum, showing miscalibrated microphones marked by black triangles.*

to budget constraints, this aspect was deemed more important than the recording quality of the microphones. The resulting deviation of some devices to adjacent ones is less than one dezibel, and therefore of little impact for the SODIX calculation and can be further alleviated by modifying the value of σ_1 in the SODIX configuration file to smooth the directivity of each source, as explained in Chap. 2.3.4. It has to be noted, that the miscalibration may vary depending on the day the experiment was carried out, as the microphones were recalibrated multiple times during the testing progress, but with little variation over the weeks. Though SODIX offers the possibility to exclude miscalibrated or defective microphones from the calculation, this option was deliberately disregarded, because it interferes with the comparison plot routine as the number of defective microphones is not necessarily equal for different TPs.

Figure 3.9 shows the same auto spectrum as before, this time with frequency in linear scaling over relative microphone position, as this depiction emphasizes two other effect prevalent in the raw data. First, the individual microphones show a deviation in their frequency response for frequencies $f \gtrsim 5\,\text{kHz}$. As the microphones are correctly calibrated for low frequencies (see Fig. 3.8), the deviation at high levels most likely occurs due to the poor quality of the microphones. The variance compromises the quality of the SODIX plots and results in a frayed depiction of the source directivities. The display problems are of cosmetic nature, however, and have no influence on the physical validity of the results.

The distortion effect is illustrated by Fig. 3.10 for TP 317 at the 1000 Hz and

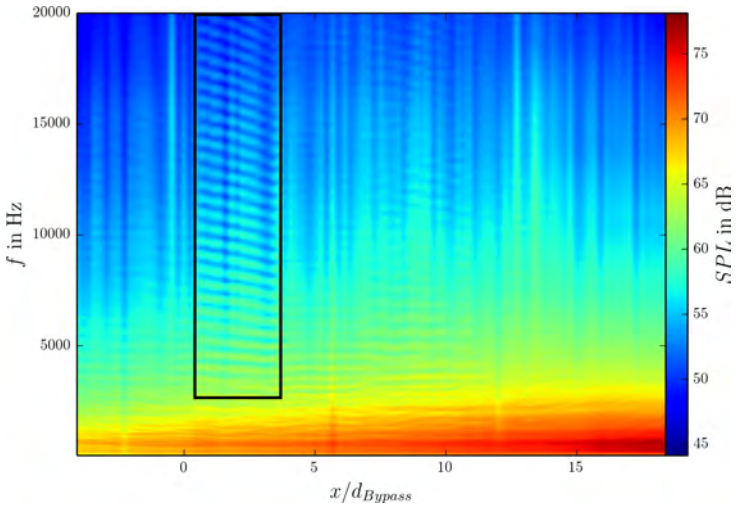

Figure 3.9: *Linear auto spectrum, showing frequency response variation on the one hand and an effect similar to a comb filter, marked by the black box, on the other.*

6300 Hz TOB. Whereas in Fig. 3.10(a) the source directivity is relatively smooth, the jagged edges and fluctuating distribution in Fig. 3.10(b) are the result of the poor raw data quality. This effect, though cleary visible, does not impair the plots to an extend that they are no longer reliable, because the underlying physical phenomenon of source directivity towards the microphones is unadulterated.

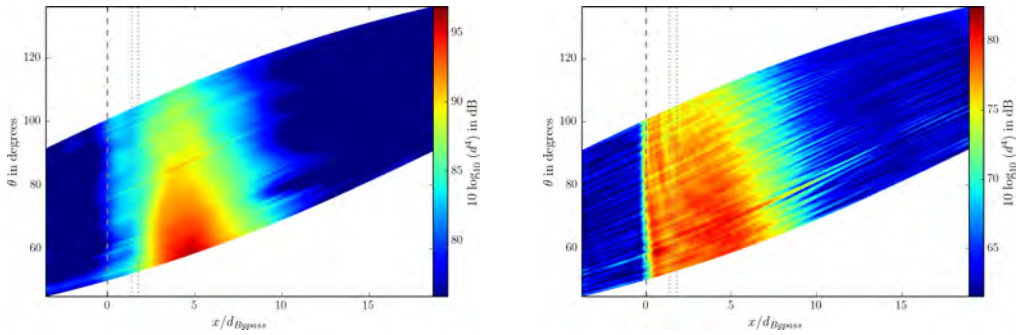

(a) TOB 1000 Hz (b) TOB 6300 Hz

Figure 3.10: *Comb filter effect evident in the source directivities of DLR 317 for TOB 6300* Hz*. TOB 1000* Hz *is free from this effect.*

The fluctuating distribution can be smoothed by increasing the value of σ_1 in the SODIX configuration file. However, this procedure might not always be feasible, since the frequency response deviation phenomenon occurs only for higher frequencies. The penalty function may then yield inappropriate results, because the wavelength is shorter than the distance between two adjacent microphones (as explained in Chap. 2.3.4). It was furthermore tested, whether a variation of the source grid density would smooth out the raw data ambiguity (see Chap. 3.2.2).

Various distances Δx_s, based on the wavelength of the respective TOB, have been tried out. The tests had no immediate effect on the resulting SODIX plot.

The second phenomenon, marked by a black box in Fig. 3.9, is similar to a comb filter effect. The periodic SPL fluctuation for frequencies $f \gtrsim 4000\,\text{Hz}$ for microphones in the first third of the array hints at wave interference in that segment. This occurs most likely due to sound wave reflection from the floor or the microphone frame, resulting in cancellation and amplification of the sound waves. According to the test reports, the whole test chamber as well as the frame were lined with sound absorbers in order to supress acoustic reflections. Analysis of the modulation frequency of the interference pattern yields a wavelength of $\lambda \approx 0{,}54\,\text{m}$, which suggests a reflection by the array frame, as the wavelength is equal to twice the distance from the microphone top ends to the bar they were mounted on and would therefore result in the observable sinusoidal amplification and cancelation. The comb filter effect in the raw data does not seem to have a noticeable impact on the result plots.

3.2.2 SODIX Setup

This section deals with the various preliminary steps required to configure SODIX for an optimal simulation run.

Source position distribution

Sect. 2.3.4 explained the necessity of having a suitable source position grid to allow the SODIX routine the localization of noise sources. The grid used originally (which will be referred to as the reference grid) is of equal length for each TOB ($l_s = 5\,\text{m}$) and uses a spacing of one fourth of the respective wavelength between source points for all TOBs ($\Delta x_s = 0.25\lambda$), see Fig. A.1. Therefore, the resulting grid has a very dense source point distribution for the highest frequencies. As SODIX calculates the directivity of each source point once per iteration step, the time needed for the calculation of the source directivity increases exponentially for higher frequencies as the number of source points increases inversely proportional to the wavelength. This section focusses on the attempts made to reduce SODIX computation time by adjusting the density and length of the source position grid, i.e. the number of points. Verification directivity calculations are conducted using the most tenuous assumable conditions within the

given data framework, i.e. sideline conditions with neither flight stream nor additional broadband or tonal sound excitation, as the velocity of the exiting jets is maximal there (TP *DLR 317*).

The SODIX calculation time can be estimated using a proprietary script that sums up the calculation time needed for each source point in every narrow band frequency within the simulation range. The time needed is based on Eq. 3.1, where the lower bound of summation f_l is the starting frequency, the upper bound f_u is the end frequency and $a(TOB(i))$ is the number of source points of the TOB for index frequency i. The frequency steps $\Delta i = 5{,}95\,\text{Hz}$ result from FFT analysis and correspond to the width of a narrow band in the scope of this experiment. It has to be noted that the calculation time is merely an estimation and may vary depending on the actual simulation.

$$t_{calc} = \sum_{i=f_l}^{f_u} t_{point} \cdot a(TOB(i)) \tag{3.1}$$

One approach to optimise computation time is to shorten the grid for higher frequencies. Michel and Siller [23] observed, based on studies by Viswanathan and Czech [35], that the maximal SPL can be found for $St = 0.5 \ldots 1$, with hot jets averaging at $St = 0.7$. A similar prediction was done by Zaporozhets et al [38]. and Bryce and Stevens [5], who located the SPL maximum at $St = 1.0$. According to Michel [23], the maximum moves upstream to the nozzle outlet towards higher frequencies and further downstream for lower frequencies. Generally, if the frequency is doubled, the distance of the SPL maximum from the nozzle is reduced by half and vice versa. For the test calculation, the SPL maximum was found to be at $x/d_{Bypass} = 5$ for $St \approx 1$ as expected. Based on these observations, multiple iterations of weighted grids were implemented in order to reduce the number of source positions for higher frequencies (e.g. Fig. A.3 and A.4). However, all weighted grids showed problems for higher frequencies, because aliasing effects occur downstream of the original sound source. Due to the shortened source grid length for high TOB, these effects were no longer correctly registered by SODIX, because the algorithm localizes the total sound energy from outside the computational domain at the borders of the source grid. The SPL of the appearing clusters can exceed that of the main sound source, resulting in distorted plots, see Fig. 3.11. There is an in-depth explanation of the aliasing effect in Sect. 4.1.

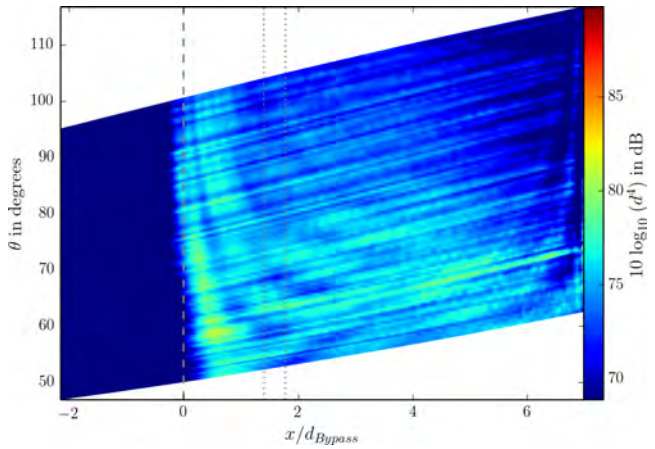

Figure 3.11: *Clustering of sound sources due to a shortened source position grid (type $L_{\alpha,2}$) for TOB 10000* Hz*, DLR 317. The highest SPL is approximately 90* dB *and barely visible at the far right side of the directivity matrix.*

Because shortening the source grid length is not feasible, several tests have been carried out using a different source point spacing, violating the maximum source offset criterion $\Delta x_s < 0.25\lambda \ldots 0.4\lambda$ (see Sect. 2.3.4). As expected, the subsequent plots differ significantly from the ones done with the reference grid, which is why this approach was deemed unfeasible as well. Further analysis revealed that there was an insufficient amount of source positions at low frequencies, unnecessarily diluting result plots, as SODIX cannot allocate the true sources unambigously (see Fig. 2.11). Tests revealed a beneficial influence when the source point density is increased at these frequencies.

The original intent of optimising the source positions in order to reduce computation time could not be achieved. At high frequencies, the aliasing effect prevents shortened grids. In fact, the final grid used in this work (Fig. 3.12) has more source points than the original reference grid. It is therefore optimised for this specific task and should not be generalized when dealing with other source directivity analyses. It uses a constant length $l = 5\,\text{m}$ and a source position spacing of $\Delta x_s = 0.25\lambda_{TOB}$, except below 500 Hz, where the source point distance remains constant.

Iteration steps

It is stated in the various publications concerning SODIX (see Sect. 2.3.4), that the algorithm is preferably to be run with 200 iteration steps. This number was therefore chosen for this work as well. However, time constraints created the

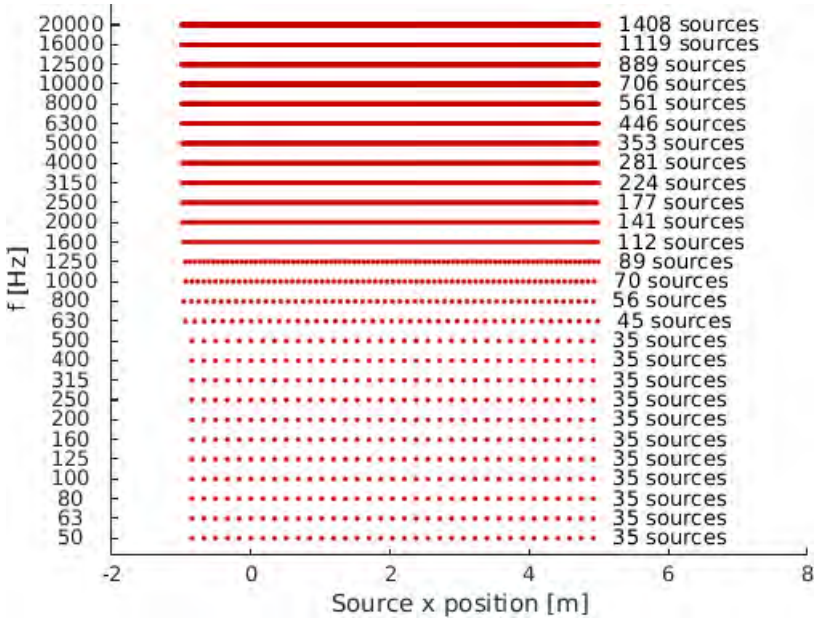

Figure 3.12: *Final source position grid used for the source directivity analysis in SODIX.*

need of running simulations with fewer iteration steps. Test runs with 50 and 100 iterations were carried out on the 3150 Hz TOB in order to verify that the results do not deviate significantly for a lower number of iterative steps. Figure 3.13 shows the comparison plots for both tests with the original case, respectively.

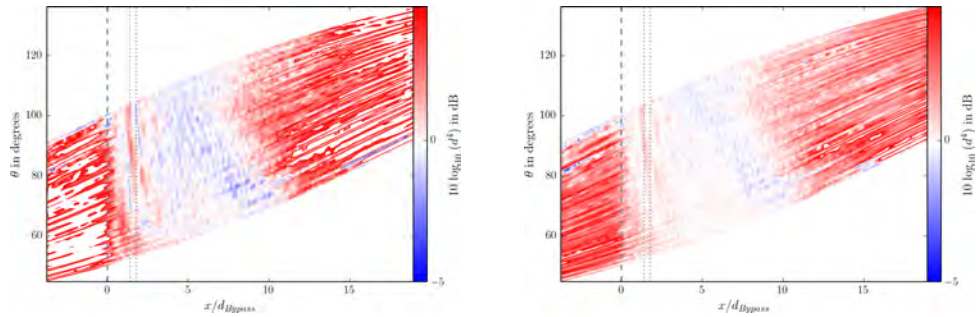

(a) 50 iteration steps.

(b) 100 iteration steps.

Figure 3.13: *Iteration count tests on DLR 325, TOB* 3150 Hz. *Dynamic range of the plot is* 5 dB. *Usual number of iteration steps is 200.*

Both plots look similar: The main sound source in the area downstream of the nozzle ($0 < x/d_{Bypass}$) is almost equal in sound intensity to the datum case, differing by up to 2 dB, whereas areas of lower sound pressure differ by a significantly larger margin. This commonly observable behaviour is due to SODIX' sound directivity analysis routine: The algorithm assumes a uniform sound field for every microphone and then elaborates the source directivity with each iterative step. Therefore, each additional step increases the dynamic range of the

resulting sound directivity. As the objective of this thesis is the evaluation of the main sound event, results with 100 iteration steps are acceptable, as their analyses entail an almost unchanged sound field and can thus be conducted without compromising the result. The deviation is larger for 50 iteration steps, which should therefore be used more carefully. All TPs analysed with SODIX in the scope of this thesis have their number of iteration steps listed in Table A.3.

Slack variables

Preparing the analysis, several SODIX runs have been conducted for one TOB of a single TP, altering the slack variable σ_1 between each run in order to determine an optimal value for σ_1 for all future runs. Four values have been selected: $\sigma_1 = \{0, 0.001, 0.01, 0.1\}$, where $\sigma_1 = 0$ represents a disabled smoothing function $G_1(d)$. The results are displayed in Fig. 3.14. As expected, the source directivity becomes smoother for increasing values of σ_1 (see Sect. 2.3.4). However, due to the interpolation between neighbouring sources, the detected maximum SPL decreases. Peculiarly, the SPL maximum does not decrease strictly monotonic for increasing σ_1, but is nearly equal to no smoothing for $\sigma_1 = 0.01$. If the slack variable becomes too large ($\sigma_1 > 0.01$), the dynamic range of the output is reduced considerably. $\sigma_1 = 0.001$ represents a good compromise of source directivity smoothing without reducing the readability of the output data, while simultaneously filtering out frequency response deviations. However, generalizing conclusions for all TOB and experiment setups cannot be drawn. Therefore, the σ_1-smoothing function will be turned off ($\sigma_1 \equiv 0$); should need arise, calculations of specific TOB will be rerun with $\sigma_1 = 0.001$.

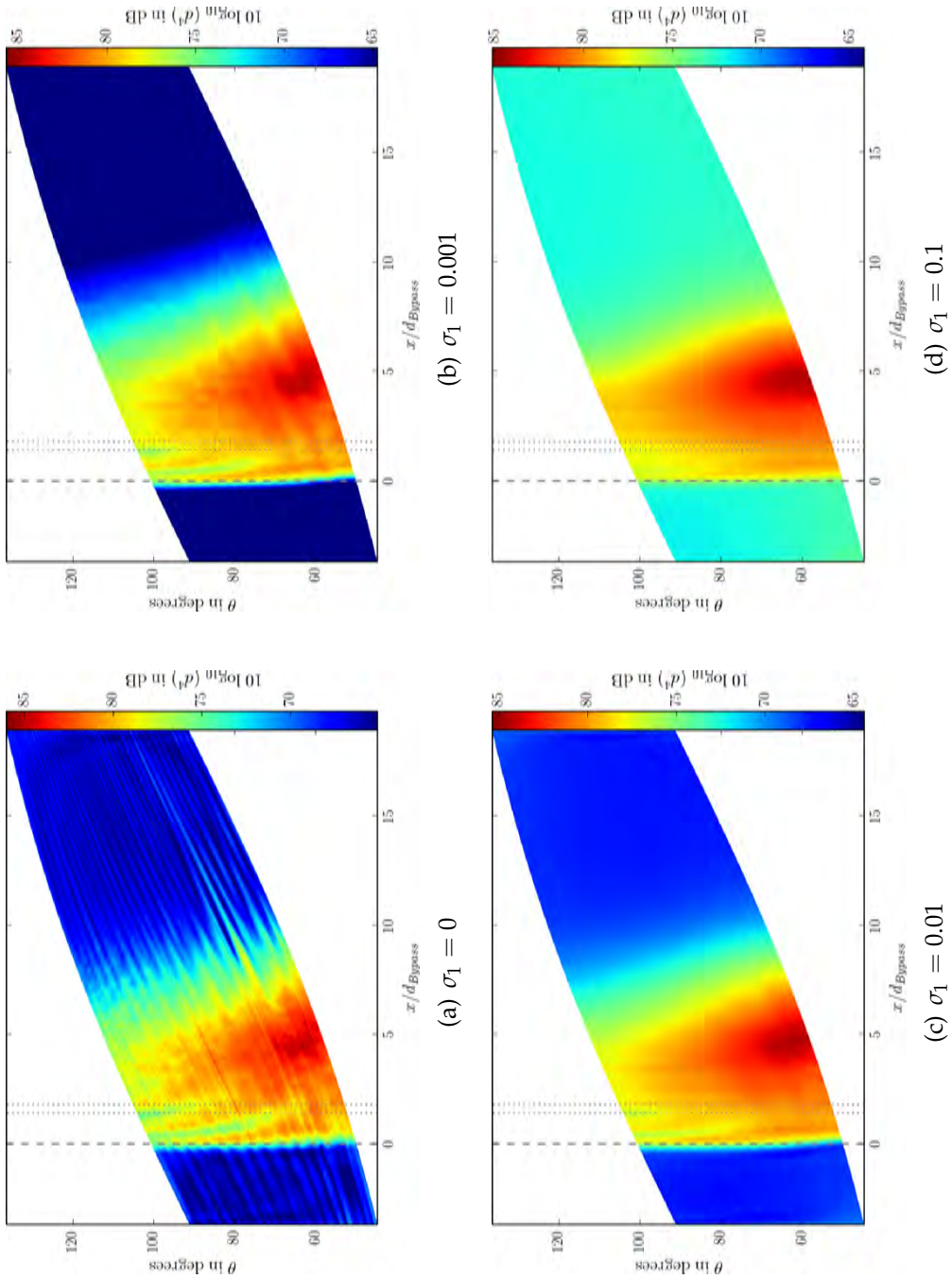

(a) $\sigma_1 = 0$ (b) $\sigma_1 = 0.001$

(c) $\sigma_1 = 0.01$ (d) $\sigma_1 = 0.1$

Figure 3.14: *Source directivity plots of DLR 317, TOB 4000* kHz*, different values of* σ_1.

4 Data Analysis

This chapter discusses the results of the conducted SODIX simulation runs. First, the aliasing effect introduced in Sect. 3.2.2, that is present at high frequencies is analysed and possible reasons for its occurence are presented. Second, the effects of flight stream presence on the overall flow conditions are elaborated. In the following sections, the various build configurations are presented in order:

- ICAO noise certification flight conditions with and without a simulated flight stream,
- test runs with simulated rearward fan broadband noise,
- baseline, scarfed and serrated nozzle configurations and
- short- and long-cowl engine configurations.

The focus lies on the comparison of uninstalled and installed jet noise. The test cases without flight stream will only be analysed when comparing the ICAO reference measurement simulation points (Sect. 4.3). After this, these cases will be excluded from future analysis, as their sound field does not represent common flight situations.

4.1 Aliasing

Investigation of high TOB SODIX plots yields an unforeseen problem, independent of the source allocation used. Using the OPENAIR raw data, SODIX is not able to determine the source position of the recorded cross-spectral sound intensity unambiguously for frequencies $f \gtrsim 8000\,\mathrm{Hz}$. Instead, a secondary emission area is located at the rear end of the source positions, as evidenced by Fig. 4.1(a) for TP *DLR 317*. This effect occurs first at the distant site of the source directivity matrix and moves closer to the nozzle for increasing frequencies, showing harmonic qualities for higher TOB (see Fig. 4.1(b)).

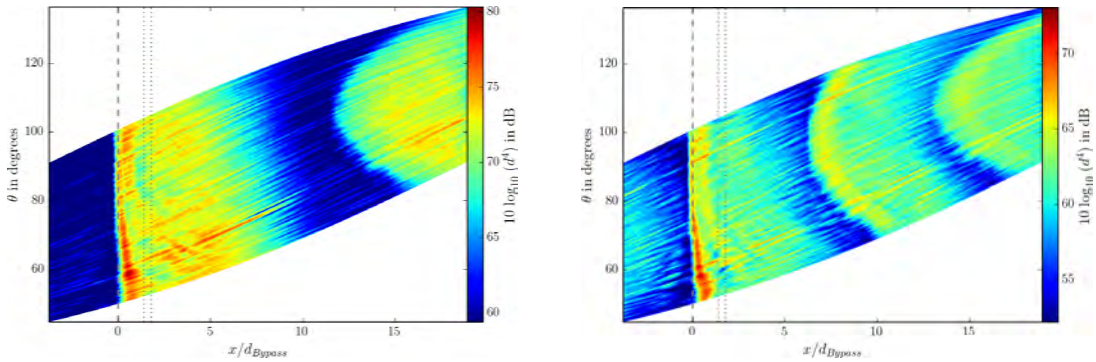

(a) TOB *10000* Hz. (b) TOB *20000* Hz.

Figure 4.1: *Harmonic aliasing effect evident in SODIX plots of TP DLR 317.*

The effect seen in Fig. 4.1(a) and 4.1(b) respectively, distorts the SODIX results to a certain degree as the SPL values drop significantly in the primary wake area of the nozzles. It is questionable, whether this effect represents physical phenomena or is an error either in the raw data itself or on SODIX' side. At first glance, it suggests some form of spatial aliasing, as it appears to have harmonic qualities and only occurs for high frequencies, when the wavelength is short. Spatial aliasing effects are prone to occur due to spatial undersampling of the sound events. The microphones in the linear array are spaced at constant intervals, which could potentially be too wide for high TOB, as the length of the sound waves decreases with increasing frequency. A possible criterion to assess this phenomenon is the trace wave length λ_s (Eq. 4.1) [25]. The trace wave length is the hypotenuse of the triangle formed by the line connecting the source (e.g. at the nozzle exit) with microphone and the axis of the microphone array, see Fig. 4.2.

$$\lambda_s = f(\lambda, \theta^*) = f(c, f, \theta^*) = \frac{\lambda}{\cos(\theta^*)} \tag{4.1}$$

Based on experience, aliasing effects tend to occur, when $\lambda_s < 2\Delta x_m$. Analysis of various high frequency plots showed, that aliasing generally occurs starting with the 8000 Hz TOB. A verification simulation run, that is independent of the OPENAIR data, has been conducted using a constructed CSM that only contains one sound source at the nozzle outlet ($x = 0$) at 20 kHz. It uses a single steering vector g_{jm} with the same microphone and source positions as the OPENAIR tests (see Eq. 2.13). The plot of the verification run can be seen in Fig. 4.3(a). There is a clear shape similitude in source directivity between the calculated and simulated CSM. The aliasing event SPL is approximately 40 dB below the main source.

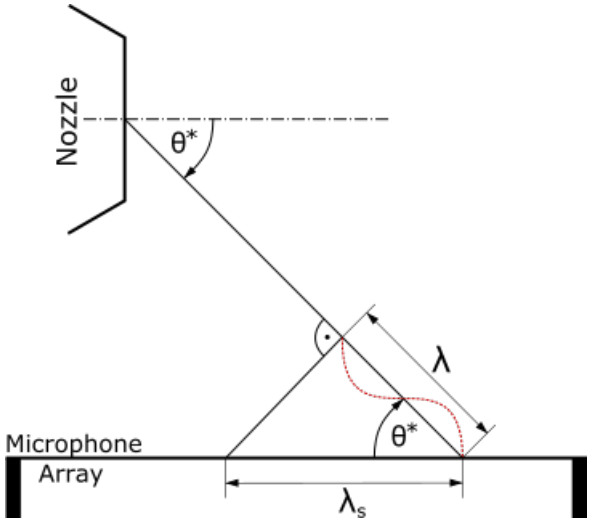

Figure 4.2: *Graphic illustration of the trace wave length λ_s.*

However, the constructed verification CSM facilitated an acceptable SODIX result, as the simulated source radiates exactly at a source position specified in the grid. When the source is spread out over five positions that do not coincide with the assumed source positions, the resulting plot changes and resembles the actual aliasing effect more closely, see Fig. 4.3(b). Here, the SPL of the aliasing event is only $\approx$ 20 dB below the main event, which is similar to the experiment. In conclusion, the constructed CSM proves that aliasing occurs due to spatial undersampling. As stated in Eq. 4.1, λ_s is a function of wavelength and corrected emission angle, both of which are fixed due to testing contraints. Thus, the only possible solution to avoid spatial aliasing effects during future tests would be to reduce the spacing interval Δx_m of the microphones in the array, though this may not be always technically or economically feasible.

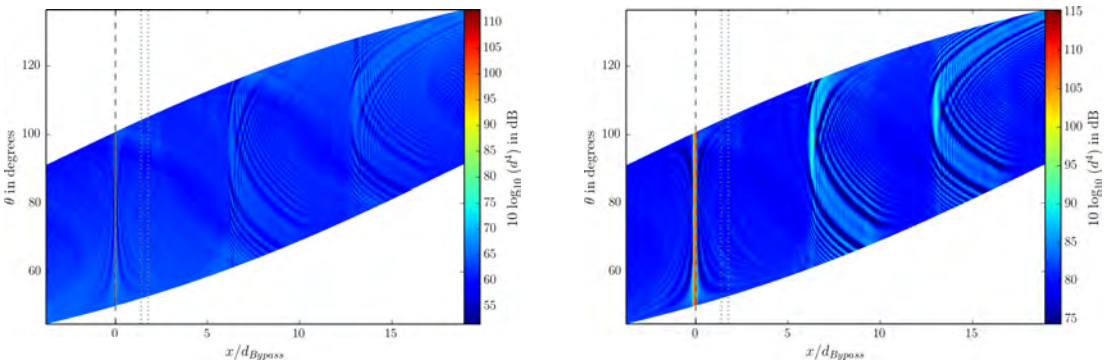

(a) Single source CSM. DR is 60 dB.

(b) Multiple source CSM. DR is 40 dB.

Figure 4.3: *Harmonic aliasing effect evident in SODIX plots of specifically constructed CSMs that evidence the existence of aliasing effects due to insufficient microphone spacing, TOB 20000* Hz.

4.2 Flight Stream Effect

This Section presents tests where only the flight stream was present. Though two simulations have been run at 70 ms^{-1} (*DLR 247*) and 90 ms^{-1} (*DLR 248*) FS velocities, representing approach and cutback/sideline conditions respectively, only plots of the latter will be shown here, as the sound fields do not differ substantially, with *DLR 248* averaging at an 8 dB higher SPL maximum than *DLR 247* over all analysed frequencies. Figure 4.4 shows a low- and high-frequency TOB plot of *DLR 248*.

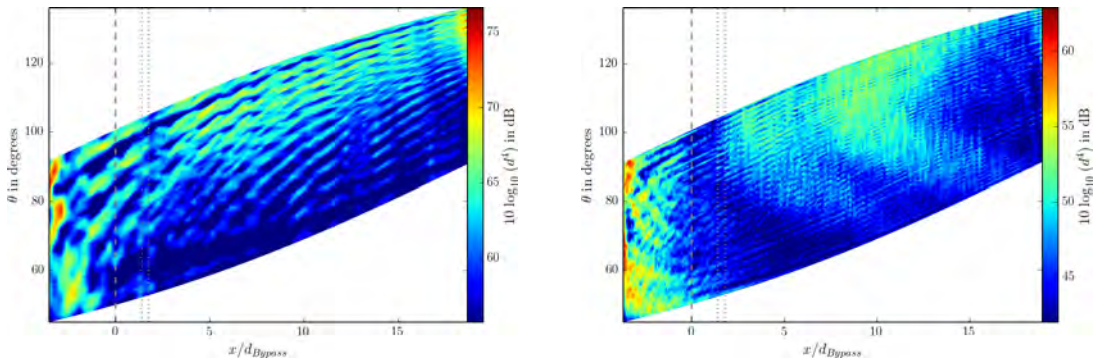

(a) TOB 1000 Hz (b) TOB 4000 Hz

Figure 4.4: *SODIX plots of a testpoint with flight stream simulation only (DLR 248), using the developed source position grid (Fig. 3.12).*

The main source event is localized by SODIX at the leftmost grid position. Judging by the symmetric moiré-like patterns occuring over all frequencies, SODIX seems unable to detect true sources within the given source position grid. As the algorithm needs to distribute sound energy to specific sources, it tries to place those at the most likely positions in the provided field. The flight stream noise does not perturbate into the measurement area, otherwise the entire plot would be of the same intensity. It is likely that the flight stream noise is caused by turbulent flows due to potential core collapsing or by surface interaction along the test rig. According to the QQ test report, the extra large fan supplying the flight stream air should not be the source of this sound, as it is intergrated into an extensive silencing arrangement [37]. Figure 4.5 shows the spectrum plots of *DLR 248* (sideline FS), *DLR 317* (jet sideline without FS) and *DLR 325* (jet sideline with FS), see also Sect. 4.3.1 and 4.3.2.

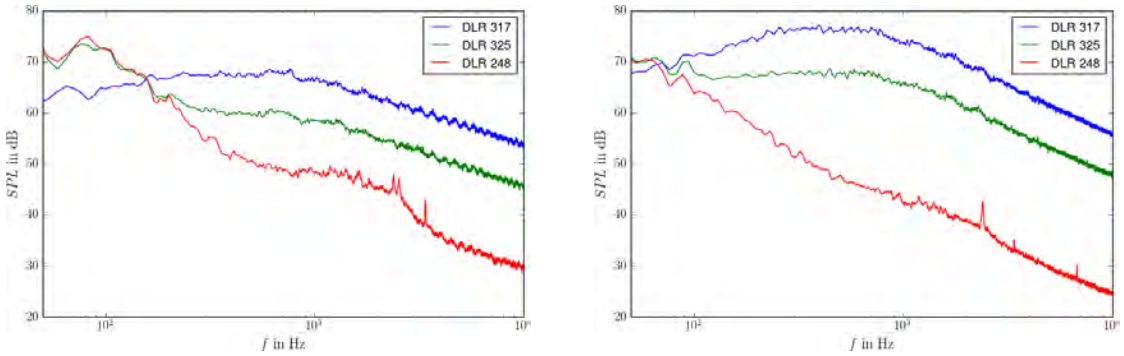

(a) First microphone in linear array (b) Last microphone in linear array

Figure 4.5: *Frequency spectra of DLR 248 (FS only), DLR 317 (jet only) and DLR 325 (jet with flight stream).*

The spectra clearly show that the flight stream dominates the sound field at very low frequencies. Above a threshold of approximately 200 Hz, the sound intensity of the flight stream test run drops significantly, especially for the first microphones in the array and in comparison to the tests with core jet enabled. The low frequency source plot (Fig. 4.4(a)) shows patterns that persist over all frequencies. At higher frequencies, additional aliasing occurs, as described in Sect. 4.1, though here the first occurence is visible for 4000 Hz (Fig. 4.4(b)). The linear and logarithmic auto spectra plots of *DLR 248* displayed in Fig. 4.6 do not show any of the anomalies discussed in Sect. 3.2.1, except a few miscalibrated or defective microphones, further evidencing that the aliasing effect is not caused by raw data ambiguity, but by the SODIX algorithm.

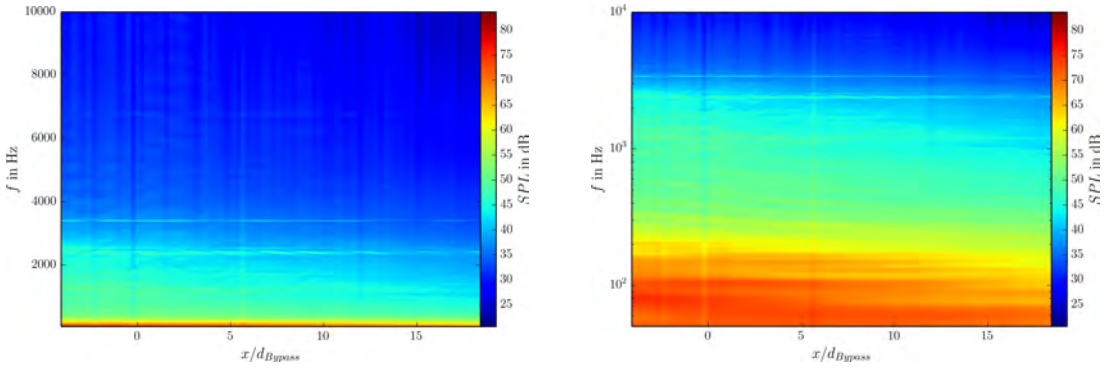

(a) Linear frequency scale (b) Logarithmic frequency scale

Figure 4.6: *Linear and logarithmic auto spectra of DLR 248.*

In order to properly assess the flight stream sound field, the SODIX calculations of *DLR 248* were rerun using a source grid that extends 10 m upstream of the nozzle. The result plots can be seen in Fig. 4.7.

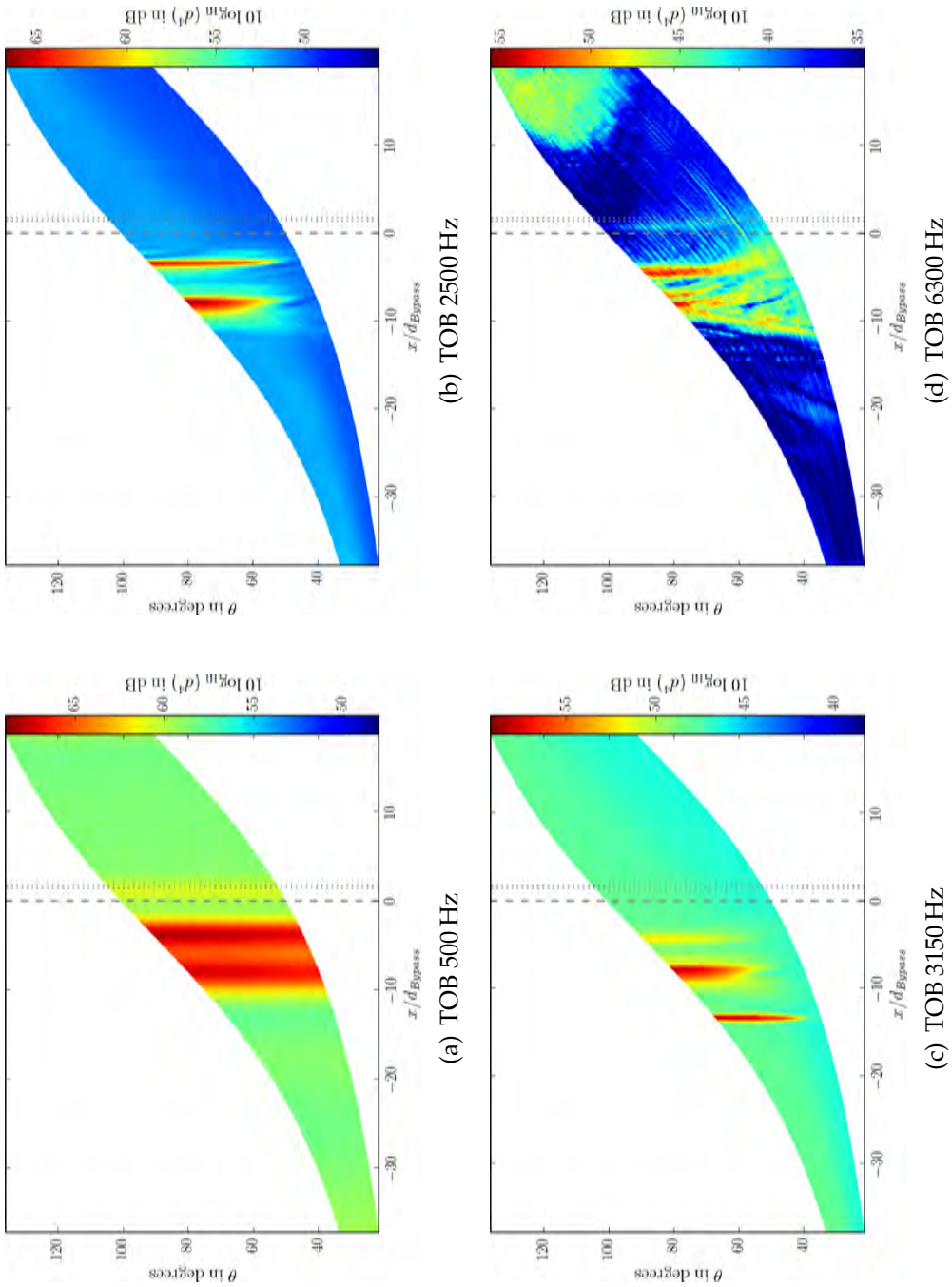

(a) TOB 500 Hz (b) TOB 2500 Hz (c) TOB 3150 Hz (d) TOB 6300 Hz

Figure 4.7: *SODIX plots of a testpoint with flight stream simulation only (DLR 248), using a grid that extends* 10 m *upstream of the nozzle.*

The results show very clear sound events for all TOBs except the highest, where the aliasing effect visibly distorts the plot characteristics. For this calculation, σ_1 was set to 0.001. The plots show three clear sound events that vary over the frequency. For low frequencies up to 2000 Hz, a single event, possibly due to jet mixing noise at or behind the flight stream nozzle, is detected at $x/d_{Bypass} \approx -10$. For very low frequencies, this event possesses uniform directivity, whereas at higher frequencies the event is picked up only by the first half of the microphone array. This phenomenon, as well as the SPL of the different plots, coincide very well with the observations made for Fig. 4.5.

For $f \gtrapprox 2500$ Hz TOB, a second sound event occurs at $x/d_{Bypass} \approx -4$, which is most likely linked to flight stream jet mixing noise due to potential core collapsing. This event is not picked up by the rear quarter of the microphone array, possibly because of a combination of atmospheric attenuation and σ_1 usage. At the 3150 Hz TOB, a third sound event occurs upstream of the other two. As it is detected at this TOB only, it likely stems from a tonal noise source, e.g. an obstacle shedding vortices at a set frequency. The plots in Fig 4.7 show, that the flight stream produces clear sound events upstream of the nozzle that are outside the source position grid used otherwise. The FS dominates the sound fields at very low frequencies outside of the analysis scope of this thesis.

4.3 ICAO Reference Measurement Points

This section deals with the test points that simulate the ICAO noise certification reference points, namely sideline (SL), cutback (CB) and approach (APP). The relevant TPs are listed in Table 4.1. The tests were all carried out on a short-cowl engine with baseline nozzle configuration without any additional sound excitation.

4.3.1 Reference Measurement Points without Flight Stream

The following subsection first presents the analysis of the uninstalled and installed sideline measurement points in greater detail. For the remaining CB and APP TPs, only the most interesting events will be shown.

Table 4.1: *Test points simulating ICAO reference measurement. All tests were carried out on a baseline short-cowl engine without additional sound excitation.*

DLR TP	Condition	Flight Stream	Wing
317	SL	No	No
435	SL	No	Yes
279	CB	No	No
411	CB	No	Yes
287	APP	No	No
395	APP	No	Yes
325	SL	Yes	No
443	SL	Yes	Yes
257	CB	Yes	No
423	CB	Yes	Yes
297	APP	Yes	No
403	APP	Yes	Yes

Sideline ICAO reference point without wing installation

The SODIX plots of TP *DLR 317* are shown in Fig. 4.8 for four different TOB, giving an overview of the SPL and source directivity trends with increasing frequency.

For the 250 Hz TOB, the maximum SPL is approximately 94 dB and is located at $x/d \approx 7$, where the main low-frequency mixing takes place. The radiation shows a clear rearward component. The plot suggests that the true sound maximum of the jet radiates even further downstream and is subsequently outside of the angular range. This observation carries through most of the analysed tests. For future tests it is therefore suggested to extend the linear microphone array further downstream in order to pick up signals at lower emission angles ($\theta = 30° \ldots 50°$).

As expected, the SPL maximum moves upstream with increasing frequency. At a frequency of 1250 Hz, the absolute SPL maximum is reached, which equals $St = 1$ at $x/d = 5$. This behaviour is consistent with the theory presented in Sect. 2.3.3. As the frequency increases further, the SPL maximum of each TOB decreases and moves closer to the nozzle outlet plane. This connection can be ascribed to the fact, that high frequency noise is caused by small eddies, which mainly occur in the primary mixing zone of the jet. With increasing jet length, the eddies widen, causing the frequency of their generated noise to become lower.

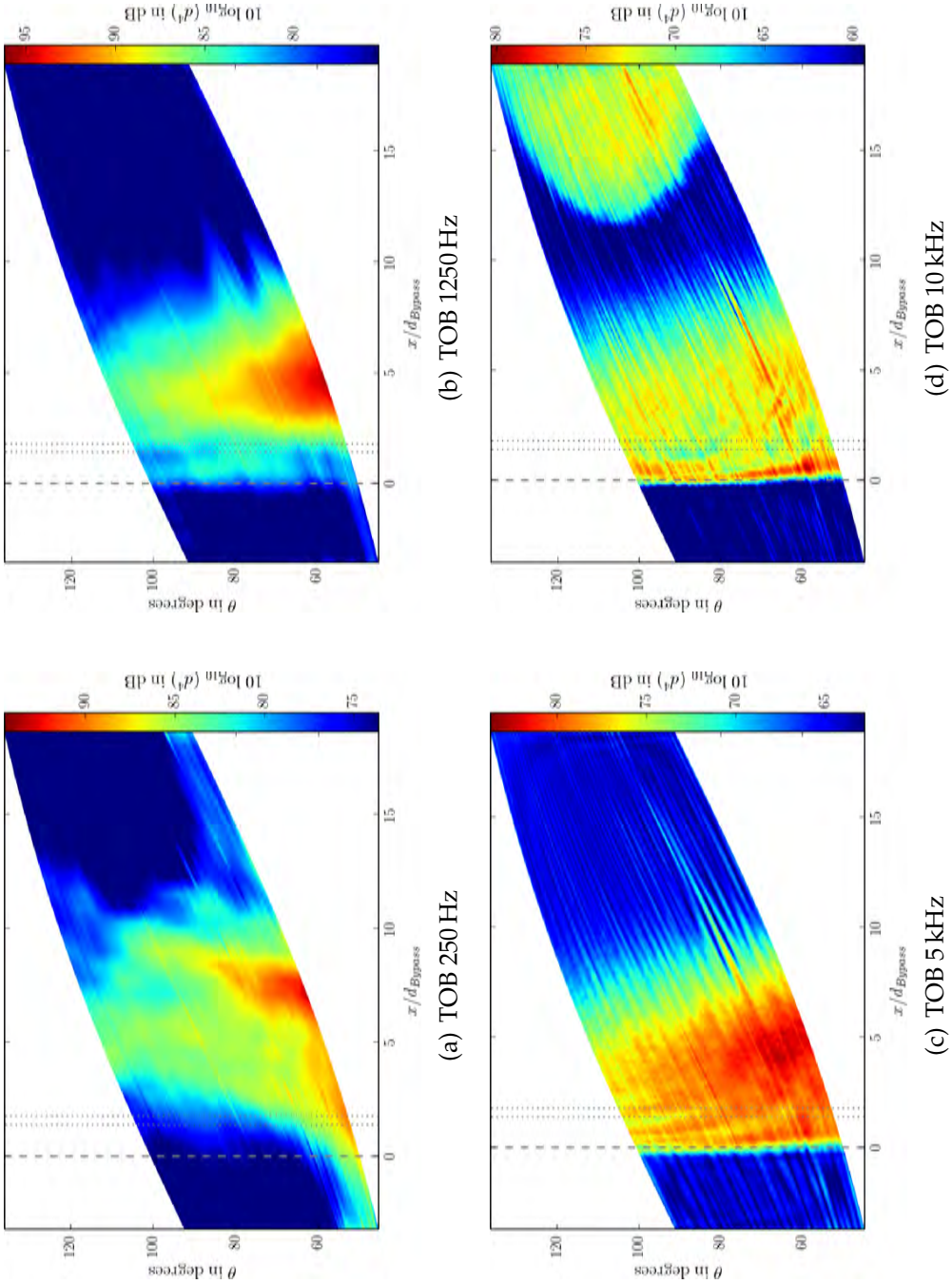

(a) TOB 250 Hz (b) TOB 1250 Hz

(c) TOB 5 kHz (d) TOB 10 kHz

Figure 4.8: *Source directivity plots of different TOBs of DLR 317 (baseline nozzle at sideline conditions without wing installation and flight stream).*

At 5 kHz, three distinct sound sources can be observed radiating into the forward arc, whereas SODIX locates the sources more uniformly for the downstream microphones. This implies some form of wave interference in the forward quadrant which results in the trident shape. Beginning with the 5 kHz plot, the frequency response deviation of the microphones described in Sect. 3.2.1 can be seen. At 10 kHz, aliasing occurs, causing SODIX to falsely take away source energy from the main source and add it to the aliasing sources. In addition, the last two plots show clearly, that the source events start almost exactly at the nozzle outlet $x = 0$, as there is no source detected upstream of this plane. This implies that there are no significant noise sources on the aeroengine nacelle, but only in the free jet, which is to be expected without employing a simulated flight stream.

Sideline ICAO reference point with wing installation

Figure 4.9 shows the comparisons of installed (*DLR 435*) and isolated (*DLR 317*) jet. The uninstalled wing case is always subtracted from the installed case, so that positive values, represented in red, imply that the installed case is louder.

The SPL difference between installed and isolated test configurations is generally about 12 dB, which is a rather significant increase. The aliasing effect becomes more prominent as well. In the low-frequency domain, additional sound sources occur primarily upstream of the nozzle and can most certainly be attributed to either sound wave reflection from the wing or surface/flow interactions. However, as incidence and exit angles must correspond, the forward reflection would require an unusual negative incidence angle. Therefore, the physical validity of the 250 Hz plot is questionable.

The high-frequency plots exhibit more expected behaviour. For the 1250 Hz TOB, there are two different areas with increased sound pressure, the first right at the nozzle radiating into the aft quadrant, the second in close proximity to the nozzle being picked up by almost the full linear array. At this frequency, the sources are most likely medium-scale eddies formed on the underside of the wing due to wall shear stress. These vortices only occur within a small frequency range; for higher frequencies the sources become more well-defined. On the latter two plots, there are two distinct noise sources. The first is on the same position as the one in the 1250 Hz plot, meaning that there is a turbulent event emitting a broadband noise that spans over all TOB. The second source travels further downstream with increasing frequency. As eddies tend to grow with increasing travel distance, the

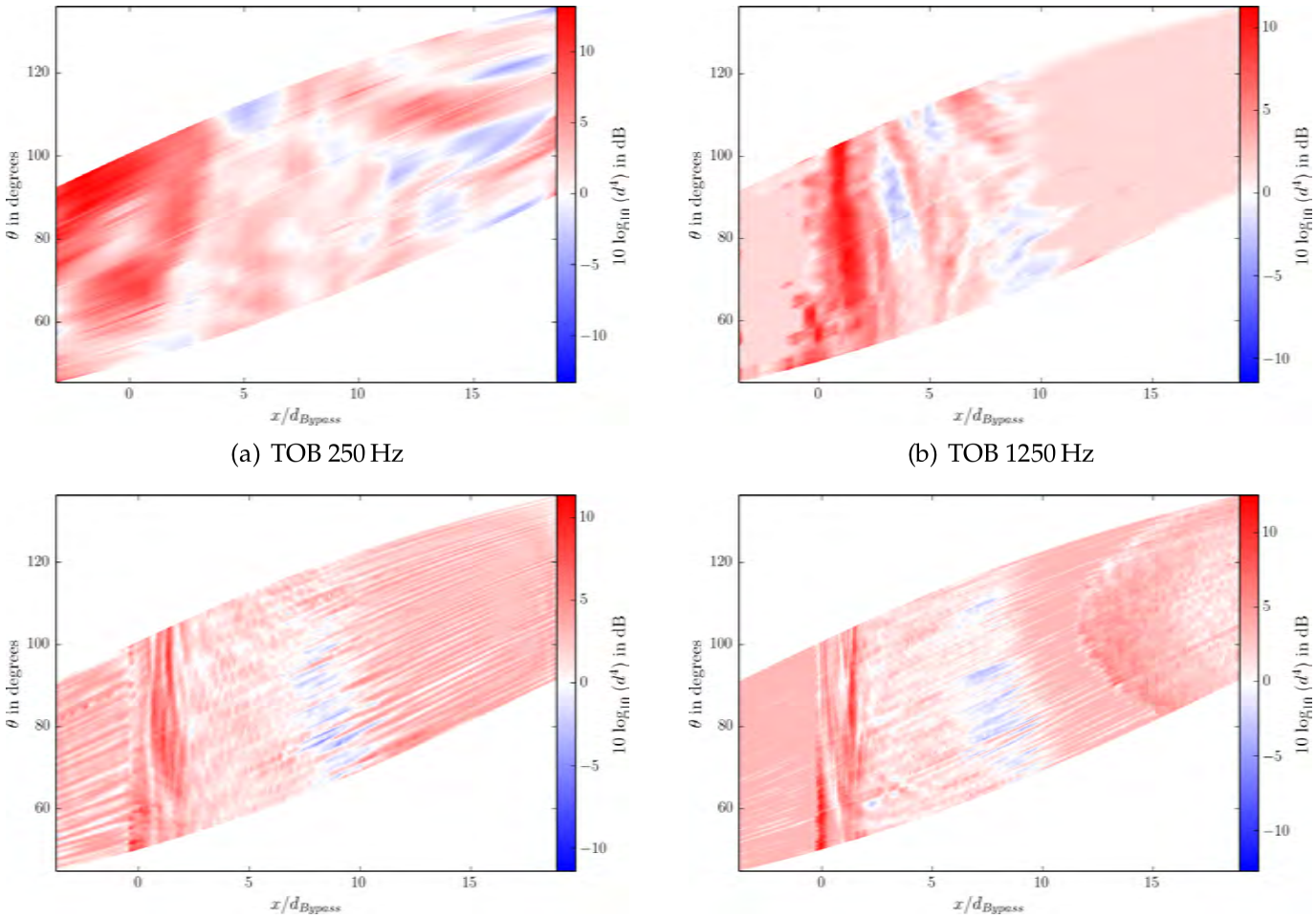

(a) TOB 250 Hz

(b) TOB 1250 Hz

(c) TOB 5 kHz

(d) TOB 10 kHz

Figure 4.9: *Source directivity comparison plots of different TOBs of DLR 435 and DLR 317 (baseline nozzle at sideline conditions with and without wing installation).*

second sound source at high TOBs is most likely different from the first source. As such, it can possibly be linked to vortices separating at the position where the deployed flap system impinges on the free jet.

The sound field intensity with installed wing is not greater at every source position, however. In the 1250 Hz plot, there is an area, where the uninstalled SPL is above the installed level at $x/d \approx 4$. As it is far downstream of the engine/wing installation, one possible explanation is, that the noise reduction has to occur due to reduced turbulence in the mixing jet. The following subsection revisits this phenomenon, as it also appears for APP and CB conditions.

Approach and cutback ICAO reference points with wing installation

For the approach and cutback TPs, only the core and bypass jet velocities change in comparison to the sideline TPs explained above. Therefore, this subsection will only focus on the noticable differences between the flight conditions. Figure 4.10 shows the comparison plots of selected approach and cutback TOBs.

The wing installation increases the SPL relatively uniformly over the entire measurement area for all TPs, similarly to the sideline TP shown before. The SPL difference is significant and averages at $+20$ dB for the installed case. The low-frequency plots in Fig 4.10 (800 Hz and 1000 Hz) show a signficantly louder sound source upstream of the nozzle at $x/d < 0$. The individual plots for both TPs reveal that the source upstream of the nozzle is much weaker than the main jet source and the difference plot suggests more significance than there actually is. Moreover, both low-frequency plots show an area where the installed case is of lesser relative intensity at $x/d \approx 3-5$. When analysing the non-comparison plots for installed and uninstalled approach conditions (Figure 4.11) it becomes evident that both cases exhibit a source gap at this position. This gap moves downstream when the wing is installed, which results in the SPL difference observable in Fig. 4.10(a) and (c). This area only appears at a certain TOB range, which is why wave cancellation can be considered a viable reason for its occurence.

The high-frequency plots in Fig. 4.10 exhibit a more expected behaviour. As for the SL plots before (Fig. 4.9), there is a distinctly louder source at the nozzle outlet with downstream directivity. Due to its position in direction of flow, the increased SPL could result from flow interaction with the wing leading edge and the pylon. Besides, there is an area of increased SPL compared to the uninstalled case for

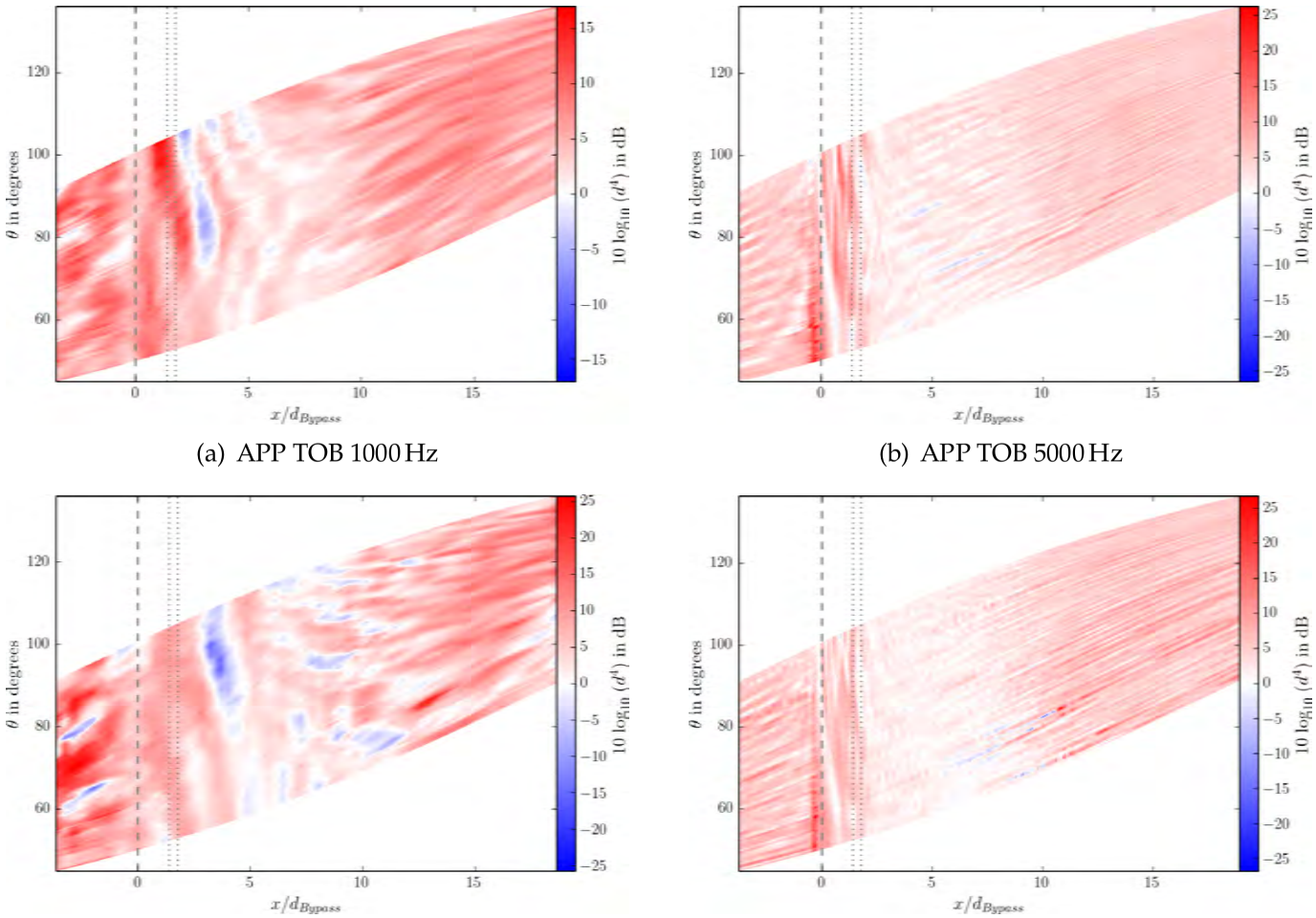

(a) APP TOB 1000 Hz

(b) APP TOB 5000 Hz

(c) CB TOB 800 Hz

(d) CB TOB 6300 Hz

Figure 4.10: *Selected source directivity comparison plots of different TOBs of approach (DLR 287 and DLR 395) and cutback (DLR 279 and DLR 411) TPs (baseline nozzle with and without wing installation.*

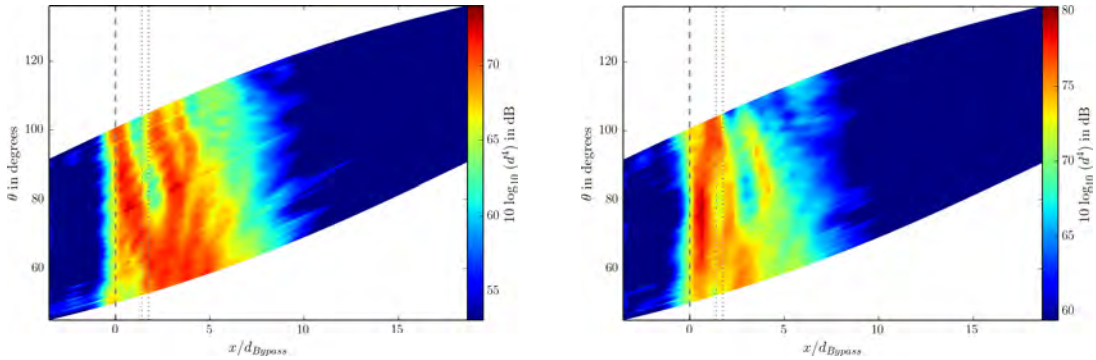

(a) Isolated. (b) Installed.

Figure 4.11: *Isolated and installed approach TPs (DLR 287 and 395), short cowl engine, TOB* 1000 Hz*. The cutback TPs show similar behaviour.*

$x/d = 0 - 2$, which coincides with the chord dimension of the wing and could result from turbulent surface interaction. During approach, the SPL difference is greater by approximately 3 dB. Downstream of the wing, the SPL of both installed and uninstalled wing jet are of similar magnitude, meaning that the noticable SPL increase happens not in the jet mixing area, but near the wing due to flow-surface interaction and subsequent turbulence generation, which agrees with the theory presented in Sect. 2.3.3.

4.3.2 Reference Measurement Points with Flight Stream

The second part of the reference point analysis deals with the same uninstalled and installed test configurations as the previous one, only this time with flight stream simulation. All other testing conditions remain unchanged. This includes the engine configuration, nozzle design as well as core and bypass flow velocities. Therefore, all changes to the sound field can be attributed to the flight stream. The flight stream velocity is 70 ms^{-1} for approach and 90 ms^{-1} for cutback and sideline flow conditions. As before, the focus of this section is on the SL condition; comparisons will be made with the isolated test points shown in the previous section. Cutback and approach TPs are being explained in reference to the sideline condition presented.

Isolated sideline ICAO reference point with flight stream

Figure 4.12 shows the SODIX plots for FS sideline conditions without wing installation for the same TOB as Fig. 4.8.

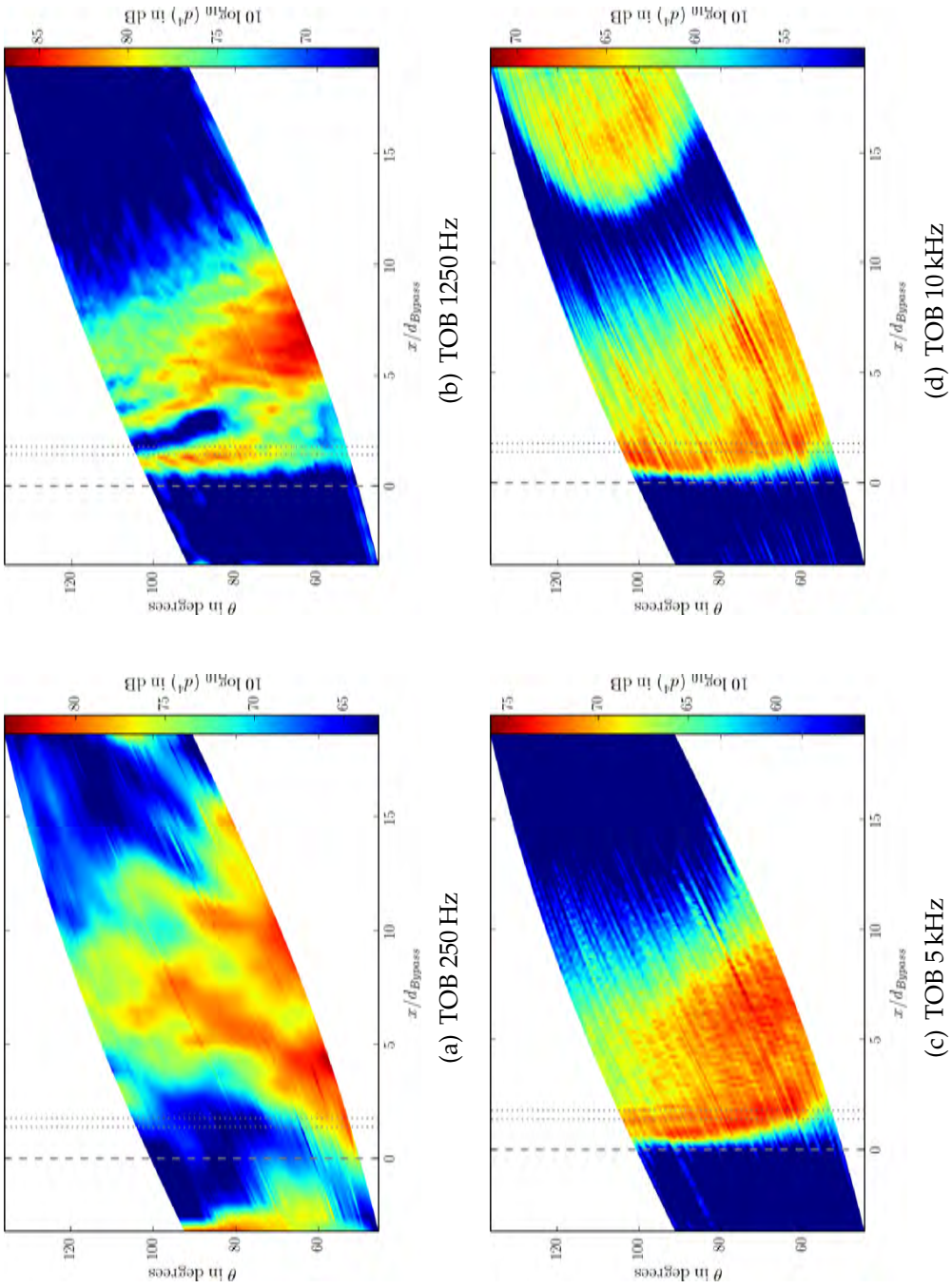

(a) TOB 250 Hz (b) TOB 1250 Hz

(c) TOB 5 kHz (d) TOB 10 kHz

Figure 4.12: *Source directivity plots of different TOBs of DLR 325 (baseline nozzle at sideline conditions, without wing installation and with flight stream).*

As shown in Sect. 4.2, the flight stream influences the sound field at the lowest frequencies (e.g. TOB 250 Hz). It is visible at the far left end of the directivity matrix and depending on the frequency has a SPL of $85 - 95$ dB, decreasing for increasing frequency. For lower frequencies, the flight stream noise overrides the jet sound events, resulting in unintelligible plots when the source position grid in Fig. 3.12 is used, see Fig. 4.13.

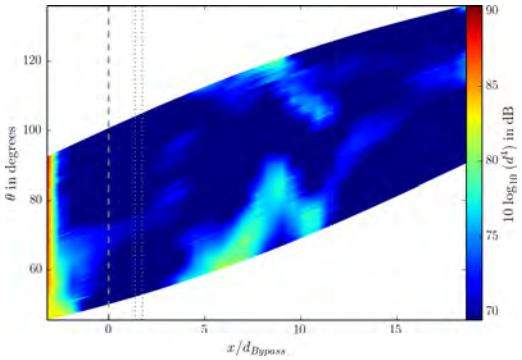

Figure 4.13: *Flight stream dominance over the sound field observable at low frequencies, TOB* 125 Hz *of DLR 325. Due to the dynamic range of the plot, the other mixing sources disappear.*

At higher frequencies,jet mixing noise dominates and so the plots look similar to the isolated cases. The overall SPL drops significantly compared to the isolated test setup. The difference amounts to up to 20 dB. This can be attributed to the fact, that the slow flight stream surrounds the fast core jets. According to Lighthill's theory of sound (see Sect. 2.3.3) the source strength is proportional to a higher power of the velocity difference. It has to be considered that during real flight, the FS and the SPL reduction it entails are always present, resulting in a significantly different noise characteristic as during isolated, land-based testing. Another noticable effect is the refraction of sound waves caused by the FS. Sound waves are pressure fluctuations, and as such are always convected with a flow and refracted between fluids of different velocity. To a lesser extent this effect also appears between core and bypass jets, but it is more pronounced with FS activated as the diameter of the NTF FS nozzle is relatively greater than that of the aeroengine jets. The refraction causes sound events to appear farther downstream than their actual occurence. As this work does not use shear layer correction, the resulting offset in direction of flow is observable in all TOBs in Fig. 4.12, but can be further emphasized by inspecting the comparison plot of isolated (*DLR 317*) and flight stream (*DLR 325*) test points (Fig. 4.14). The dark blue area at the nozzle outlet equates to a lower SPL in the flight stream test.

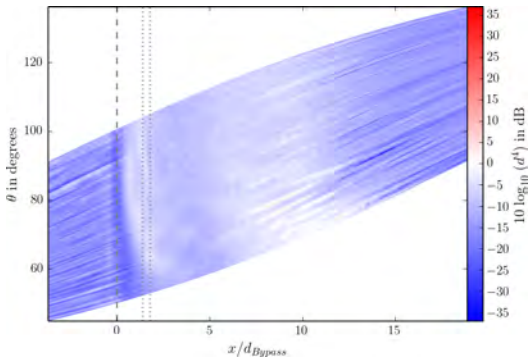

Figure 4.14: *Sound wave refraction caused by the flight stream, TOB* 5000 Hz *of DLR 325 and DLR 317. The FS displaces sources by* $\approx 0.5x/d$.

The sound directivity characteristics of the plots of *DLR 325* in Fig. 4.12 are similar to those of the uninstalled testing case. There appears to be a general rearward directivity for low frequencies. Again, it can not be ruled out that the true noise source is further downstream and therefore outside the angular range of the plot.

Installed sideline ICAO reference point with flight stream

The wing effect comparison directivity plots for sideline conditions with FS are shown in Fig. 4.15.

The plots show no large differences to the experiments without FS (Fig. 4.9). Again, the addition of flight stream simulation moves sound events downstream due to refraction effects. This happens irrespective of whether a wing is installed or not. However, the absolute SPL difference between TPs with and without flight stream is noticable. Whereas wing installation results in an up to 10 dB increase in sound intensity without FS simulation, the experiments with FS exhibit an up to 20 dB SPL increase compared to no FS, being greater for intermediate TOBs. As the wing is fully engulfed by the flight stream, the additional noise difference most likely results from flow interaction with the wing surface. It has to be noted that the flight stream only increases the relative difference between installed and isolated test cases, but has an overall reduction effect on the SPL as explained above. The directivity of the sound events is similar between both configurations as well, though the plots appear to be more blurry when the flight stream is enabled. Besides this, there are the same additional sources: One at the nozzle outlet radiating to the front microphones and one encompassing the wing and radiating mainly downstream. The area with reduced sound pressure just behind the wing at TOB 1250 Hz is also present and even more pronounced.

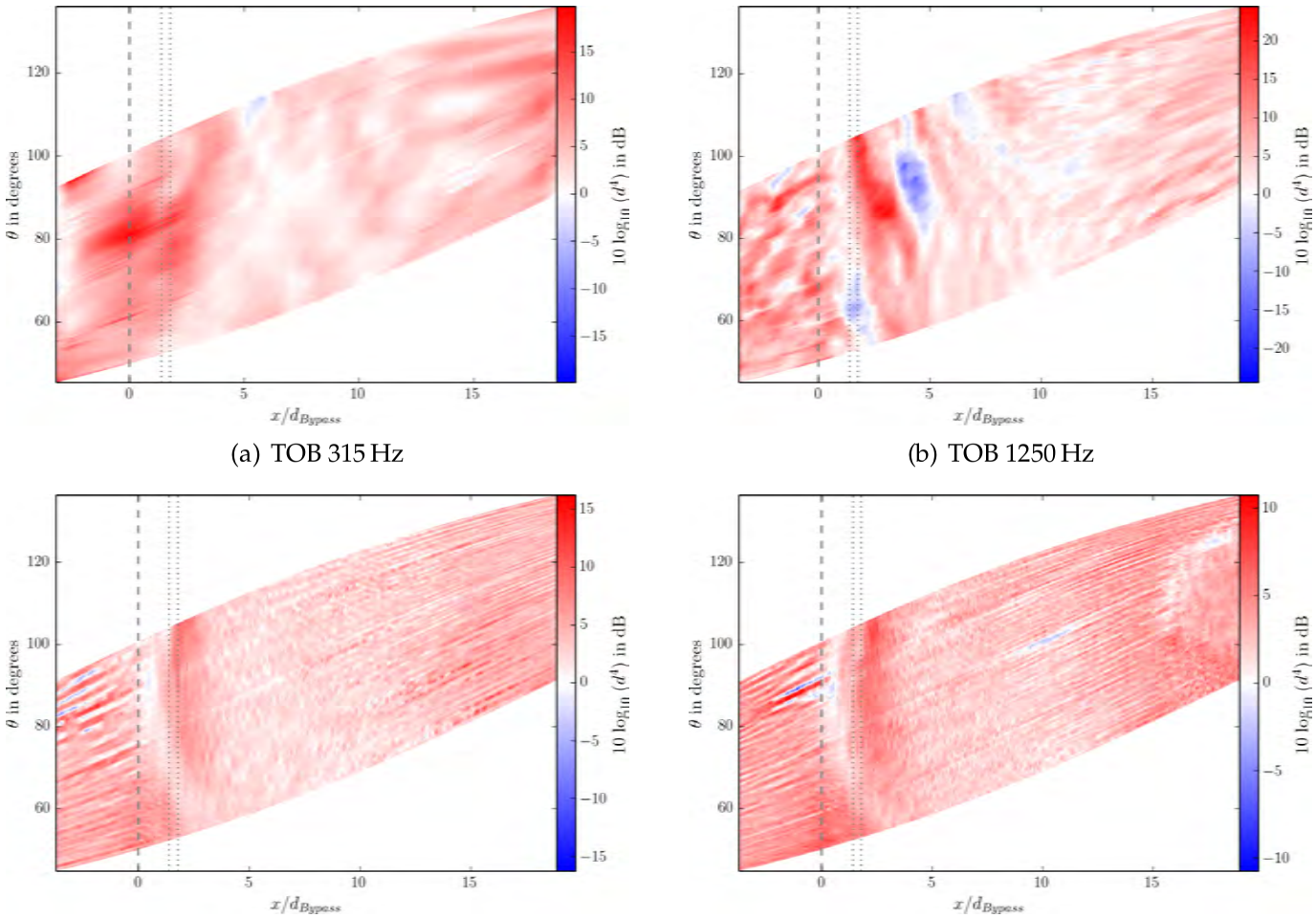

(a) TOB 315 Hz

(b) TOB 1250 Hz

(c) TOB 5 kHz

(d) TOB 8 kHz

Figure 4.15: *Source directivity comparison plots of different TOBs of DLR 443 and DLR 325 (baseline nozzle at sideline conditions with and without FS, wing installed).*

Moreover, the low-frequency plots show a noticable SPL increase upstream of the nozzle. As the flight stream velocity is the same for installed and isolated cases, this increase has to come from wing installation effects alone. However, it is uncertain as to why additional noise sources occur along the nacelle when the wing is installed, as it would need some sort of upstream influence on the turbulence of the flow to achieve this effect.

Installed approach and cutback ICAO reference points with flight stream

Figure 4.16 shows the comparison plots for installed and isolated approach and cutback TPs with flight stream enabled.

The large dynamic range of the approach and cutback comparison plot at TOB 1250 Hz is because of the relative SPL difference between installed and isolated TPs of up to 75 dB. There are areas within the original sound field which exhibit sound pressure values that result in negative decibel values, i.e. below the hearing range. For reference, the non-comparison plots with full dynamic range are shown in Fig. 4.17. It can be seen that the appearance of the comparison plots can be traced back to the areas of very low sound pressure, which render the comparison plot unintelligible. It has to be noted, that due to the logarithmic nature of hearing, plots using a full dynamic range do not possess much physical validity; generally speaking, sound events that are more than 25 dB below the main sound event are indistinguishable to the human ear and as such are not relevant when assessing the sound field data. All plots in this thesis using such a scale are therefore for demonstration purposes only.

The question remains, as to why the uninstalled approach and cutback TPs show areas with a SPL of approximately 0 dB, whereas the same behaviour is not observable for the sideline TPs, though there is no difference between SL and CB conditions besides the core and bypass flow velocity and the day of testing (one day apart). It is likely that this error occured during SODIX calculation, i.e. that SODIX continuously and erroneously emphasized a distinct region during the 200 iteration steps run on this simulation. However, reducing the amount of iteration steps or changing the value of σ_1 is no solution to this problem, as this does not change the source distribution, but merely the dynamic range (see Sect. 2.3.4 and 3.2.2). The high-frequency plots are similar to the SL TP, though the defective microphone makes the difference appear more significant than it is.

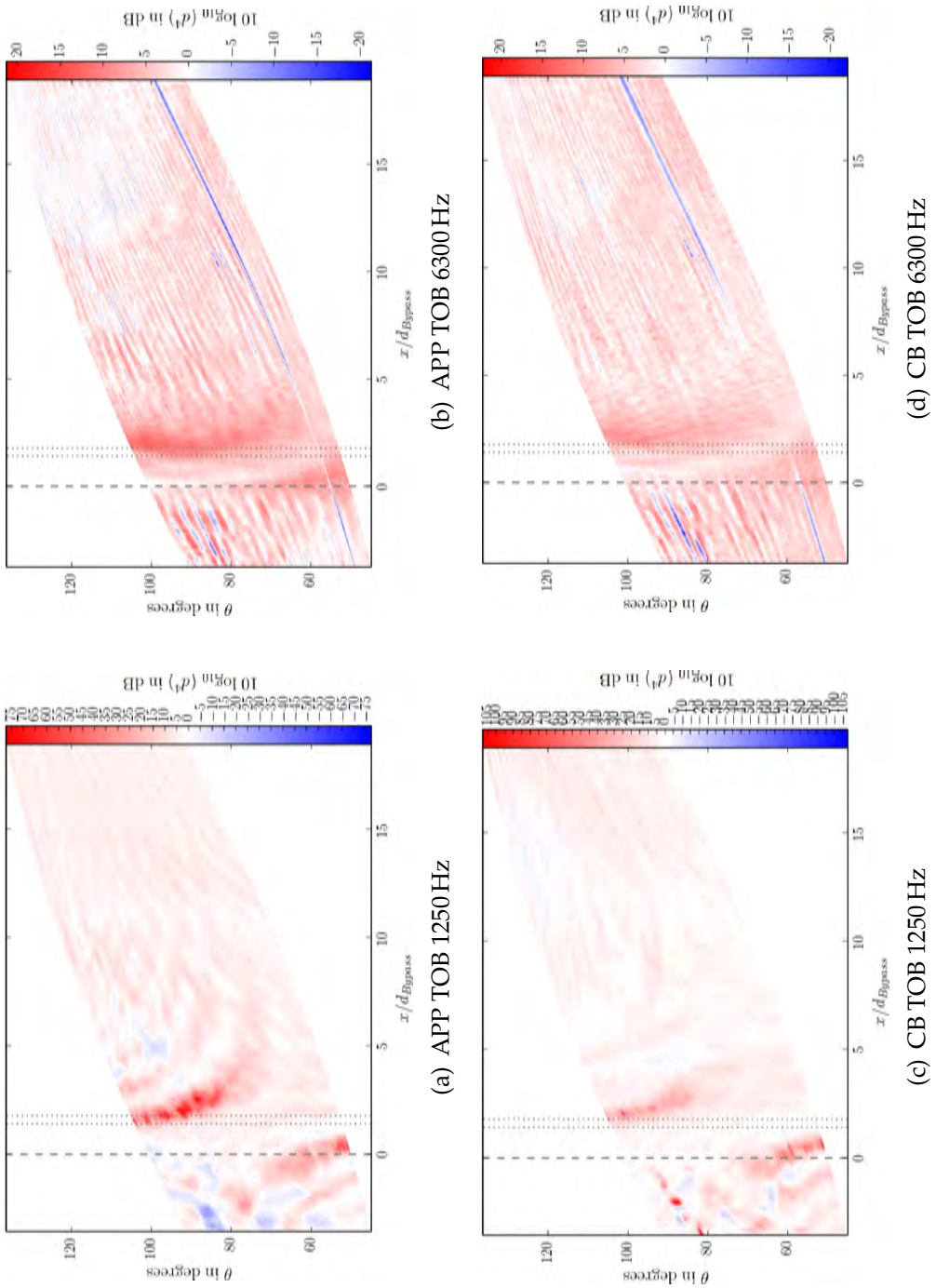

(a) APP TOB 1250 Hz (b) APP TOB 6300 Hz

(c) CB TOB 1250 Hz (d) CB TOB 6300 Hz

Figure 4.16: *Selected source directivity comparison plots of different TOBs of approach (DLR 297 and DLR 403) and cutback (DLR 257 and DLR 423) TPs (baseline nozzle with and without FS, wing installed).*

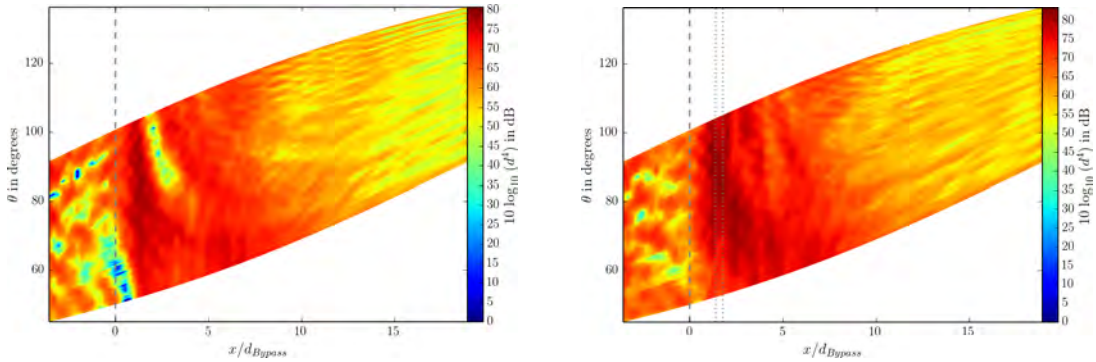

(a) Isolated, DLR 257 (b) Installed, DLR 423

Figure 4.17: *Isolated and installed cutback TPs with FS (DLR 257 and 423), TOB* 1250 Hz. *Dynamic range of the plot is the absolute SPL maximum. The displacement of some areas causes the comparison plot to have a large dynamic range.*

4.4 Broadband Fan Noise Simulation

The broadband noise generation is described in Sect. 3.1.4. Its main purpose is to simulate the typical rearward fan noise from the bypass duct. The test points relevant for this section are shown in Table 4.2 alongside their configuration and flow conditions.

Table 4.2: *Broadband test points. All tests were carried out on a short-cowl engine with baseline nozzle configuration.*

DLR TP	Condition	Flight Stream	Wing	Excitiation
306	No flow	No	No	BB
383	No flow	No	Yes	BB
350	SL	Yes	No	BB-A
444	SL	Yes	Yes	BB-A

No Flow Conditions

In order to exemplify and verify the sound generation, tests were run without any additional flow (neither jet nor flight stream). The broadband sound excitation of those tests spanned all relevant frequencies and was not limited to a certain frequency range. Employing the usual 20 dB dynamic plot range, only the noise emanating from the speakers is visible on the nozzle exit plane, possessing a uniform directivity and vanishing in close proximity to its first occurence,

exemplified on TOB 2000 Hz in Fig. 4.18(a). The sound field with the wing installation is similar, though reflections are detected at the half wing span and at the wing tip for this frequency. The maximum SPL is about 2 dB higher when a wing is installed.

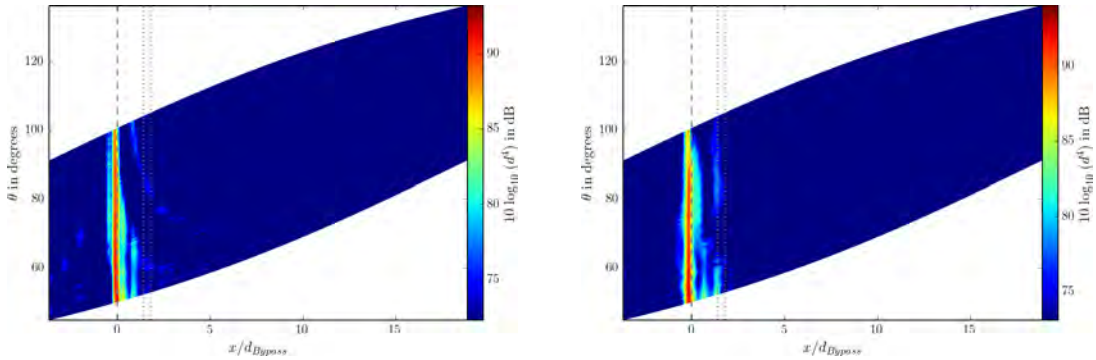

(a) Isolated (b) Installed

Figure 4.18: *Broadband noise excitation with no additional flow (DLR 306 and DLR 383), TOB* 2000 Hz.

Increasing the dynamic range to the absolute maximum of the plot, however, reveals another aspect of the no flow tests. Throughout all frequencies, coherent patterns occur in the plots, see Fig. 4.19. This cannot be attributed to the aliasing effect discussed in Sect. 4.1, as the trace wave length adheres to $\lambda_s < 2\Delta x_m$ at lower frequencies and may instead be a result of the spatially discrete noise simulation of the speaker rings (Fig. 3.5). Experience showed, that SODIX has difficulties localizing the position of coherent sources, such as the speakers, resulting in unphysical patterns. As for the CB and APP TPs (Fig. 4.17), the isolated plot shows areas of extremely low sound pressure.

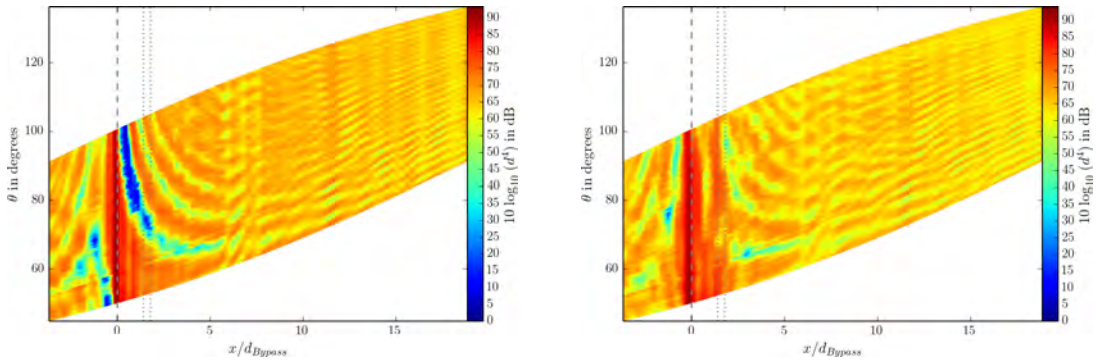

(a) Isolated, DLR 306 (b) Installed, DLR 383

Figure 4.19: *Broadband noise excitation with no additional flow (DLR 306 and DLR 383), TOB* 2000 Hz. *Dynamic range of the plot is absolute SPL maximum.*

Sideline Conditions with Flight Stream

Sideline conditions were chosen to investigate the influence of broadband noise with enabled jet flow over approach and cutback conditions. Figure 4.20 shows the plots for TPs *DLR 350* and *444*, with the standard 20 dB dynamic range. There is one malfunctioning microphone in Fig. 4.20(a) showing as a dark blue line.

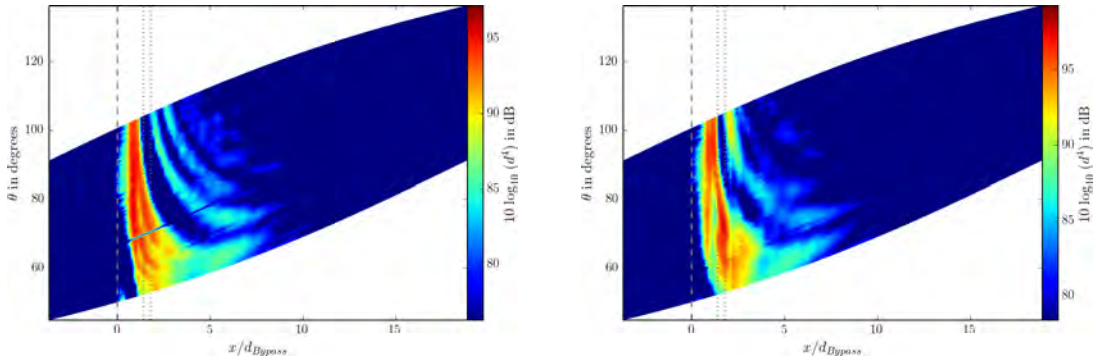

(a) Isolated, DLR 350 (b) Installed, DLR 444

Figure 4.20: *Broadband noise excitation with sideline flow conditions and flight stream enabled, TOB* 2000 Hz.

The absolute SPL maximum is higher compared to the no flow case presented before, which is to be expected, considering the turbulent mixing noise caused by the core mass flow. In addition, the sound source distribution is concentrated in a smaller area, meaning that the mixing sources that usually occur further downstream of the nozzle are less significant than the simulated broadband noise. The directivity of the source field is similar to the no flow case described above, being relatively uniform with the strongest sources close to the nozzle. The presence of the flight and core streams causes the main sound source to appear more diluted, as the sound waves are refracted in the shear layer of the jet. The wing presence causes the maximum SPL to rise by approximately 3 dB, which is significantly lower compared to previously assessed TPs with similar conditions but without broadband sound excitation (*DLR 325* and *443*). There is a new source at the wing tip with forward directivity that is about 10 dB below the main sound source. In addition, the directivity of the main source changes slightly; it moves further to the flap and has a more pronounced rearward emission. It is notable, that this time an area of very low SPL occurs when the wing is present, Fig. 4.21. This gives further credence to the assumption that this area results from the SODIX calculation in conjunction with the experiment setup and is not an actual physical phenomenon.

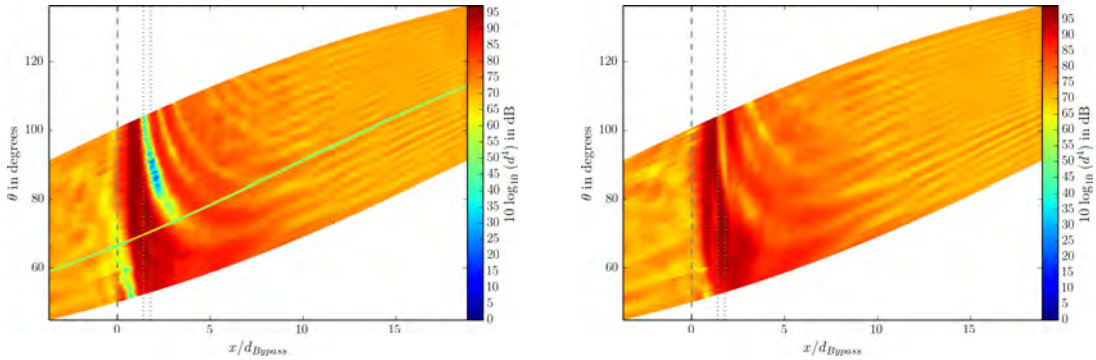

(a) Isolated, DLR 350 (b) Installed, DLR 444

Figure 4.21: *Broadband noise excitation with sideline flow conditions and flight stream enabled, TOB* 2000 Hz. *Dynamic range of the plot is absolute SPL maximum.*

In conclusion, the broadband sound excitation used in the scope of this experiment raises the maximum SPL by an average 10 dB compared to test cases without additional noise generation. Moreover, the BB noise is comparably louder than the flight stream mixing noise, which was intented according to the test reports. The presence of flight and core streams enhances the total SPL of the sound field even further. The broadband noise sources are located close to the nozzle, have a uniform directivity and with increasing distance from the nozzle there are fewer and weaker sources.

4.5 Nozzle Configurations

In this Section, the effects of the serrated and scarfed nozzle geometries in comparison to the baseline nozzle are assessed. In order to reduce the amount of data, all tests mentioned in this Section were carried out using sideline conditions with flight stream, because this is the most representative and critical condition of all the test conditions available. Table 4.3 lists the test points and their parameters. Comparisons are then made to the baseline nozzle with SL and FS (*DLR 325*).

4.5.1 Serrated Nozzle

Full-scale spectral analysis by Rolls-Royce acquired via personal communication suggests that the serrated nozzle installation provides an up to 3 dB noise decrease at low frequencies equivalent to up to 1250 Hz. Above this threshold, the

Table 4.3: *Nozzle geometry test points. All tests were carried out using sideline conditions and flight stream without additional sound excitation.*

DLR TP	Nozzle	Wing
527	Scarfed	No
599	Scarfed	Yes
735	Serrated	No
817	Serrated	Yes

serrated nozzle promotes noise generation, having an up to 2 dB higher emission level than the baseline configuration. This effect was desired by the designers, because low-frequency noise was deemed more tenuous as it is less affected by atmospheric attenuation. Sound field analysis using SODIX cannot confirm these effects definitely, as the whole sound field changes appearance depending on the installed nozzle, but hint at a similar behaviour. Figure 4.22 shows a low-frequency plot of the isolated and installed serrated nozzle configuration tests. There is a malfunctioning microphone in Fig. 4.22(a).

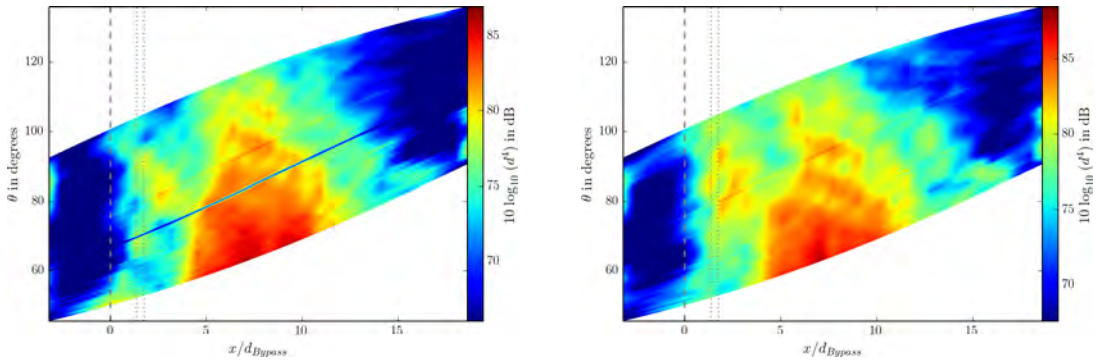

(a) Isolated, DLR 735 (b) Installed, DLR 817

Figure 4.22: *Serrated nozzle configuration, sideline condition, TOB* 500 Hz.

Both plots do not deviate significantly from the baseline plots in Fig. 4.12. Again, the wing presence increases the SPL maximum by approximately 2 dB and causes additional sound sources to appear in close proximity to the wing. Moreover, for higher frequencies (not displayed here), the main noise source shifts from the downstream mixing event of core and bypass flow to the nozzle exit area, which reflects expected behaviour (see Fig. 2.5). The serrations of the nozzles are geometrically designed to specifically reduce sound emission at lower frequencies [32]. Figure 4.23 shows a comparison plot for the serrated and the baseline nozzle at a low and high TOB respectively. Negative (blue) dB values mean a

lower sound emission due to the serrated nozzle. Because of a defective microphone, the dynamic range of the plot had to be limited to 15 dB.

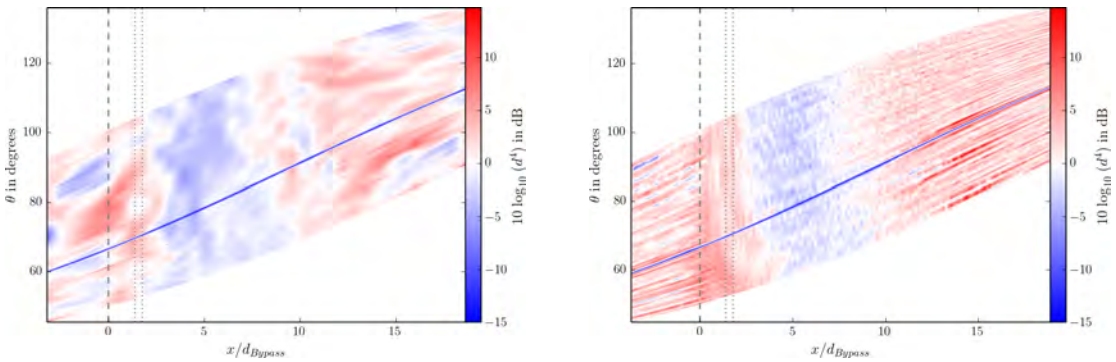

(a) TOB 500 Hz (b) TOB 5000 Hz

Figure 4.23: *Serrated nozzle configuration compared to the baseline nozzle, sideline condition, no wing installed.*

Whereas the sound field at 500 Hz does not allow a clear interpretation due to its blurred appearance, it does reflect the trend of the high frequency plot. In general, the serrated nozzle seems to reduce the SPL in the mixing area of the jets by about 5 dB. In other areas of the sound field whose absolute SPL is well below the main source, the SPL is increased. Comparing the SPL maximum of all SODIX plots, the serrated nozzle provides an advantage of $1-4$ dB for frequencies below 1600 Hz and above 4000 Hz. Inbetween this span, the serrated nozzle plots show an absolute increase of roughly $1-2$ dB. This behaviour coincides with the result obtained by RR for frequencies up to 4000 Hz; above this threshold, the average maximum SPL should increase when using serrated nozzles according to the data analysed by Rolls-Royce. This difference can be attributed to the fact that SODIX analyses the full sound field instead of just the spectra of a polar microphone array. In addition, the linear microphone array was placed in the near field of the nozzle, whereas the polar array was located in the far field. All in all, the serrated nozzle achieves the expected sound reduction, but it has to be designed very carefully in order to avoid a high frequency noise increase which could outweigh the low frequency benefits, resulting in large implementation costs when applied to civil aviation engines. Despite this fact, so-called chevron nozzles have become widely used in modern civil aeroengines.

4.5.2 Scarfed Nozzle

Compared to the serrated geometry, the scarfed nozzle is a rather simple implementation of noise reduction technology. The scarfed appendix extends downstream of the baseline nozzle exit plane in order to preserve the flow area of the baseline nozzle. Figure 4.24 shows two selective TOBs of the isolated and installed scarfed nozzle test.

Again, the plots exhibit the same general behaviour that could be observed for all experiments. The main source has rearward directivity and reaches its peak intensity at $St \approx 1$ at $x/d_{Bypass} = 5$ and consists mostly of low-frequency mixing noise. The high-frequency noise occurs closer to the nozzle and radiates mainly into the forward quadrant. Wing presence also causes the commonly observable higher frequency ($f > 500\,\mathrm{Hz}$) sound sources to appear close to the wing trailing edge. Interestingly, the wing does not add to the maximum SPL at lower frequencies when a scarfed nozzle is installed. Instead, it only increases the total noise emission at higher frequencies ($f > 4000\,\mathrm{Hz}$), and then only by $1 - 2\,\mathrm{dB}$. Compared to the baseline nozzle, the main sound source possesses a slightly more pronounced forward directivity and has moved upstream by approximately one nozzle diameter. In addition, noise sources close to the nozzle are more dominant for the scarfed build. The intensity of the sound field does not change much, however. The scarfed nozzle lowers the maximum SPL by 1 dB at maximum for frequencies between $1 - 2\,\mathrm{kHz}$. Investigation of the isolated comparison plot of baseline and scarfed nozzles (Fig. 4.25) confirms that the high-frequency mixing noise close to the nozzle moves slightly downstream, most likely due to the scarfed lip of the nozzle acting as an artificial sound barrier.

It can be concluded that the scarfed nozzle build has a positive effect regarding interaction noise, but does not significantly change the sound field concerning mixing noise. Since it is comparably easier to fully design and optimise a scarfed nozzle than a serrated one, the former may act as a cheaper substitude to the more demanding serration designs. The added mass has to be weighted against the sound reduction effect.

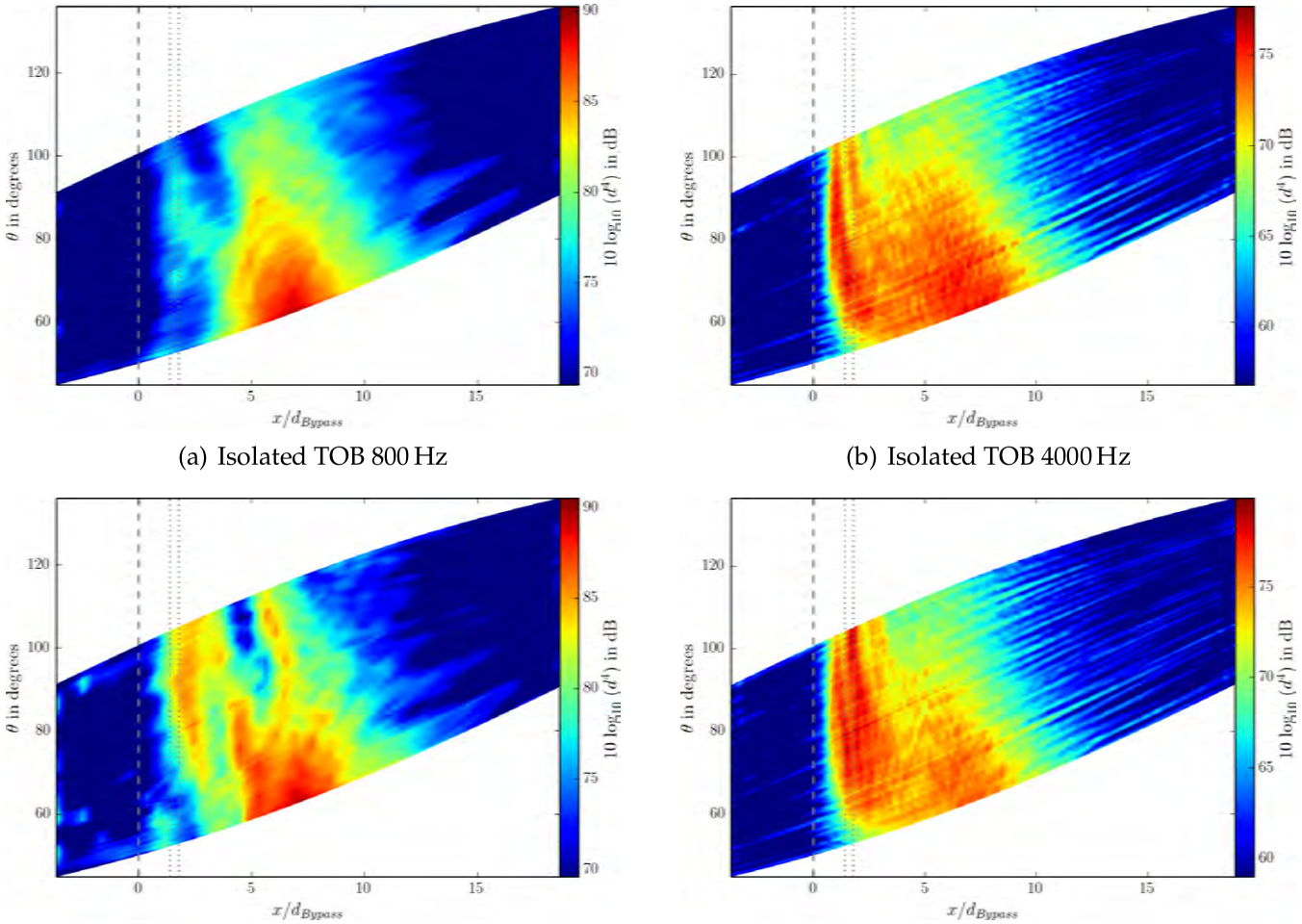

(a) Isolated TOB 800 Hz

(b) Isolated TOB 4000 Hz

(c) Installed TOB 800 Hz

(d) Installed TOB 4000 Hz

Figure 4.24: *Selected low and high-frequency plots of isolated (DLR 527) and installed (DLR 599) TPs at sideline conditions with the scarfed nozzle geometry.*

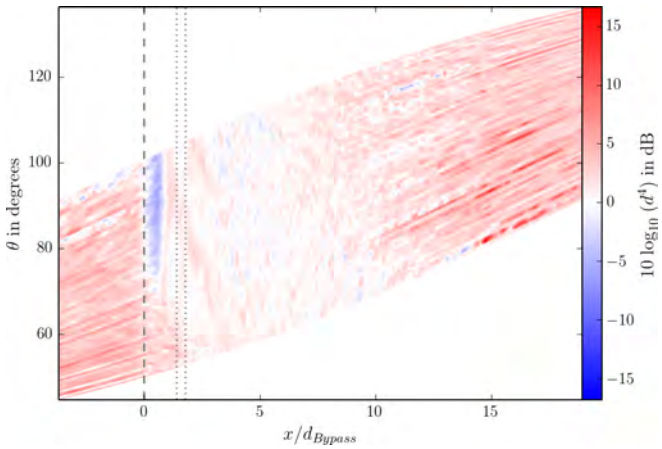

Figure 4.25: *Scarfed nozzle configuration compared to the baseline nozzle, sideline condition, no wing installed.*

4.6 Long Cowl Engine

The long cowling configuration was tested without a wing and with baseline and scarfed nozzle configurations only (see Sect. 3.1.4). Therefore, this Section will focus only on two long cowl (LC) TPs and compare these with the baseline short cowl (SC) configuration. Both configurations have the same thrust output. Table 4.4 lists the relevant TPs for this Section. The scarfed nozzle plots have been omitted, as this nozzle design did not show significant differences or benefits compared to the baseline configuration.

Table 4.4: *Long cowl test points. All tests were carried out at sideline condition without wing installation and additional sound excitation.*

DLR TP	Nozzle	Flight Stream
900	Baseline	No
914	Baseline	Yes
1003	Scarfed	Yes

Long cowl engine without flight stream

Figure 4.26 shows two selective TOBs of the no flight stream TP. Plots of the reference baseline point, *DLR 317*, can be found on page 51.

Compared to the baseline TP, the long cowling causes the average maximum SPL to drop by about 5 dB over all frequencies, which equates to a significant decrease in the subjectively perceived noise. Furthermore, secondary noise sources drop

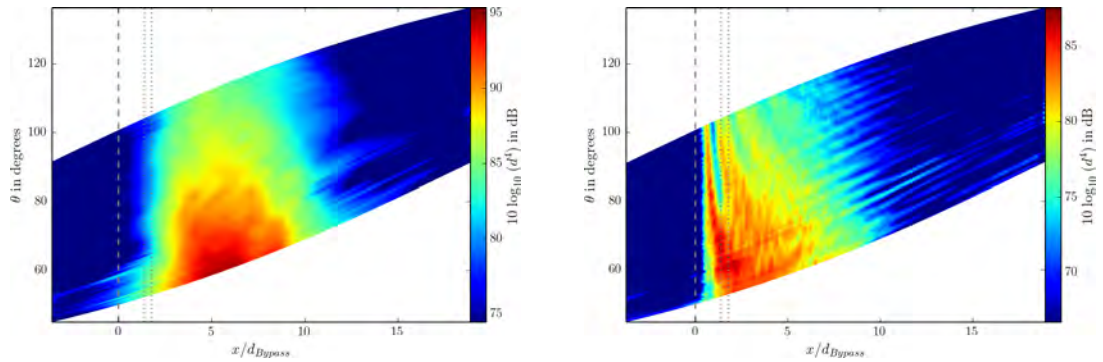

(a) TOB 630 Hz (b) TOB 3150 Hz

Figure 4.26: *Long cowl nozzle configuration, sideline condition, no flight stream (DLR 900).*

by up to $10-15$ dB, their SPL being lower for higher frequencies. The comparison plots shown in Fig. 4.27 highlight additional differences between short and long cowl configurations.

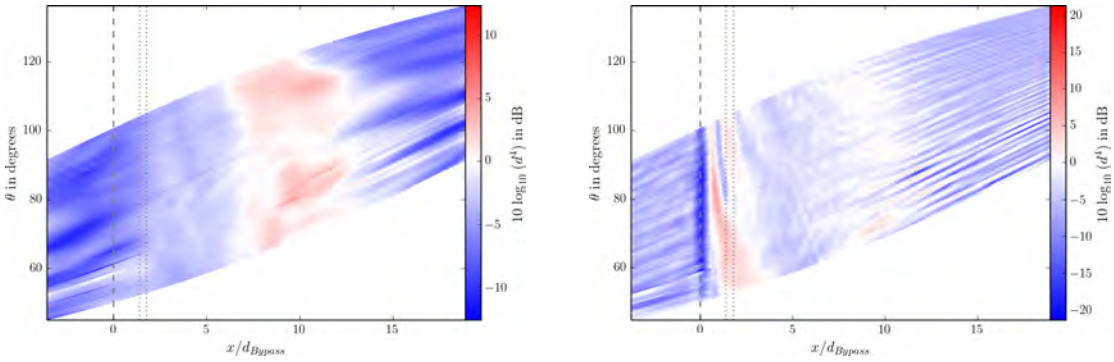

(a) TOB 630 Hz (b) TOB 3150 Hz

Figure 4.27: *Long cowl nozzle configuration (DLR 900), sideline condition, no flight stream compared to the baseline configuration at the same conditions (DLR 317).*

Though the long cowl configuration exhibits an overall lower maximal SPL, the low-frequency mixing area is in fact longer compared to the short-cowl engine; it extends by about two nozzle diameter upstream as well as downstream. At higher frequencies, there is significantly more noise with relatively uniform directivity at the nozzle exit plane for the long cowl configuration. As the flow is pre-mixed inside the cowling before being exhausted into the environment, the average flow velocity of the jet is slower compared to the SC engine. At the nozzle exit plane, however, the flow velocity is greater, as the SC core flow is surrounded by the slow and cold bypass flow. The noise entailing from the flow is in

accordance to Lighthill's *Theory of Sound* (Sect. 2.3): The LC engine exhibits more sound sources close to the nozzle, but is of less sound intensity overall. Moreover, the first LC sound source has shifted well downstream the marked nozzle exit plane. This is especially noticable for higher frequencies, as the SODIX plots are of higher resolution then due to a greater number of source positions used. The shift is most likely due a moved origin of coordinates that has not been accounted for during SODIX analysis. Therefore, the dashed line in all plots marks the position of the SC exit plane, whereas the LC engine exit plane is approximately one nozzle diameter further downstream.

Long cowl engine with flight stream

Enabling the flight stream has the same effect on the LC engine as on the SC. Figure 4.28 shows TP *DLR 914* at the same TOB as for *DLR 900* in the Section above.

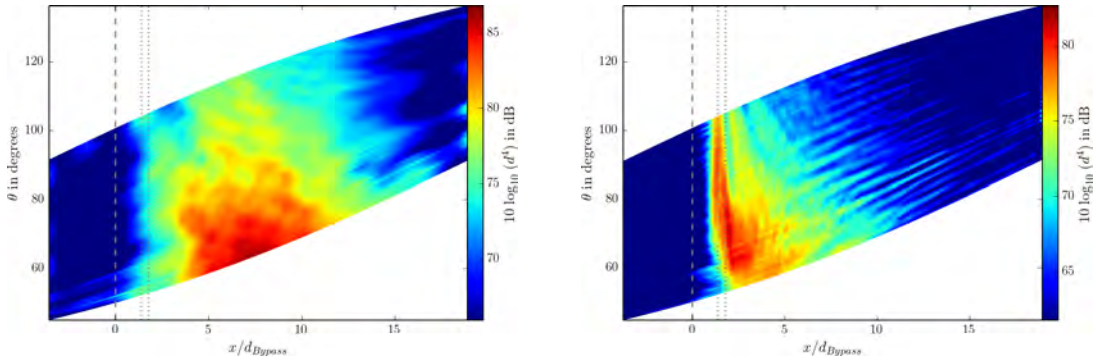

(a) TOB 630 Hz (b) TOB 3150 Hz

Figure 4.28: *Long cowl nozzle configuration, sideline condition, flight stream enabled (DLR 914).*

The flight stream causes sound sources to appear further downstream and more spread out due to wave refraction. In addition, the FS encases the hot and fast core flow, which lowers the maximum SPL by $6 - 12$ dB, having the greatest effect at lower frequencies. The degree by which the flight stream reduces noise emission is comparable to the TPs presented before. When comparing the LC TP with the SC TP that has the same conditions (*DLR 325* on page 57), the long cowl nozzle still has a noise reduction effect at low frequencies due to emitting less downstream mixing noise than the SC configuration. At higher frequencies $f > 2000$ Hz, however, the effect reverses: The high-frequency noise close to the

nozzle exit plane described in the Section above causes the sound field of the LC engine configuration to have a higher maximum SPL. Interestingly, this only occurs when the a flight stream is present; during the no FS test described above, the SC nozzle had a greater maximum SPL at all frequencies. This fact is further evidenced by the comparison plot in Fig. 4.29 (blue color equals to less absolute sound pressure on the long cowl configuration). From left to right, the plot first shows the offset of the long cowl nozzle exit plane along the abscissa, then the high intensity sound source followed by an area of relatively low intensity mixing noise.

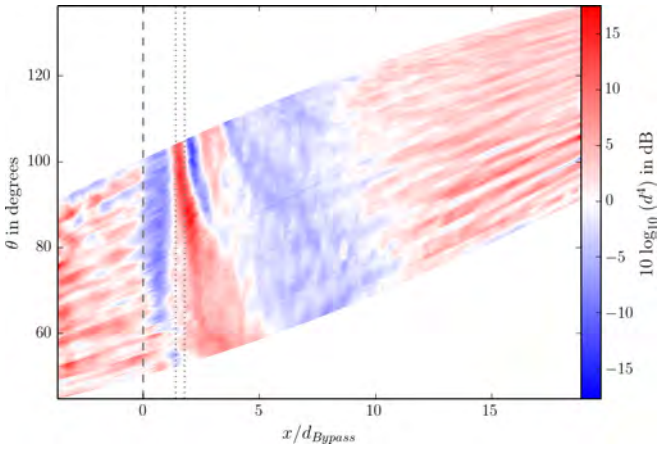

Figure 4.29: *Long cowl nozzle configuration (DLR 914) compared to the short cowl nozzle (DLR 325), sideline condition, no wing installed, TOB* 2000 Hz.

4.7 Remarks

This Section contains concluding remarks on the test conduction and the digital tools used for data assessment. Judging by the availability and readability of the raw data, the test has been carried out meticulously. The previous Sections highlighted some difficulties regarding the raw data validity, however. This concerns the quality of the microphones, that proved to be compromised in the high-frequency range at the most tenuous test conditions, showing significant differences in their frequency response. Moreover, the spacing of the microphones was not optimised for high-frequency sound immision, especially so for the rear section of the array, resulting in extensive aliasing effects for higher TOB plots. It is therefore advised to match the microphone spacing to the tracewave length criteria presented in Sect. 4.1 and optimise the spacing accordingly if comprehensive

results for high frequencies are to be obtained. This of course has to be weighted against other factors such as costs, microphone diameter and possible installation positions, though the latter two were not of concern for the OPENAIR test. In addition, the low-frequency mixing noise of the jet occurs at the bottom part of the SODIX plots, meaning that it is only picked up by the downstream part of the linear array. It is therefore uncertain whether the most intense section of the mixing is inside the measured area. A downstream extension of the microphone array would allow to capture the whole jet mixing area and provide a clearer view on the sound field of the jet.

The SODIX algorithm proved to be a stable source directivity analysis tool. The very low-frequency (up to 500 Hz) plots suffer from low resolution that could not be completely alleviated by increasing the source position grid density, but due to engine scaling effects (see Sect. 2.2.1), these frequencies are not of interest, as they at the low end of the audible range when scaled. The aliasing effect occuring for higher frequencies is a common problem of source localization methods. According to the findings of this thesis, it results from the discrete and regular microphone spacing, is in the data and cannot be compensated in the analysis. Internal experience showed, that the aliasing present when assessing the sound field with SODIX is comparably weaker to other source localization methods such as beamforming. However, the aliasing effect prevented the shortening of the source position grid to reduce the calculation time.

A python routine for plotting and comparing the SODIX output was written in the scope of this thesis. The output of the comparison plot routine proved difficult to interpret, however, when great differences in SPL were detected between different test cases. Though this issue was partly alleviated by limiting the maximum dynamic range on the plot, this solution only acts as a workaround. One possible approach would be to weigh the local SPL in relation to the absolute maximum, giving large relative differences a reduced impact on the overall field and thus enhancing the difference of the main sources while lowering the significance of secondary events, though this would further complicate readability and interpretation of the sound field for readers unexperienced with SODIX. In addition, the object-oriented plot routine has been designed open-ended for usage beyond this thesis. As such, implementation of a graphical user interface to facilitate accessibility would be a desirable enhancement of the tool.

5 Conclusion and Outlook

The subject of this thesis was the analysis of the aeroacoustic OPENAIR experiment carried out in summer 2012 in order to examine the sound field of the core and bypass jet flow of a generic turbofan aeroengine under a multitude of test conditions. These conditions included different nozzle geometries and cowling configurations, flight stream simulation emulating ICAO noise measurement reference points, broadband sound excitation simulating rearward fan noise and installation effects evoked by the presence of the aircraft wing and pylon. The thesis employed the sound directivity analysis algorithm SODIX that was developed by DLR in order to assess the sound field of the aeroengine jet. The experience that was gained during analysis preparation on how to configure the source directivity analysis tool SODIX is presented, including recommendations regarding the source position grid design as well as the slack variable and iteration steps values. The thesis also served as a verification basis for SODIX, offering insight into various issues that were yet undiscovered, such as the aliasing for short wavelengths and low-frequency sound field dilutation. Though the algorithm proved more stable than established beamforming methods according to experience, there is still potential for optimisation.

By establishing a theoretical basis of the working priniple of turbomachinery, jet fluid mechanics and aeroacoustics, the advantages and disadvantages of various configuration combinations were successfully shown. In accordance with the theory, the maximum SPL was found to be at $x/d = 5$ with $St = 1$ with sources moving closer to the nozzle for increasing frequencies and vice versa. When a wing was present, the source field changed: At higher frequencies, additional sources appeared on the wing underside and at the flap tip. When present, the flight stream moved sources downstream, because the sound waves were refracted in the shear layers between the jets of different velocity. Wing and flight stream presence were found to have a comparable influence on the sound intensity: The former effect increased the maximum SPL of the sound field by approximately $5 - 10\,\mathrm{dB}$, whereas the latter decreased the noise emission by generally the same

amount. Both effects cancelled each other out in most test cases, resulting in a sound field comparable to isolated testing. When compared to the baseline short cowl configuration, the sound reduction effects of the serrated nozzle design as well as long cowl configuration were confirmed using source directivity analysis, both reducing the average SPL of the sound field by 3 dB. The wing presence lead to interesting behaviour, partly nullifying the benefit. The scarfed nozzle design only showed a minor interaction noise reduction effect when a wing was present, but did not change the mixing noise noticeably. Generally, tests using wing installation and flight stream simulation should be carried out preferably, provided that the testing budget permits this, as they facilitate a more holistic approach to sound field analysis and reflect the conditions during real flight better than the stationary isolated tests carried out in the course of aeroengine noise certification. All in all, the findings of this thesis correspond well with the elaborated theory. The source directivity analysis proved a valuable tool in assessing the ramifications of wing and flight stream presence. The plots revealed a much greater significance of both aspects then expected. Universally valid conclusions cannot be drawn from the data, however, considering the statistically low amount of test points investigated.

Based on the results obtained in the scope of this thesis, recommendations on future test setup were given. This especially concerns the layout of the linear microphone array, which was found to be of insufficient length and have too high spacing between microphones. As a next working step, the obtained data should be projected to the farfield and comparisons with the QinetiQ farfield data from the OPENAIR experiment should be made. Additionally, further research of the sound field of a scarfed nozzle with a wing installed could potentially yield interesting results.

Bibliography

[1] S. Bashforth. The effect of flight and the presence of an airframe on exhaust noise. AIAA Paper 81-2029, Rolls-Royce Ltd., Derby, England, 1981.

[2] P. Böhning. OPENAIR Test Definition Document. Test Requirement Document D2.4.7, RRD, 2012.

[3] Boeing Market Analysis. Current Market Outlook. Market forecast, Boeing Commercial Airplanes, 2013.

[4] W. J. G. Bräunling. *Flugzeugtriebwerke*. Springer Verlag, Berlin / Heidelberg, second edition, 2004.

[5] W. D. Bryce and R. C. K. Stevens. An investigation of the noise from a scale model of an engine exhaust system. AIAA Paper 75-459, National Gas Turbine Establishment, Farnborough, England, 1975.

[6] DLR. Institute of propulsion technology. "`http://www.dlr.de/at/en/desktopdefault.aspx/tabid-1521/2269_read-3715/`", 2015. [Online; accessed on 14th August 2015].

[7] easyJet Airline Company Ltd. *A319/A320 Flight Crew Operating Manual (FCOM)*. DSC - Aircraft Systems, DSC-27 - Flight Controls, DSC-27-30 - Flaps and Slats.

[8] M. R. Fink. Propulsive lift noise. In H. H. Hubbard, editor, *Aeroacoustics of Flight Vehicles: Theory and Practice*, volume 1: Noise Sources of *NASA RP-1258*, chapter 8, pages 449–482. NASA Langley Research Center, Hampton, Virginia, August 1991.

[9] M. J. Fisher, P. A. Lush, and M. Harper Bourne. Jet noise. Journal of Sound and Vibration (1973) 28(3), 563-585, Institute of Sound and Vibration Research, University of Southampton, England, 1973.

[10] S. Funke, R. P. Dougherty, and U. Michel. SODIX in Comparison with various Deconvolution Methods. 5th Berlin Beamforming Conference Paper BeBeC-2014-11, DLR German Aerospace Center, 2014.

[11] S. Funke, A. Skorpel, and U. Michel. An extended formulation of the SODIX method with application to aeroengine broadband noise. Proceedings 18th aiaa/ceas aeroacoustics conference paper, DLR German Aerospace Center, 2012.

[12] K. Giering. Lärmwirkungen. Sondervorhaben des bundesministeriums für umwelt, naturschutz und reaktorsicherheit, Umweltbundesamt, 2010.

[13] C. H. Hansen. Fundamentals of Acoustics. Script, University of Adelaide, 2006.

[14] G. S. Hreinsson. Aircraft Noise. Script, Virginia Polytechnic Institute and State University, 1993. Mainly about EPNdB.

[15] ICAO. Chicago Convention on International Civil Aviation. Signed by the ICAO member states on the Convention of International Civil Aviation, 1944.

[16] ICAO, Committee on Aviation Environmental Protection. Annex 16, Vol. I, Environmental Technical Manual. Chicago Convention Annex, 1971.

[17] ICAO, Committee on Aviation Environmental Protection. Annex 16, Vol. II, Aircraft Engine Emissions. Chicago Convention Annex, 1971.

[18] International Organisation for Standards (ISO). Preferred frequencies for acoustical measurements, 1997. ISO 266:1997.

[19] M. J. Lighthill. On sound generated aerodynamically: (i) general theory. Paper, Department of Mathematics, The University, Manchester, 1951.

[20] C. J. Mead and P. J. R. Strange. Under-Wing Installation effects on Jet Noise at sideline. AIAA Paper 98-2207, DERA Pyestock and Rolls-Royce plc, 1998.

[21] V. G. Mengle, L. Brusniak, R. Elkoby, and R. H. Thomas. Reducing Propulsion Airframe Aeroacoustic Interactions with Uniquely Tailored Chevrons: 3. Jet-Flap Interaction. AIAA Paper 2006-2435, The Boeing Company and NASA, 2006.

[22] U. Michel and S. Funke. Noise Source Analysis of an Aeroengine with a New Inverse Method SODIX. AIAA Paper 2008-2860, DLR German Aerospace Center, 2008.

[23] U. Michel and H. Siller. Aircraft Noise Course. Lecture script, DLR German Aerospace Center, 2010.

[24] G. Müller and M. Möser. *Taschenbuch der Technischen Akustik*. Springer Verlag, Berlin / Heidelberg, third edition, 2004.

[25] M. Möser. *Technische Akustik*. Springer Vieweg, Heidelberg, ninth edition, 2012.

[26] Nelson, P. M. (Ed.). *Transportation Noise Reference Book*. Butterworth & Co. Ltd., London, 1987.

[27] H. Oertel jr., M. Böhle, and T. Reviol. *Strömungsmechanik*. Springer Vieweg, Heidelberg, seventh edition, 2015.

[28] A. B. Packman, H. Kozlowski, and O. Gutierrez. Jet noise characteristics of unsuppressed duct burning turbofan exhaust system. AIAA Paper 76-149, Pratt and Whitney Aircraft / NASA Lewis Research Center, Washington, D.C., January 1976.

[29] G. J. J. Ruijgrok. *Elements of Aviation Acoustics*. Delft University Press, Delft, 2004.

[30] H. Schlichting and K. Gersten. *Grenzschichttheorie*. Springer Verlag, Berlin / Heidelberg, tenth edition, 2006.

[31] H. Sigloch. *Technische Fluidmechanik*. Springer Vieweg, Heidelberg, ninth edition, 2014.

[32] H. Siller, U. Tapken, and R. Bauers. OPENAIR Test Data Analysis. Report D2.4.11, DLR German Aerospace Center, 2013.

[33] M. J. T. Smith. *Aircraft Noise*. Press Syndicate of the University of Cambridge, Cambridge, 1989.

[34] H. K. Versteeg and W. Malalasekra. *An Introduction to Computational Fluid Dynamics*. Pearson Education Ltd., second edition, 2007.

[35] K. Viswanathan and M. J. Czech. Measurement and Modeling of Effect of Forward Flight on Jet Noise. Technical Report AIAA-2010-3921, 16th AIAA/CEAS Aeroacoustics Conference, Stockholm, Sweden, 2010.

[36] D. J. Way and B. A. Turner. Model Tests Demonstrating Under-Wing Installation Effects on Engine Exhaust Noise. AIAA Paper 80-1048, National Gas Turbine Establishment, Farnborough, England, 1980.

[37] C. Wrighton. OPENAIR Test Data. Test Conduct Report D2.4.10, QQ, 2013.

[38] O. Zaporozhets, V. Tokarev, and K. Attenborough. *Aircraft Noise*. Spon Press, Oxon, 2011.

Appendix

Table A.1: *Positions of the microphones used in the linear array.*

M	x [m]*	y [m]**	z[m]**	Θ [°]*	Θ* [°]*
1	-1,080	1,014	5,708	108,74	100,55
2	-1,020	1,014	5,708	107,76	99,98
3	-0,960	1,014	5,708	106,78	99,40
4	-0,900	1,014	5,708	105,78	98,82
5	-0,840	1,014	5,708	104,78	98,24
6	-0,780	1,014	5,708	103,76	97,66
7	-0,720	1,014	5,708	102,74	97,08
8	-0,660	1,014	5,708	101,71	96,49
9	-0,600	1,014	5,708	100,67	95,91
10	-0,540	1,014	5,708	99,63	95,32
11	-0,480	1,014	5,708	98,57	94,73
12	-0,420	1,014	5,708	97,51	94,14
13	-0,360	1,014	5,708	96,45	93,55
14	-0,300	1,014	5,708	95,38	92,96
15	-0,240	1,014	5,708	94,31	92,37
16	-0,180	1,014	5,708	93,24	91,78
17	-0,120	1,014	5,708	92,16	91,19
18	-0,060	1,014	5,708	91,08	90,59
19	0,000	1,014	5,708	90,00	90,00
20	0,060	1,014	5,708	88,92	89,41
21	0,120	1,014	5,708	87,84	88,81
22	0,180	1,014	5,708	86,76	88,22
23	0,240	1,014	5,708	85,69	87,63
24	0,300	1,014	5,708	84,62	87,04
25	0,360	1,014	5,708	83,55	86,45
26	0,420	1,014	5,708	82,49	85,86
27	0,480	1,014	5,708	81,43	85,27

Continued on next page

Table A.1 – continued from previous page

M	x [m]*	y [m]**	z[m]**	Θ [°]*	Θ* [°]*
28	0,540	1,014	5,708	80,37	84,68
29	0,600	1,014	5,708	79,33	84,09
30	0,660	1,014	5,708	78,29	83,51
31	0,720	1,014	5,708	77,26	82,92
32	0,780	1,014	5,708	76,24	82,34
33	0,840	1,014	5,708	75,22	81,76
34	0,900	1,014	5,708	74,22	81,18
35	0,960	1,014	5,708	73,22	80,60
36	1,020	1,014	5,708	72,24	80,02
37	1,080	1,014	5,708	71,26	79,45
38	1,140	1,014	5,708	70,30	78,88
39	1,200	1,014	5,708	69,35	78,31
40	1,260	1,014	5,708	68,41	77,74
41	1,320	1,014	5,708	67,48	77,17
42	1,380	1,014	5,708	66,57	76,61
43	1,440	1,014	5,708	65,66	76,05
44	1,500	1,014	5,708	64,77	75,49
45	1,560	1,014	5,708	63,90	74,94
46	1,620	1,014	5,708	63,03	74,39
47	1,680	1,014	5,708	62,18	73,84
48	1,740	1,014	5,708	61,34	73,29
49	1,800	1,014	5,708	60,52	72,75
50	1,860	1,014	5,708	59,71	72,21
51	1,920	1,014	5,708	58,91	71,68
52	1,980	1,014	5,708	58,12	71,14
53	2,040	1,014	5,708	57,35	70,61
54	2,100	1,014	5,708	56,59	70,09
55	2,160	1,014	5,708	55,85	69,57
56	2,220	1,014	5,708	55,11	69,05
57	2,280	1,014	5,708	54,39	68,53
58	2,340	1,014	5,708	53,69	68,02
59	2,400	1,014	5,708	52,99	67,51
60	2,460	1,014	5,708	52,31	67,01
61	2,520	1,014	5,708	51,64	66,51
62	2,580	1,014	5,708	50,98	66,01
63	2,640	1,014	5,708	50,34	65,52
64	2,700	1,014	5,708	49,70	65,03

Continued on next page

Table A.1 – continued from previous page

M	x [m]*	y [m]**	z[m]**	Θ [°]*	Θ* [°]*
65	2,760	1,014	5,708	49,08	64,54
66	2,820	1,014	5,708	48,47	64,06
67	2,880	1,014	5,708	47,87	63,58
68	2,940	1,014	5,708	47,28	63,11
69	3,000	1,014	5,708	46,70	62,64
70	3,060	1,014	5,708	46,14	62,17
71	3,120	1,014	5,708	45,58	61,71
72	3,180	1,014	5,708	45,04	61,25
73	3,240	1,014	5,708	44,50	60,80
74	3,300	1,014	5,708	43,98	60,35
75	3,360	1,014	5,708	43,46	59,90
76	3,420	1,014	5,708	42,95	59,46
77	3,480	1,014	5,708	42,46	59,02
78	3,540	1,014	5,708	41,97	58,59
79	3,600	1,014	5,708	41,49	58,16
80	3,660	1,014	5,708	41,02	57,73
81	3,720	1,014	5,708	40,56	57,31
82	3,780	1,014	5,708	40,11	56,89
83	3,840	1,014	5,708	39,66	56,48
84	3,900	1,014	5,708	39,23	56,07
85	3,960	1,014	5,708	38,80	55,66
86	4,020	1,014	5,708	38,38	55,26
87	4,080	1,014	5,708	37,97	54,86
88	4,140	1,014	5,708	37,56	54,47
89	4,200	1,014	5,708	37,17	54,08
90	4,260	1,014	5,708	36,78	53,69
91	4,320	1,014	5,708	36,39	53,31
92	4,380	1,014	5,708	36,01	52,93
93	4,440	1,014	5,708	35,65	52,55
94	4,500	1,014	5,708	35,28	52,18
95	4,560	1,014	5,708	34,92	51,81
96	4,620	1,014	5,708	34,57	51,45
97	4,680	1,014	5,708	34,23	51,09
98	4,740	1,014	5,708	33,89	50,73
99	4,800	1,014	5,708	33,56	50,38
100	4,860	1,014	5,708	33,23	50,03

* relative to core nozzle, ** relative to x-axis

Table A.2: *Third octave bands according to ISO 266 [18].*

No	Nominal	Lower	Center	Upper
1	10.00	8.91	10.00	11.22
2	12.50	11.22	12.59	14.13
3	16.00	14.13	15.85	17.78
4	20.00	17.78	19.95	22.39
5	25.00	22.39	25.12	28.18
6	31.50	28.18	31.62	35.48
7	40.00	35.48	39.81	44.67
8	50.00	44.67	50.12	56.23
9	63.00	56.23	63.10	70.79
10	80.00	70.79	79.43	89.13
11	100.00	89.13	100.00	112.20
12	125.00	112.20	125.89	141.25
13	160.00	141.25	158.49	177.83
14	200.00	177.83	199.53	223.87
15	250.00	223.87	251.19	281.84
16	315.00	281.84	316.23	354.81
17	400.00	354.81	398.11	446.68
18	500.00	446.68	501.19	562.34
19	630.00	562.34	630.96	707.95
20	800.00	707.95	794.33	891.25
21	1000.00	891.25	1000.00	1122.02
22	1250.00	1122.02	1258.93	1412.54
23	1600.00	1412.54	1584.89	1778.28
24	2000.00	1778.28	1995.26	2238.72
25	2500.00	2238.72	2511.89	2818.38
26	3150.00	2818.38	3162.28	3548.13
27	4000.00	3548.13	3981.07	4466.84
28	5000.00	4466.84	5011.87	5623.41
29	6300.00	5623.41	6309.57	7079.46
30	8000.00	7079.46	7943.28	8912.51
31	10000.00	8912.51	10000.00	11220.18
32	12500.00	11220.18	12589.25	14125.38
33	16000.00	14125.38	15848.93	17782.79
34	20000.00	17782.79	19952.62	22387.21

Source position grids

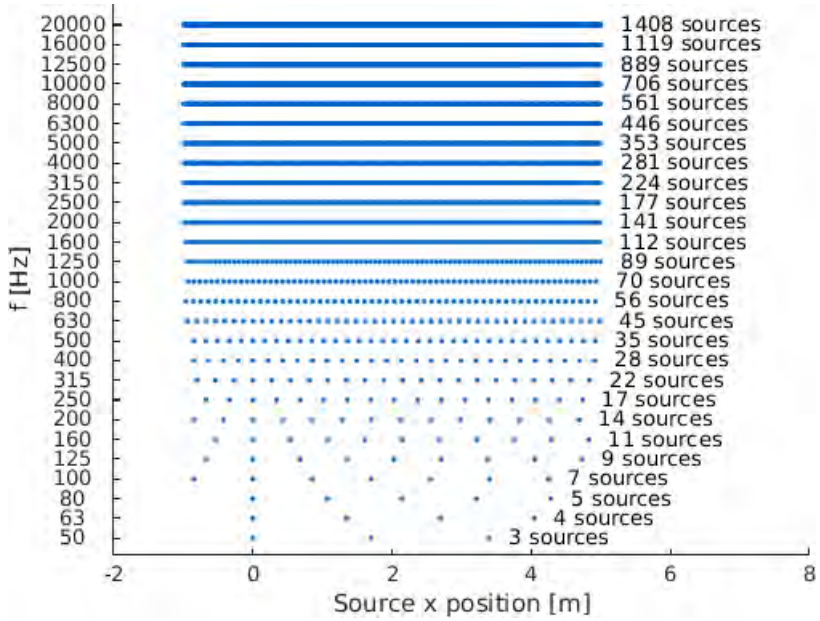

Figure A.1: *Reference source position grid.*

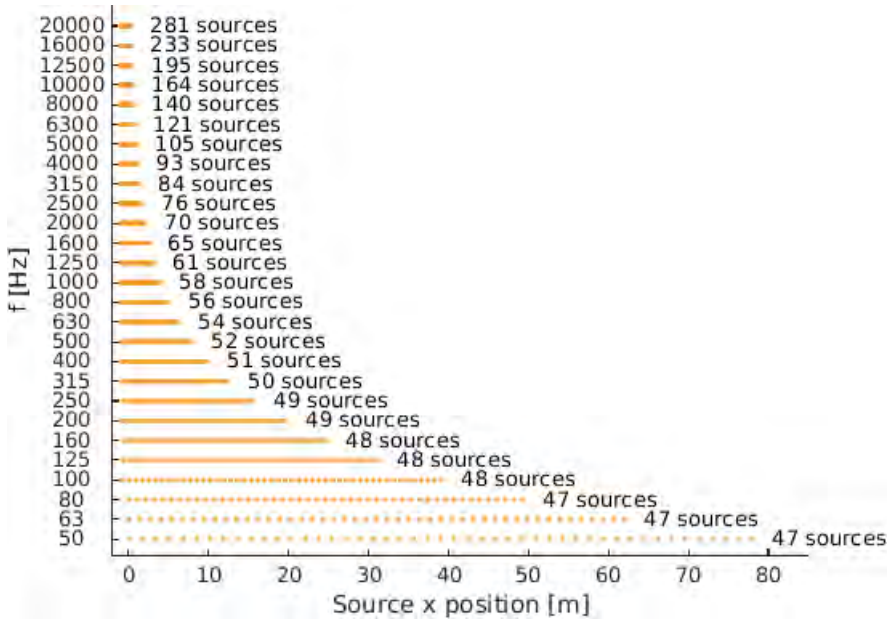

Figure A.2: *Linearly scaled source position grid, normalized to TOB* 800 Hz.

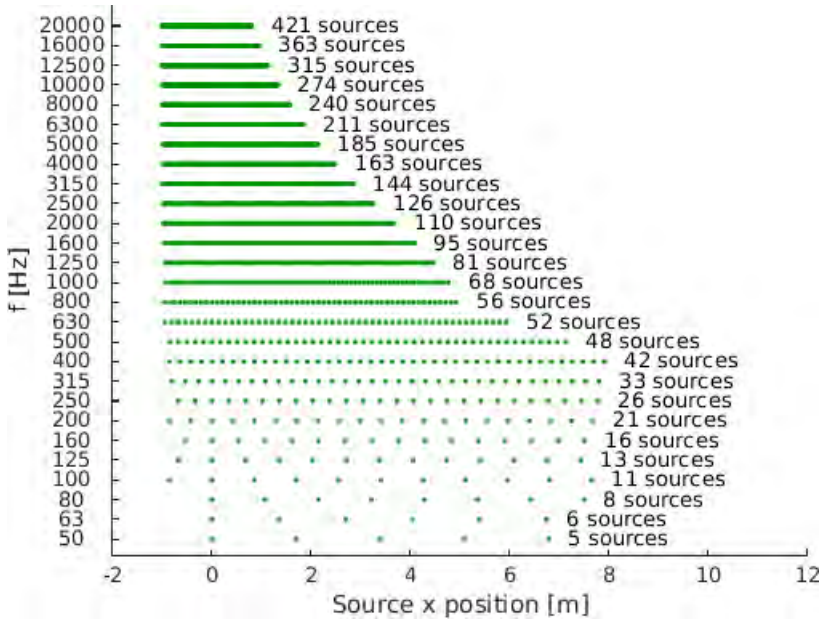

Figure A.3: *Linearly scaled source position grid with weighting factor, normalized to TOB* 800 Hz*.*

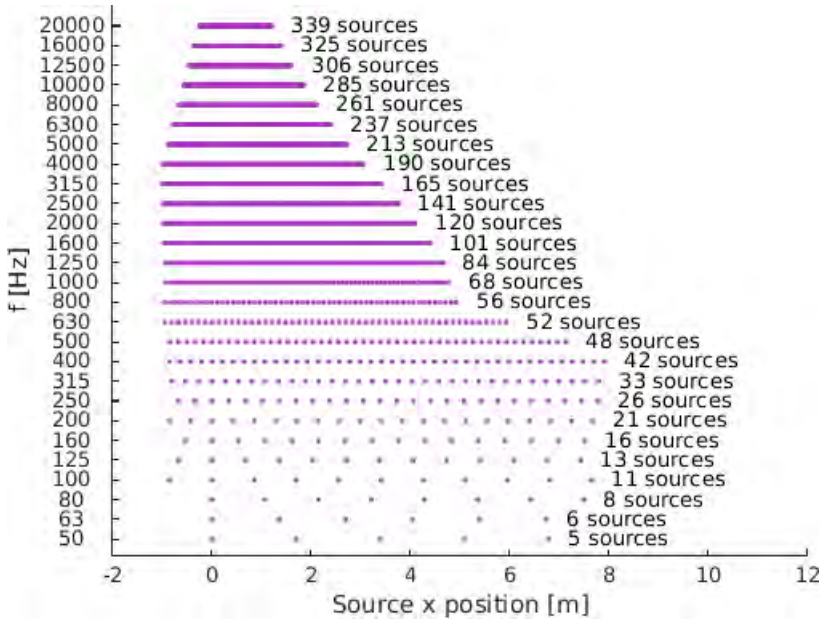

Figure A.4: *Linearly scaled source position grid with weighting factor with corrections for high frequencies, normalized to TOB* 800 Hz*.*

Table A.3: *Comprehensive compilation of all test points analysed in the scope of this thesis with their respective conditions.*

DLR TP	QQ TP	Cond.	Conf.	Nozzle	FS [m/s]	Wing	Noise	Iter.
247	CP 386	None	SC	Baseline	70	No	BG	100
248	CP 390	None	SC	Baseline	90	No	BG	100
317	CP 471	SL	SC	Baseline	0	No	BG	200
435	CP 606	SL	SC	Baseline	0	Yes	BG	200
279	CP 432	CB	SC	Baseline	0	No	BG	200
411	CP 592	CB	SC	Baseline	0	Yes	BG	200
287	CP 440	APP	SC	Baseline	0	No	BG	200
395	CP 566	APP	SC	Baseline	0	Yes	BG	200
325	CP 479	SL	SC	Baseline	90	No	BG	200
443	CP 614	SL	SC	Baseline	90	Yes	BG	200
257	CP 410	CB	SC	Baseline	90	No	BG	200
423	CP 594	CB	SC	Baseline	90	Yes	BG	200
297	CP 450	APP	SC	Baseline	70	No	BG	200
403	CP 574	APP	SC	Baseline	70	Yes	BG	200
306	CP 460	None	SC	Baseline	0	No	BB	200
383	CP 538	None	SC	Baseline	0	Yes	BB	200
350	CP 504	SL	SC	Baseline	90	No	BB-A	100
444	CP 615	SL	SC	Baseline	90	Yes	BB-A	100
527	CP 719	SL	SC	Scarfed	90	No	BG	100
599	CP 809	SL	SC	Scarfed	90	Yes	BG	100
735	CQ 164	SL	SC	Serrated	90	No	BG	200
817	CQ 264	SL	SC	Serrated	90	Yes	BG	200
900	CQ 375	SL	LC	Baseline	0	No	BG	100
914	CQ 389	SL	LC	Baseline	90	No	BG	100